

# Ultra-peripheral J/ $\psi$ photoproduction in PbPb collisions at $\sqrt{s_{NN}}=2.76$ TeV with CMS

By

R. Patrick Kenny III

Submitted to the Department of People who read Abstracts and the  
Graduate Faculty of the University of Kansas  
in partial fulfillment of the requirements for the degree of  
Doctor of Philosophy

Committee members

---

MEMBER 1, Chairperson

---

MEMBER 2

---

MEMBER 3

---

MEMBER 4

Date defended: 

---

October 02, 2012

The Dissertation Committee for R. Patrick Kenny III certifies  
that this is the approved version of the following dissertation :

Ultra-peripheral  $J/\psi$  photoproduction in PbPb collisions at  $\sqrt{s_{NN}}=2.76$  TeV with CMS

---

MEMBER 1, Chairperson

Date approved: October 03, 2012

# Abstract

The first is some L<sup>A</sup>T<sub>E</sub>X code, don't change it.

## **Acknowledgements**

I would like to thank all of the little people who made this thesis possible.

# Contents

<b>1</b>	<b>Introduction</b>	<b>1</b>
1.1	Overview . . . . .	1
1.2	Variables in heavy-ion measurements . . . . .	3
1.3	Temperature and energy density of the QGP . . . . .	5
1.4	Elliptic flow and viscosity in the QGP . . . . .	8
1.5	Recent results from HI control measurements . . . . .	9
<b>2</b>	<b>Photo-nuclear interactions</b>	<b>12</b>
2.1	Weizsäcker-Williams approximation . . . . .	13
2.2	The STARlight model . . . . .	17
2.3	The Adeluyi and Bertulani model . . . . .	21
2.4	Leading Twist Approach Derivation . . . . .	23
2.5	Photon-induced nuclear break-up . . . . .	25
2.6	Experimental Results . . . . .	29
2.6.1	UPC measurements at RHIC . . . . .	29
2.6.2	UPC $J/\psi$ at the LHC . . . . .	31
<b>3</b>	<b>The Compact Muon Spectrometer detector</b>	<b>36</b>
3.1	Tracker . . . . .	37
3.2	ECAL . . . . .	39
3.3	HCAL . . . . .	40

3.4	ZDC . . . . .	41
3.5	Muons . . . . .	42
3.6	Trigger . . . . .	47
<b>4</b>	<b>ZDC reconstruction</b>	<b>49</b>
4.1	Break up determination . . . . .	49
4.1.1	ZDC signal reconstruction . . . . .	49
4.1.2	Determination of the one neutron thresholds . . . . .	51
4.1.3	ZDC reconstruction method comparison . . . . .	54
<b>5</b>	<b>UPC Trigger development for CMS</b>	<b>58</b>
5.1	L1 trigger . . . . .	58
5.2	HLT trigger . . . . .	60
5.3	Studies of 2011 PbPb data . . . . .	61
5.3.1	High mass $\gamma\gamma \rightarrow e^+e^-$ in PbPb 2011 . . . . .	61
5.3.2	UPC hadronic overlap . . . . .	62
5.3.3	UPC $J/\psi$ with muons in HF . . . . .	63
5.4	Trigger development for the LHC pPb Run . . . . .	63
5.4.1	pPb $J/\psi$ . . . . .	64
<b>6</b>	<b>Analysis</b>	<b>65</b>
6.1	Physics generators and Monte Carlo simulations . . . . .	65
6.1.1	MC vs Data compairson . . . . .	66
6.1.2	STARlight and particle gun MC in CMS . . . . .	66
6.2	Event selection . . . . .	70
6.2.1	Data sets . . . . .	71
6.2.2	Event selection cuts . . . . .	72
6.3	Signal extraction . . . . .	75
6.4	Efficiency determination . . . . .	79

6.4.1	Muon efficiencies . . . . .	80
6.4.2	ZDC trigger efficiency . . . . .	84
<b>7</b>	<b>Systematic uncertainties</b>	<b>87</b>
7.1	Template fit normalization . . . . .	87
7.2	ZDC trigger efficiency . . . . .	89
7.3	ZDC reconstruction . . . . .	90
7.4	HF noise threshold . . . . .	91
7.5	MC acceptance . . . . .	92
7.6	Additional systematic checks . . . . .	93
7.6.1	Mass fit . . . . .	93
7.6.2	Tag and probe from counting compared to fitting . . . . .	93
7.6.3	The effect of noise on ZDC trigger efficiency estimates . . . . .	95
<b>8</b>	<b>Results and summary</b>	<b>97</b>
8.1	Coherent $J/\psi$ cross section . . . . .	97
8.2	diMuon-neutron correlations . . . . .	98
<b>A</b>	<b>My Appendix, Next to my Spleen</b>	<b>111</b>

# List of Figures

1.1	Comparison of $\frac{dE_T}{d\eta}$ as a function of collision energy, $\sqrt{s_{NN}}$ , normalized by the number participating nucleons, $N_p$ , to account for the difference in the ion species collided at the various different experiments. . . . .	6
1.2	Direct photon yield as a function of $p_T$ from PHENIX [1] (left) and ALICE [2] (right) . . . . .	7
1.3	Schematic of the initial nuclear overlap and elliptic flow. . . . .	8
1.4	$v_2/\varepsilon$ as a function of $1/S\frac{dN_{ch}}{dy}$ for different different values of $\eta/s$ for KLN initial state (left) and Glauber initial state (center) compared to STAR (overlaid) and CMS and PHOBOS data (right). . . . .	10
1.5	$v_2$ measured using the cumulant method in pPb collisions . . . . .	11
2.1	The electromagnetic field boosted and at rest. . . . .	13
2.2	ZDC neutron spectrum at RHIC with each a Gaussian fit to the 1, 2, 3, 5, and 5 neutron peak [3]. . . . .	30
2.3	The energy asymmetry in the ZDCs for photon-induced interaction, coulomb events, and nuclear interaction, hadronic events [3]. . . . .	31
2.4	Coherent $J/\psi$ photoproduction cross section in ultra-peripheral PbPb collisions at $\sqrt{s_{NN}} = 2.76$ TeV, measured by the ALICE experiment at forward and mid-rapidity []. . . . .	32
2.5	Nuclear suppression factor, $S$ , in the AB and LTA methods. . . . .	34
2.6	Nuclear suppression factor, $S$ , in STARlight method. . . . .	35



3.1	The Compact Muon Solenoid layout [4]. . . . .	37
3.2	Layout of the silicon tracker with the pixels closest to the interaction point, marked with a black dot, and the strips segments beyond the pixels. . . . .	38
3.3	Material budget in the tracker broken down by sub-detector(left) and category (right). . . . .	38
3.4	The energy resolution of ECAL as a function of energy [4]. . . . .	39
3.5	The $E_T$ resolution of HCAL as a function of $ \eta $ and $E_T$ [4]. . . . .	40
3.6	The CMS muon system showing the four DT stations in the barrel (MB1-MB4), the four CSC stations in the endcap (ME1-ME4), and the RPC stations. . . . .	43
3.7	Schematic of the DT chambers and an individual DT cell. . . . .	44
3.8	Schematic of a RPC cell. . . . .	44
3.9	Schematic of the CSC chambers and an individual CSC cell. . . . .	45
3.10	The momentum resolution of the muon system using only the tracker and the whole muon system in the barrel (left) and end cap (right). . . . .	46
3.11	The amount of material in CMS as a function of $\eta$ in number of interaction lengths. . . . .	47
4.1	Average ZDC pluse shape is plotted as the charge as a function of time slice for the first hadronic from $ZDC^-$ (left) and $ZDC^+$ (right). . . . .	50
4.2	The fraction of signal in time slice 5 over time slice 4 as a function of the signal in time slice 5 in $ZDC^-$ (left) and $ZDC^+$ (right). . . . .	51
4.3	Fit to the signal spectra for $ZDC^-$ (left) and $ZDC^+$ (right) . . . . .	52
4.4	ZDC noise spectra from $ZDC^-$ EM section (upper left), $ZDC^+$ EM section (upper right), $ZDC^-$ HAD section (lower left), and $ZDC^+$ HAD section (lower right) from out of time time slices. . . . .	53
4.5	Fit to charge spectrum from $ZDC^-$ (left) and $ZDC^+$ (right) using the comparison reconstruction method . . . . .	54
4.6	Comparison of the nominal (red) ZDC reconstruction method and the comparison (blue) method for $ZDC^-$ (left) and $ZDC^+$ (right). . . . .	55

4.7	Effects of requiring in-time signal in successively more ZDC hadronic channels, no timing, at least one (red), at least two (green), at least three (blue), and all four (yellow) HAD channels have a maximum signal in the fourth time slice. . . . .	56
4.8	Effect of ZDC signal timing requirements after noise subtraction. . . . .	57
5.1	Coherent excess in inclusive $J/\psi$ $p_T$ spectrum. . . . .	62
6.1	Comparison of the of the dimuon rapidity distributions between coherent $J/\psi$ MC sample and data. . . . .	66
6.2	Comparison of the of the dimuon $\phi$ distributions between coherent $J/\psi$ MC sample and data. . . . .	67
6.3	Comparison of the of the dimuon $p_T$ distributions between coherent $J/\psi$ MC sample and data. . . . .	68
6.4	Generator level rapidity (left) and $p_T$ (right) distributions for the coherent (black), incoherent (red), and photon-photon process (green). . . . .	69
6.5	The $J/\psi$ polarization of the particle gun (red), coherent (blue), and incoherent samples are plotted as the cosine of the helicity angle. . . . .	70
6.6	Comparison of HF noise distributions in zero bias data, physics triggered data, and MC. . . . .	74
6.7	Mass fit to $J/\psi$ using Gaussian for the signal and a first-order polynomial for the photon-photon continuum. . . . .	76
6.8	Fit to MC $p_T$ templates. . . . .	77
6.9	68%, 95%, and 99% confidence contours from the $p_T$ template fit. . . . .	78
6.10	Simultaneous fit to the mass and $p_T$ spectra. . . . .	78
6.11	68%, 95%, and 99% confidence contours from the simultaneous fit. . . . .	79
6.12	Muon daughter detectability from coherent $J/\psi$ . . . . .	80
6.13	Dimuon acceptance from coherent $J/\psi$ (top left), incoherent $J/\psi$ (top right), and photon-photon interactions (lower). . . . .	81

6.14	Fits to tag and probe pairs in the $J/\psi$ mass region for pairs with a probe $2 <  \eta  <$ $2.2$ and $1.55 < p_T < 1.8$ GeV. . . . .	82
6.15	Muon trigger efficiencies in $p_T$ and $\eta$ bins from the tag and probe method. . . . .	83
6.16	The trigger efficiency from tag and probe averaged over candidates in each $(p_T,  y )$ bin. . . . .	84
6.17	The acceptance times averaged trigger efficiency from tag and probe. . . . .	85
7.1	Coherent, incoherent, and photon-photon process $p_T$ template fit to data. . . . .	88
7.2	Various mass distribution fits and the corresponding $p_T$ template fit. . . . .	89
7.3	Mass fit to $J/\psi$ using Gaussian (Left) and Crystal Ball (Right) for the signal and a polynomial for the background . . . . .	93
7.4	Simultaneous fit to the mass and $p_T$ using mass templates for the mass fit. . . . .	94
7.5	Tag and probe trigger efficiencies from counting (left) compared to fitting (right). . .	95
8.1	Transverse momentum distribution of the $J/\psi$ when $J/\psi$ and neutron have the opposite rapidity direction and the transverse momentum distribution of the $J/\psi$ when $J/\psi$ and neutron have the same rapidity direction for low- $p_T$ (top left) and high- $p_T$ (top right) $J/\psi$ . Bottom: Ratios $R_{opp/same}$ for low- $p_T$ ( left) and high- $p_T$ ( right) $J/\psi$ . . . . .	100
8.2	Ratio between the transverse momentum distribution of the $J/\psi$ when $J/\psi$ and neutron have the opposite direction and the transverse momentum distribution of the $J/\psi$ when $J/\psi$ and neutron have the same direction. . . . .	101
8.3	Rapidity distribution of the $J/\psi$ when $J/\psi$ and neutron have the opposite rapidity direction and the rapidity distribution of the $J/\psi$ when $J/\psi$ and neutron have the same rapidity direction for low- $p_T$ (top left) and high- $p_T$ (top right) $J/\psi$ . Bottom: Ratios $R_{opp/same}$ for low- $p_T$ ( left) and high- $p_T$ ( right) $J/\psi$ . . . . .	102
8.4	Rapidity ratios $R_{opp/same}$ for low- $p_T$ ( left) and high- $p_T$ ( right) $J/\psi$ . . . . .	102

8.5	Rapidity distribution of $J/\psi$ in the case of the events having the neutron in negative and positive rapidity for the low- $p_T J/\psi$ (top), high- $p_T J/\psi$ (middle) and dimuons from $\gamma\gamma$ sample (bottom). . . . .	104
8.6	$R_{(\mu\mu)^-}^{\varepsilon_{ZDC}(n^-/n^+)}$ and $R_{(\mu\mu)^+}^{\varepsilon_{ZDC}(n^-/n^+)}$ integrated over one side in rapidity for low- and high- $p_T J/\psi$ and also for dimuons from $\gamma\gamma$ sample. . . . .	105

# List of Tables

2.1	$\sigma_{AA \rightarrow AAJ/\psi}(mb)$ the LTA, STARlight, AB methods. Four different gluon density models are used in the AB method. STARlight is a simulation software package that utilizes the STARlight model. . . . .	33
5.1	List of 2011 L1 seeds. . . . .	59
5.2	List of 2011 HLT trigger. . . . .	60
6.1	Integrated luminosities and number of events for the three samples used in this analysis. . . . .	72
6.2	Effects of event selection cuts. . . . .	73
6.3	ZDC trigger efficiencies for ZDC reconstruction method 1 and 2 . . . . .	86
7.1	Summary of systematic uncertainties . . . . .	87
7.2	ZDC trigger efficiencies using the nominal and comparison ZDC reconstructions for trigger sample that require a pixel track. . . . .	90
7.3	Thresholds from combined HF noise distributions and two-side noise distributions. . . . .	91
7.4	HF noise thresholds for keeping various fractions of the noise sample for RecHit and CaloTower. . . . .	92
7.5	Number of upc dimuon candidates with $p_T < 1$ GeV when changing HF calorimeter cuts for RecHit and CaloTower. . . . .	92
7.6	ZDC trigger efficiencies using the nominal and comparison ZDC reconstructions for trigger sample that do not require a pixel track. . . . .	96

8.1	Number of dimuon pairs for different directions of the neutron rapidity direction together with $R_{(\mu\mu)^-}^{n^-/n^+}$ and $R_{(\mu\mu)^+}^{n^-/n^+}$ . . . . .	103
8.2	Ratios $R_{(\mu\mu)^-}^{\varepsilon_{ZDC}(n^-/n^+)}$ and $R_{(\mu\mu)^+}^{\varepsilon_{ZDC}(n^-/n^+)}$ i.e. $R_{(\mu\mu)^-}^{n^-/n^+}$ and $R_{(\mu\mu)^+}^{n^-/n^+}$ corrected by the ZDC <sup>+</sup> and ZDC <sup>-</sup> efficiencies. . . . .	103

# Chapter 1

## Introduction

### 1.1 Overview

Microseconds after the Big Bang, the Universe existed in a state known as the Quark Gluon Plasma (QGP). In the QGP, quarks and gluons are not in hadronic bondage, forced to the confines of bound states such as protons and neutrons. The Large Hadron Collider (LHC) produces QGP in the lab in lead-lead (PbPb) collisions. The high energies and rates of the collisions at the LHC make it possible to do detailed studies of the QGP. The LHC is producing rare experimental probes such as suppressed jets and heavy quarkonia at unprecedented rates in heavy-ion collisions. As a result of recent LHC studies described in this thesis, physicists now have better constraints on the QGP properties like temperature, viscosity, and energy density.

The detailed studies of PbPb collisions coming out of the LHC experiments are in need of a understanding of the initial state of the ions before they collide. Without more knowledge of the initial state, physicists cannot determine which experimental effects are due to the QGP and which effects are inherent to the nuclei themselves. For example, suppression of heavy quarkonia is a signature of the QGP but also appears to occur in deuterium-gold (dAu) collisions where the QGP is not expected to arise [5]. Another important example is the measurement of viscosity, which depends on the relationship between the observed azimuthal anisotropy and the initial eccentricity of

the overlap of the two colliding nuclei (see Section 1.4). A clean probe of the initial state is needed by physicists to comprehensively understand the QGP. Ultra-peripheral heavy-ion collisions (UPC) at the LHC provide such a probe.

The current understanding of heavy-ion collisions evolved over the last 30 years. Relativistic heavy-ion collisions were first studied using the Alternating Gradient Synchrotron (AGS) at Brookhaven National Lab (BNL) in Upton, NY, followed by the Super Proton Synchrotron (SPS) at CERN near Geneva, Switzerland. From the numerous AGS and SPS experiments two main observables emerged, namely,  $J/\psi$  suppression and strangeness enhancement [?]. These results pioneered the search for the QGP.

At AGS the ion isotopes  $^{16}\text{O}$ ,  $^{28}\text{Si}$ , and  $^{197}\text{Au}$  beams were collided with fix targets. At SPS the same fix target configuration was used, but the ion isotopes were  $^{16}\text{O}$ ,  $^{32}\text{S}$ , and  $^{208}\text{Pb}$ . The center of mass energies per nucleon pair,  $\sqrt{s_{NN}}$ , for these experiments ranged from just below 5 GeV to 20 GeV. Although the strangeness enhancement and  $J/\psi$  suppression signals indicated that a deconfined state of quarks and gluons was likely created, at the energies of the AGS and SPS this state perished quickly. The threshold for creating the QGP requires an energy density of  $\sim 0.15 \text{ GeV}/fm^3$  and a temperature near 170 MeV [?]. Because of this, the QGP signals at the AGS and SPS energies could not have lasted long enough to study their properties.

Plans for a colliding beam machine dedicated to heavy-ions, designed to reach energies of 200 GeV per nucleon pair, was first proposed in 1983. It was believed that in these collisions signs of a hot gas of quarks and gluons would emerge. In 2000, RHIC began collisions and the four experiments, STAR, PHENIX, BRAHMS, and PHOBOS started taking data. The energies at RHIC were a factor of 10 higher than was previously achieved reaching the designed maximum energy. RHIC experiments confirmed the existence of a thermalized state of quarks and gluons. Contrary to expectations, the state found at RHIC was found to be a strongly coupled fluid with nearly no viscosity [?].

The LHC heavy-ion program began collisions in 2010, colliding PbPb at a center of mass energy of 2.76 TeV per nucleon pair. This corresponds to an increase in the colliding energy by



an order of magnitude with respect to RHIC. The LHC experiments, ALICE, ATLAS, and CMS have been studying the heavy-ion collisions since then. In 2013 LHCb joined the LHC heavy-ion program. Thanks to the LHC and RHIC physics programs, a new era of precision heavy-ion measurements is underway. The latest results from the LHC have come from the 2013 proton-lead (pPb) run. This period of data taking was originally designed to be a control measurement. However, CMS and ALICE have both shown an elliptical flow-like signal present in the pPb data [], which was unexpected. Understanding the origin of this nuclear effect is one of the most important priorities of the heavy-ion physics program at present. The latest data from the pPb measurements confirm the need to understand the nature of the initial state. UPC events fulfill this need by probing the nucleus through photon interactions. By measuring UPC  $J/\psi$  events, theoretical models of the initial state can be constrained. In this thesis, the CMS capability for measuring this process, the description of the analysis, and the comparison between the measured coherent  $J/\psi$  cross section to theoretical models are given.

In this chapter, the measurement of transverse energy, direct photons, and elliptic flow will be discussed. The transverse energy and direct photons measurements are related to the energy density and temperature of the QGP, which provide a confirmation of the production of QGP. The elliptic flow measurement is related to the viscosity of the QGP, which provides insight into the fluid like nature of the QGP state. Before discussing these results, several terms used to describe heavy-ion measurements and detectors will be discussed. This discussion will be divided into two parts, a generic description of the main detector elements, and an explanation of variables used in heavy-ion measurements.

## 1.2 Variables in heavy-ion measurements

The variables used by heavy-ion experiments at colliding beam facilities, such as the LHC and RHIC, are due to the cylindrical configuration of the detectors around the line of the beams. Two types of generic detectors are in use in heavy-ion experiments, trackers and calorimeters. A tracker

measures the trajectory of the particles as they pass through the detector. The particle trajectories measured by a tracker detector are called tracks. From these tracks, the particles' momenta can be deduced. In CMS tracks are mapped out from measuring charge deposits of in silicon cells. A tracker will typically be designed to interact minimally with the particles in order to preserve the trajectories of the particles. The second generic type of detector, a calorimeter, records the energy of the particles that hit it. A calorimeter is typically filled with dense material used to initiate a shower of particle collisions. The light from this shower of particles is collected and used to measure the energy of the initial particle or particles which hit the calorimeter. Unlike a tracker, a calorimeter typically is designed to stop the particles which hit it and collect as much of the energy of these particles as possible. The details the CMS detector will be discussed in more detail in Chapter 3.

Heavy-ion measurements will typically be comprised of combinations of the variables,  $p$ , for momentum,  $E$ , for energy,  $\phi$ , for the azimuthal angle,  $p_T$ , the transverse momentum,  $y$ , for rapidity, and  $\eta$ , for pseudorapidity. Energy are typically measured by a calorimeter and momentum by a tracker. The  $\phi$  angle is measured around the beam axis. The transverse momentum,  $p_T$ , is the component of the momentum that points perpendicular to the beam line. Rapidity is related to energy and momentum by  $y = \frac{1}{2} \ln \left( \frac{E+p_z}{E-p_z} \right)$ , where  $p_z$  is the momentum component that points in the direction of the beam axis. Here  $c$  is taken to be equal to 1. Pseudorapidity is defined by  $\eta = \frac{1}{2} \ln \left( \frac{|\mathbf{p}|+p_z}{|\mathbf{p}|-p_z} \right)$ , which can be shown to be equal to  $-\ln(\tan(\theta/2))$ . If  $m \ll p$ , where  $m$  is the mass of the particle, the relativistic equation for energy,  $E^2 = p^2 + m^2 \rightarrow E = p$ , and pseudorapidity is equal to the rapidity. Tracker measurements will typically provide a rapidity value with the mass assigned based on a particle identification criteria, where as calorimeter based measurements will typically be assigned a rapidity based the angle  $\theta$  with respect to the interaction point.

In addition, the variable called centrality is used in heavy-ion collisions to characterize the degree of activity. It is typically either measured using activity in either a calorimeter in the forward region at high  $\eta$  values or by the number of tracks. Centrality is reported as a percentage where 0% corresponds to the most energetic collisions and 100% corresponds to the least energetic. For

example, events assigned a centrality between 0-10% would be the top ten percent of events in terms of number of hits in a tracker detector or energy in a forward calorimeter depending on which variable is used for centrality. The number of nucleons that participate in a collision,  $N_{part}$ , the number of collisions between these participants,  $N_{col}$ , and the closest distance between the center of the two colliding nuclei, the impact parameter,  $b$ , are all related to the measured centrality percentage by use of a simulation. The convention of labeling the most active centralities 0% and the least active 100% is due to the correlation between the impact parameter. When the nuclei collide exactly head on the impact parameter is 0, which correlates with a 0% centrality value.

### 1.3 Temperature and energy density of the QGP

Lattice QCD predicts that the QGP forms above a critical temperature and energy densities, 170 MeV and  $1.5 \text{ GeV}/fm^{-3}$  []. The measurement of the  $\frac{dE_T}{d\eta}$  provides a means of estimating the energy density of the hot state created in heavy-ion collisions. The value of  $E_T$  for this measurement is defined as  $E_T = \sum_i E_i \sin\theta_i$ , where  $E_i$  is the energy measured by the  $i$ th calorimeter element and  $\theta$  is the angle between the center of the detector element and the interaction point. The temperature can be estimated from the transverse momentum spectrum of the direct photons, which are photons that are produced directly from the QGP. The measurements from CMS and ALICE at the LHC and STAR and PHENIX at RHIC confirm that the critical values for energy density and temperature are exceeded.

The values of  $\frac{dE_T}{d\eta}$  measured by CMS [6] and PHENIX [7] were done using the experiments' calorimeter systems. For the calculated  $\frac{dE_T}{d\eta}$  at  $\eta = 0$ , the interval  $|\eta| > 0.35$  was used by both experiments and corresponds to the full coverage of the PHENIX calorimeters. From the  $\frac{dE_T}{d\eta}$  at  $\eta = 0$  measurements, the energy density of the created medium at the LHC and RHIC were estimated from the Bjorken energy density formula,  $\epsilon_{Bj} = \frac{1}{A\tau} \frac{dE_T}{dy}$ , where  $A$  is the region of overlap between the two colliding nuclei and  $\tau$  is the formation time of the medium [8]. The formation time times the energy density,  $\tau\epsilon_{Bj}$ , from PHENIX was measured at RHIC to be  $5.4 \pm 0.6 \text{ GeV}$

$fm^{-2}c^{-1}$  for the centrality interval 0-5%. At the LHC CMS measured  $\tau\dot{\epsilon}_{Bj} = 14 \text{ GeV } fm^{-2}c^{-1}$  for the same centrality interval. Both values are well above the critical energy density of about  $1.5 \text{ GeV}/fm^3$  calculated from lattice QCD when assuming a medium formation time  $\tau = 1 \text{ fm}/c$ .

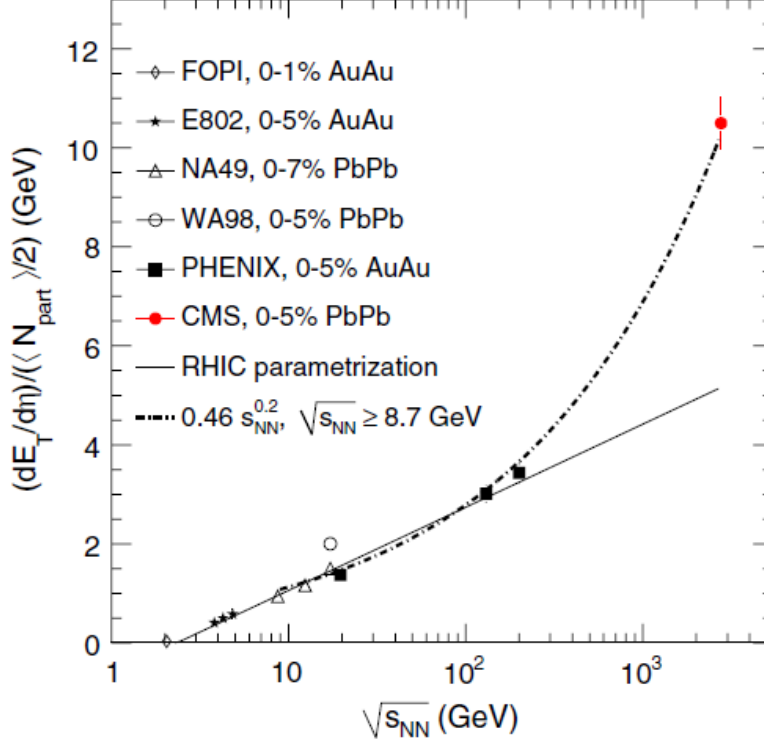


Figure 1.1: Comparison of  $\frac{dE_T}{d\eta}$  as a function of collision energy,  $\sqrt{s_{NN}}$ , normalized by the number participating nucleons,  $N_p$ , to account for the difference in the ion species collided at the various different experiments.

Direct photons defined as thermal photons created in the QGP, have been measured at RHIC by PHENIX [1] and at the LHC by ALICE [2] through the measurements of electron-positron pairs. Each experiment measured the inclusive  $p_T$  spectrum from electron-positron pairs, all pairs from the sample are taken without regard to the creation mechanism. The PHENIX measurement was taken from pp collisions and top 20% most energetic AuAu collisions, collisions with a centrality of 0-20%. The ALICE measurement analyzed the 0-40% centrality and 40%-80% centrality PbPb collisions, and pp collisions. In the PHENIX and ALICE measurements, the contribution to the inclusive spectrum was sorted into a direct component and a background component. The latter consists mainly of decays from hadrons such as  $\pi$  and  $\eta$  particles. In the PHENIX measurement

this was done by fitting to the mass distribution of the electron-positron pair for each  $p_T$ . For the ALICE measurement, the double ratio between the inclusive photons to pions over the ratio between photons from hadron decays and pions was measured to estimate the direct contribution. The inclusive photon  $p_T$  spectra were then rescaled by the direct photon fractions. The slope of an exponential fit to the low  $p_T$  portion of the direct photon spectrum is used to measure the temperature.

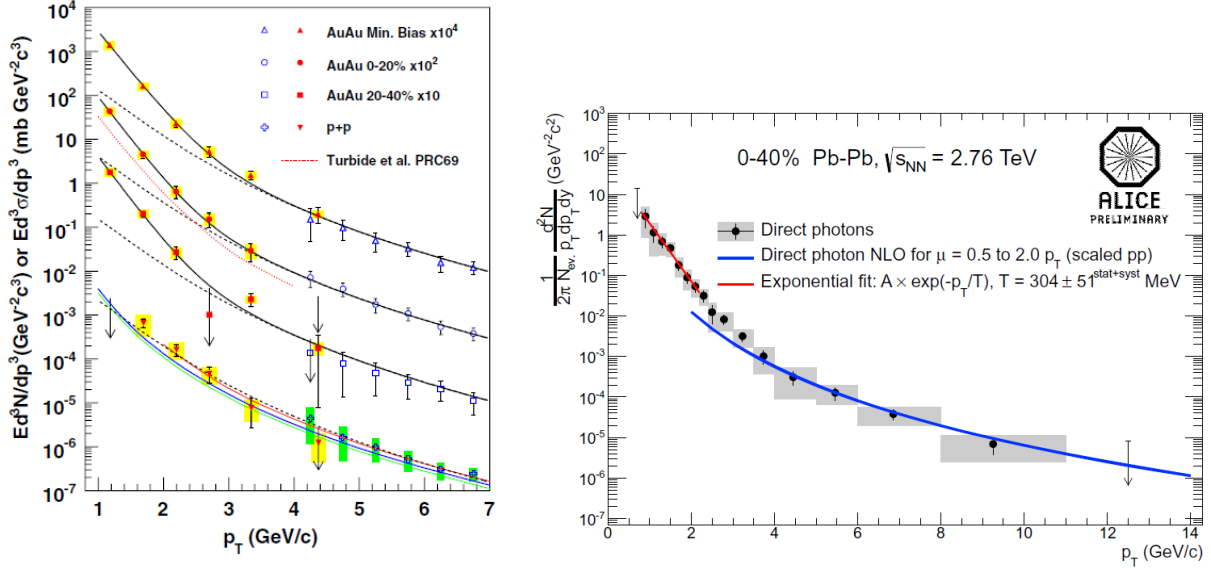


Figure 1.2: Direct photon yield as a function of  $p_T$  from PHENIX [1] (left) and ALICE [2] (right)

The temperature obtained from direct photon measurements offers a clear way of establishing whether the critical temperature for deconfinement was achieved. The direct photon  $p_T$  spectra in Fig. 1.2 shows a clear enhancement at low  $p_T$  compared to the rescaling to the pp spectra that fits the high  $p_T$  part, indicating a clear deviation from pp collisions. The low  $p_T$  photons are then consistent with thermal activity of the QGP. The thermal spectrum of the QGP is therefore imprinted on this part of the spectrum. The temperature from PHENIX was measured to be  $221 \pm 21$  MeV and  $304 \pm 51$  MeV from ALICE, both well above the critical temperature estimated from lattice QCD of  $\sim 170$  MeV. The combination of the energy density and temperature measurements create a consistent picture, that both RHIC and the LHC have created a deconfined state.

## 1.4 Elliptic flow and viscosity in the QGP

Prior to RHIC, the QGP was thought to be a hot gas of quarks and gluons. At RHIC, elliptic flow,  $v_2$ , was measured showing that the medium appears to obey hydrodynamic equations and flows like a fluid. This same signal was also measured by CMS [9] at the LHC.

Elliptic flow is the second order Fourier expansion coefficient of the azimuthal distribution of measured tracks. This expansion has the form

$$1 + \sum_{n=1}^{\infty} 2v_n \cos[n(\phi - \Psi)], \quad (1.1)$$

where  $v_n$  is the  $n$ th coefficient of the Fourier expansion,  $\phi$  is the azimuthal angle, and  $\Psi$  is the event-plane angle. The event-plane angle accounts for the random orientation of the nuclei event-by-event and is correlated with the reaction-plane,  $\Psi_R$  (see Fig. 1.3). The reaction-plane is defined by the line which runs through the center of the two nuclei when they reach the distance of closest approach.

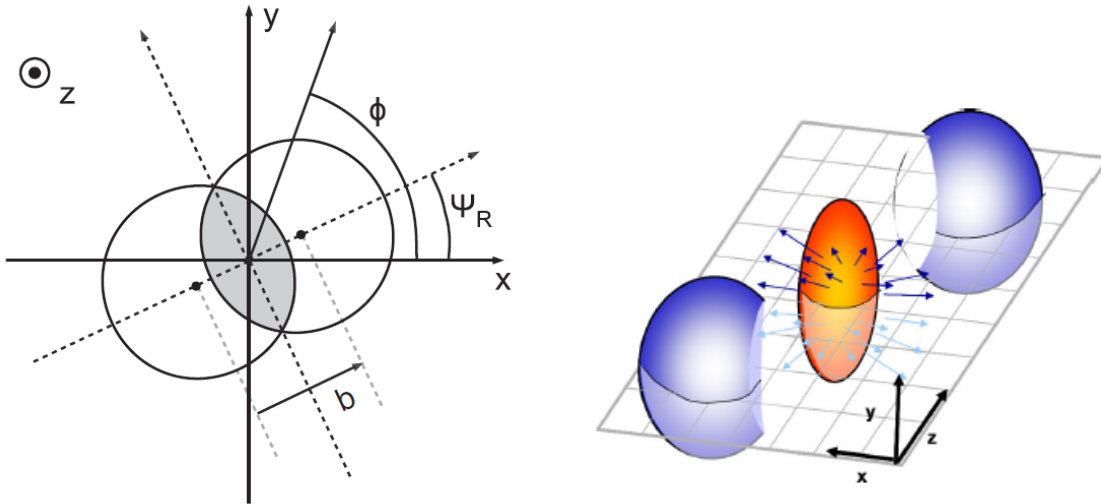


Figure 1.3: Schematic of the initial nuclear overlap and elliptic flow.

The  $v_2$  signal is believed to arise from pressure gradients. These pressure gradients originate from the initial elliptical shape of the overlap region between the colliding nuclei. The pressure

gradient is higher along the shorter axis compared to the longer axis of the ellipsoid in Fig 1.3. This difference in pressure gradient will create a flow of the QGP medium in the direction of the shorter axis. The flow is responsible for the measured anisotropic distribution of tracks.

The extent to which the initial shape of the overlap translates to flow in the medium is controlled by viscosity. A viscous fluid will tend to smooth out anisotropies and results in a smaller flow signal for the same overlap configuration of the initial nuclei. The ratio between the measured  $v_2$  signal and the initial eccentricity,  $\varepsilon$ , based on the given centrality is sensitive to the viscosity of the medium.

In Fig. 1.4,  $v_2/\varepsilon$  is plotted as a function of the number of charged particle,  $N_{ch}$ , per unit of pseudorapidity,  $\eta$ , per area of overlap between the colliding nuclei,  $S$  [10]. The model calculation was performed for four values of the ratio of the shear viscosity over entropy density,  $\eta/s$ , which are 0.0, 0.08, 0.16, and 0.24. The  $\eta/s$  value which gives the best agreement with data in Fig 1.4 depends strongly on the initial state model calculation. The observed strong dependence is one of the primary reason why more studies on the nature of the initial state are needed.

## 1.5 Recent results from HI control measurements

The proton-nucleus runs at the LHC and RHIC were pursued as control measurements. It was believed that these configurations could measure initial state backgrounds to heavy-ion measurements. However, a flow-like signal has been very recently measured in pPb collisions by LHC experiments. A  $v_2$  signal, like that indicating flow of the QGP in PbPb collisions, has been measured by CMS [1].

The  $v_2$  measurement shown in Fig 1.5 uses a cumulant method. This method differs from the event plan method discussed above, in that it uses the correlations between tracks rather than the  $\phi$  angle of the tracks with respect to the events plan angle. This method can be done using the correlations between any number of tracks. The number of tracks that are used for a given method is indicated by the number in brackets. In addition a method called the Lee-Yang Zeros

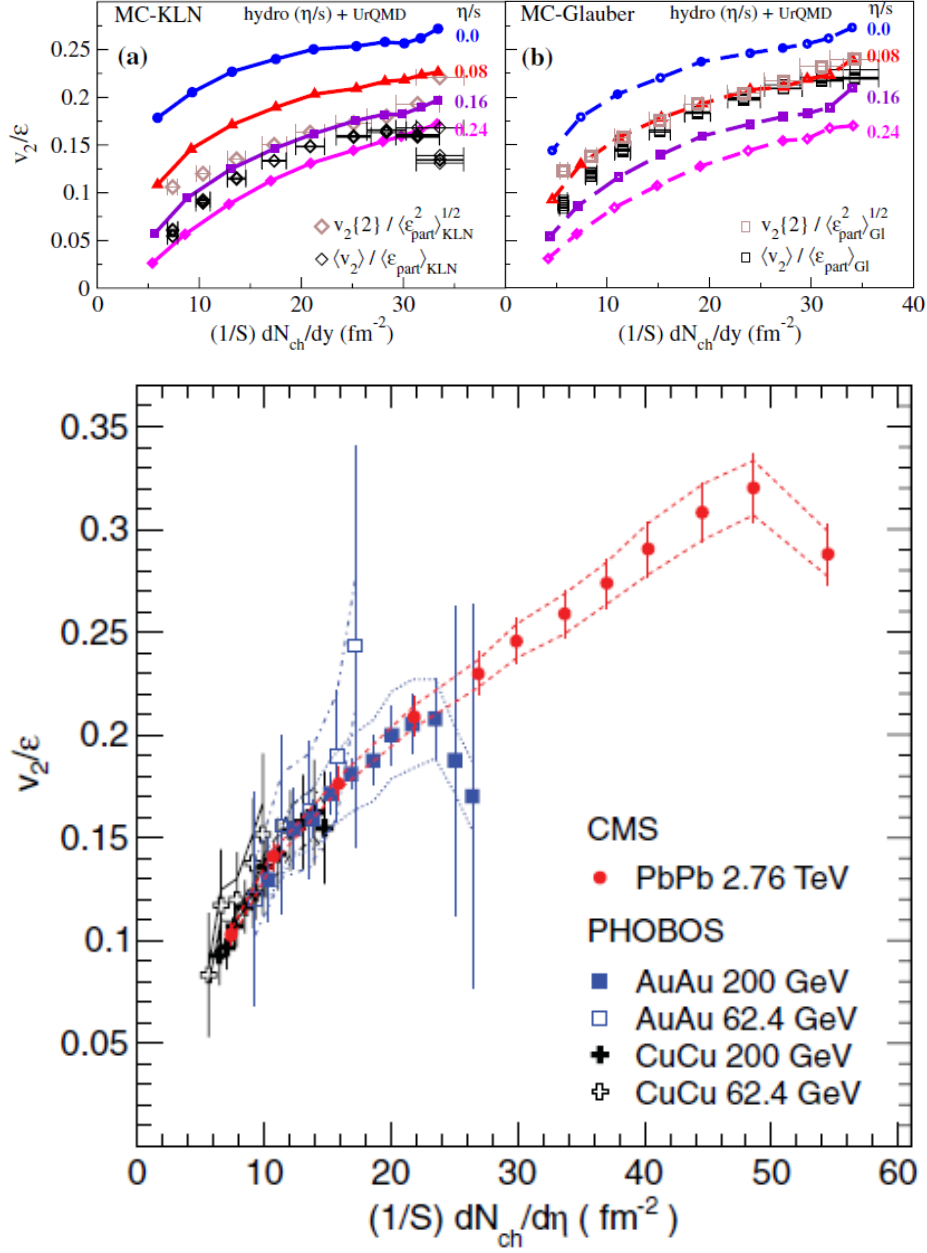


Figure 1.4:  $v_2/\epsilon$  as a function of  $1/S \frac{dN_{ch}}{dy}$  for different different values of  $\eta/s$  for KLN initial state (left) and Glauber initial state (center) compared to STAR (overlaid) and CMS and PHOBOS data (right).

(LYZ) method was used, which uses the correlations between all the tracks. The measurement is done over a range of total number of track,  $N_{trk}^{offline}$ . The range shown in Fig. 1.5 corresponds to the number of tracks present in PbPb collisions for centrality values between 50-60%. The  $v_2$  measurements using more than 2 track correlations are all consistent with each other. This is



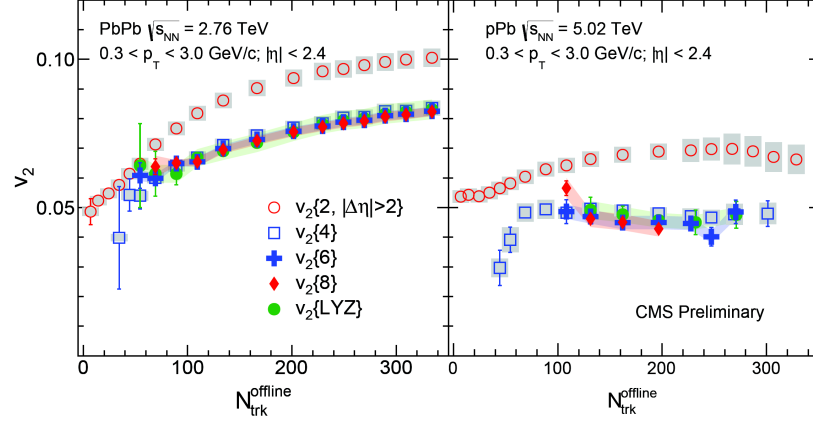


Figure 1.5:  $v_2$  measured using the cumulant method in pPb collisions

an indication that  $v_2$  in pPb collisions at the LHC is the result of collective motion. The pPb  $v_2$  measurement underscores the need for a clean probes of the initial

In this thesis the analysis of ultra-peripheral  $J/\psi$  photoproduction is discussed. In UPC events, the interaction between the nuclei occurs through exchange of photons. This results in a clean probe of the initial state of the nucleus. In the following chapter, the theory of  $J/\psi$  photoproduction in UPC events is presented.

# Chapter 2

## Photo-nuclear interactions

In ultra-peripheral heavy-ion collision, the colliding nuclei interact only electromagnetically. In such events, no QGP state emerges, and the effects arising from the QGP no longer obscure the initial state effects. Other initial state probes such as peripheral nuclear collisions and proton-nucleus collisions have the potential to create the QGP obscuring which effects come from the initial state. In UPC events the nuclei do not collide, therefore final state effects coming from the QGP are not expected. Thus, UPC events provide clarity by enhancing physicists' understanding of the initial state.

In particular, these interactions between the field of photons surrounding the colliding nuclei and the gluons within the nuclei can produce a  $J/\psi$ , probing the gluon density. The  $J/\psi$  can be produced either coherently or incoherently. In the case of coherent interactions, the photon couples to the nucleus as a whole. In the incoherent case, the photon couples to the nucleons within the nucleus. The UPC  $J/\psi$  photoproduction cross section is therefore a probe of the initial state of the nucleus.

This cross section can be calculated using three steps. First, the Weizsäcker-Williams approximation provides a way to calculate the density of probing photons that surrounds the nucleus. Second, the electron-proton scattering data gives a value for the proton photoproduction cross section at lower energies [11]. Last, a specific model is used to combined the previous two steps in

order to calculate the nuclear photoproduction cross section. In this thesis the perturbative Adelyi and Bertulani (AB), STARlight, and the Leading Twist (LTA) models are discussed. Each of these methods handle the gluon density of the nucleus differently producing a measurable difference in the value of the  $J/\psi$  photoproduction cross section. Measurements at the LHC have provided important constraints to models of the nuclear gluon density. The analysis presented in Chapter 6 adds to the existing data in a new kinematic region. In this Chapter the theoretical framework for photon-nuclear interactions, together with an experimental review of recent results on ultra-peripheral heavy-ion collisions are described.

## 2.1 Weizsäcker-Williams approximation

The density of photons surrounding the colliding nuclei can be calculated using the Weizsäcker-Williams approximation. This approximation relates the electric field of a stationary point charge to the photon field that arises at ultra relativistic velocities. The approximation is semi-classical and combines both classical and quantum elements. In the Weizsäcker-Williams approximation, a Fourier transform of Maxwell's equations is combined with the quantum mechanical equation for the energy of the photon. The frequency modes of the electrostatic field are treated as photons. The

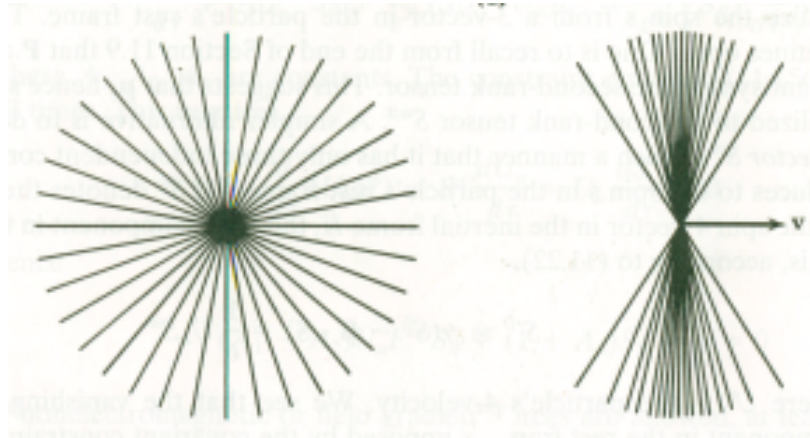


Figure 2.1: The electromagnetic field boosted and at rest.

Weizsäcker-Williams approximation makes the calculation of electromagnetic interactions with the

nucleus tractable.

The Weizsäcker-Williams approximation begins with the equation for the electric field of the projectile nucleus at rest. To calculate the photon flux on the target nucleus, the electromagnetic field only needs to be considered at the position of the target nucleus. From the projectile's point of view, the target is moving and contributes  $-vt$  to Eq. 2.1, the equation for the electric field of the projectile nucleus at rest.

$$x' = -vt', \quad y' = b, \quad z' = 0, \quad \vec{E}' = \left( \frac{eZ}{4\pi\epsilon_0 \left( (-vt')^2 + b^2 \right)^{3/2}} \right) \left( -vt' \hat{\mathbf{x}}' + b \hat{\mathbf{y}}' \right), \quad (2.1)$$

where  $b$  is the impact parameter defined as the distance of separation at closest approach,  $v$  is the velocity of the projectile nucleus,  $Z$  is the number of protons in the nucleus, and  $e$  is the charge of the electron. Two simplifications occur due to the choice of coordinates in Eq. 2.1. The magnetic field is equal to zero, as the projectile is at rest, and the  $z$  coordinate can be ignored, reducing the equation to two dimensions.

The Lorentz transformation converts the field equations in the projectile's frame to equations in the target's frame. Eq. 2.2 gives the result of the transformation from the projectile's primed frame to the target's rest frame for the field components [12]:

$$\begin{aligned} E'_x &= E_x, & \gamma(E'_y/c + \beta B'_z) &= E_y/c, & \gamma(E'_z/c + \beta B'_y) &= E_z/c, \\ B'_x &= B_x, & \gamma(B'_y - \beta E'_z/c) &= B_y, \text{ and } & \gamma(B'_z + \beta E'_y/c) &= B_z. \end{aligned} \quad (2.2)$$

The transformation equations for the fields, Eq. 2.2, and the transformation of the coordinates reduce to Eq. 2.3 [12]:

$$\begin{aligned} E'_x &= E_x, & \gamma E'_y &= E_y, & \gamma \beta E'_y/c &= B_z, \\ ct' &= \gamma ct, \text{ and } & x' &= -\gamma \beta ct. \end{aligned} \quad (2.3)$$

The Lorentz transformation reduces the six components of the electromagnetic field in the target's frame to the three equations in Eq. 2.2 by relating them to the fields in the projectile's frame.

By combining Eq. 2.1 and Eq. 2.2, equations for the electric and magnetic fields in the target's rest frame are obtained

$$\begin{aligned}\vec{\mathbf{E}} &= \left( \frac{\gamma e Z}{4\pi\epsilon_0 \left( (\gamma vt)^2 + b^2 \right)^{3/2}} \right) (vt\hat{\mathbf{x}} + b\hat{\mathbf{y}}), \text{ and} \\ \vec{\mathbf{B}} &= \frac{\gamma\beta e Z b}{4\pi c\epsilon_0 \left( (\gamma vt)^2 + b^2 \right)^{3/2}} \hat{\mathbf{z}} = \frac{\gamma\mu_0 v e Z b}{4\pi \left( (\gamma vt)^2 + b^2 \right)^{3/2}} \hat{\mathbf{z}}.\end{aligned}\quad (2.4)$$

If the impact parameter  $b$  goes to zero, the target sits in the line of the projectile particle's motion, and the denominator carries a factor of  $\gamma$  squared. When  $vt$  goes to zero, the projectile particle position lays on the  $y$ -axis, and the numerator carries a factor of  $\gamma$ . This results in fields that are a factor of  $\gamma^3$  higher in the  $y$  direction than in the  $x$  direction (see Fig. 2.1). The boost compresses the electric field of the charge in the direction of the boost and produces a magnetic field resulting in a form similar to radiation. The point charge at ultra relativistic velocities produces a strong electric field in the plane transverse to its motion resembling a plane wave.

Separating the electromagnetic field into even and odd functions of time simplifies the decomposition of the field equations into Fourier frequency modes. The even functions decompose into cosine functions, odd functions into sine functions. The  $y$ -component of the electric field and the  $z$ -component of the magnetic field are even functions in time, and the  $x$ -component of the electric field is an odd function in time. Eq. 2.5 gives the Fourier transformation integrals.

$$\begin{aligned}E_x(\omega) &= \sqrt{\frac{2}{\pi}} \frac{eZ}{4\pi\epsilon_0 b^2} \int_0^\infty \frac{(\gamma vt/b) \sin(\omega t)}{\left( (\gamma vt/b)^2 + 1 \right)^{3/2}} dt, \\ E_y(\omega) &= \sqrt{\frac{2}{\pi}} \frac{\gamma e Z}{4\pi\epsilon_0 b^2} \int_0^\infty \frac{\cos(\omega t)}{\left( (\gamma vt/b)^2 + 1 \right)^{3/2}} dt, \text{ and} \\ B_z(\omega) &= \frac{\beta E_y(\omega)}{c}.\end{aligned}\quad (2.5)$$

The solutions to the integrals of Eq. 2.5 are the following [13]:

$$u = \frac{\gamma vt}{b}, \quad du \left( \frac{b}{\gamma v} \right) = dt, \quad \omega' = \frac{\omega b}{\gamma v},$$

$$\int_0^\infty \frac{u \sin(\omega' u)}{(u^2 + 1)^{3/2}} du = \omega' K_0(\omega'), \text{ and } \int_0^\infty \frac{\cos(\omega' u)}{(u^2 + 1)^{3/2}} du = \omega' K_1(\omega'). \quad (2.6)$$

In Eq. 2.6,  $\omega$  can be related to the energy of a photon by  $E = \hbar\omega$ . The components of the electric field in terms of  $\omega$  are:

$$E_x(\omega) = \sqrt{\frac{2}{\pi}} \frac{eZ}{4\pi\epsilon_0 b^2} \frac{b}{\gamma v} \frac{\omega b}{\gamma v} K_0 \left( \frac{\omega b}{\gamma v} \right), \text{ and } E_y(\omega) = \sqrt{\frac{2}{\pi}} \frac{\gamma eZ}{4\pi\epsilon_0 b^2} \frac{b}{\gamma v} \frac{\omega b}{\gamma v} K_1 \left( \frac{\omega b}{\gamma v} \right). \quad (2.7)$$

The y-component of the electric field does not have a factor of  $t$  in the numerator in Eq. 2.5, therefore the factor of  $\gamma$  remains outside of the integral for the Bessel functions in Eq. 2.7. In Eq. 2.7,  $E_y$  carries an additional factor of  $\gamma$  in the numerator relative to the  $E_x$ , therefore in the case when  $\gamma \gg 1$ ,  $E_x$  can be neglected.

When  $v$  approaches  $c$ ,  $\beta \approx 1$ , the y-component of the electric field and the z-component of the magnetic field are related by a factor of  $c$ ,  $E_y/c = B_z$ .  $E_y$  is approximately equally to  $\gamma E_x$  because  $K_0(x)$  is smaller than  $K_1(x)$  for all  $x$ . The conditions imposed by the ultra-relativistic limit result in the following relationship

$$\gamma \gg 1 \Rightarrow \gamma E_x \gg E_x \Rightarrow E_y \gg E_x. \quad (2.8)$$

The six field components are reduced to one electric component and one perpendicular magnetic field component, which have a configuration identical to a plane wave.

As with plane waves, the energy per area per time transferred by the electromagnetic field is given by the Poynting vector. The Poynting vector takes the simple form of a plane pulse propagating in the  $x$  direction as given by

$$\vec{S} \equiv \vec{E} \times \vec{B}/\mu_0 = (E_y^2/c\mu_0) \hat{x} = c\epsilon_0 E_y^2 \hat{x}. \quad (2.9)$$

The Poynting vector relates to the fluence (energy per unit area) by the expression [14]

$$I(b) = \hat{\mathbf{x}} \cdot \int_0^\infty \vec{\mathbf{S}} d\omega = \int_0^\infty (c\epsilon_0 E_y^2) d\omega = \int_0^\infty \left( \frac{dI}{d\omega} \right) d\omega, \quad (2.10)$$

and the spectral fluence (energy per area per frequency) is given by

$$\frac{dI}{d\omega} = c\epsilon_0 E_y^2 = \frac{e^2 Z^2 c}{4\pi^3 b^2 v^2 \epsilon_0} \left( \frac{\omega b}{\gamma v} \right)^2 K_1^2 \left( \frac{\omega b}{\gamma v} \right) = \alpha \hbar \left( \frac{Z}{b\beta\pi} \right)^2 \left( \frac{\omega b}{\gamma v} \right)^2 K_1^2 \left( \frac{\omega b}{\gamma v} \right). \quad (2.11)$$

The spectral fluence given by Eq. 2.11 relates the frequency to energy. The quantum mechanical equation,  $E = \hbar\omega$ , gives the energy of a photon, which is related to the spectral fluence. The relationship between the photon number density and the spectral fluence is [12]

$$\frac{dI}{d\omega} d\omega = \hbar\omega N(\omega) d(\hbar\omega) \Rightarrow \frac{1}{\hbar^2 \omega} \frac{dI}{d\omega} = N(\omega). \quad (2.12)$$

Substituting Eq. 2.11 into Eq. 2.12 yields the semiclassical photon flux:

$$N(\omega, b) = \frac{\alpha}{\hbar\omega} \left( \frac{Z}{b\beta\pi} \right)^2 \left( \frac{\omega b}{\gamma v} \right)^2 K_1^2 \left( \frac{\omega b}{\gamma v} \right). \quad (2.13)$$

This replaces the classical electric field of a point charge with a semiclassical field of photons. The photon flux in Eq. 2.13 provides the electromagnetic input to the  $J/\psi$  photoproduction cross section calculation.

## 2.2 The STARlight model

The STARlight model for calculating the  $J/\psi$  photoproduction cross section has three main components. The STARlight approach is constructed from the Weizsäcker-Williams photon flux, uses the vector meson dominance fit to the proton-electron data, and uses the Glauber model for calculating the nuclear cross sections from the proton-electron cross sections. The Weizsäcker-Williams photon flux provides the probe. The proton-electron scattering data combine with the Glauber model

create a picture of the initial state of the nucleus. Each of the different approaches discussed in this thesis to calculating the UPC  $J/\psi$  photoproduction cross section use these same elements. However, the different models each use the last two elements differently to produce different pictures of the nucleus and different cross sections values.

The photon flux in the photoproduction cross section calculation must be finite in order for the cross section to be meaningful. The Weizsäcker-Williams approximation, Eq. 2.13, diverges at  $b = 0$ . The probability of the nuclei interacting would exceed one if the photon flux were infinite. Special treatment of impact parameter,  $b$ , where the colliding nuclei overlap eliminates the divergency.

A convolution of the photon flux with the nucleon number density functions removes the divergency at  $b = 0$ . The nucleon density of a single nucleus is given by

$$\rho_A(s) = \frac{\rho_0}{1 + \exp[(s - R_{WS})/d]}, \quad (2.14)$$

where  $s$  is the distance from the center of the nucleus,  $R_{WS}$  is the radius of the nucleus, and  $d$  is the skin depth, which determines how quickly the nucleon density falls off beyond the nuclear radius. In Eq. 2.15 the depth of the nucleus is integrated out leaving just the transverse dimension in  $T_A$ . The average number of nucleons in the overlap region is given by a convolution of  $T_A$  from each of the two nuclei to produce The average number of nucleons in the overlap region is given by a convolution of  $T_A$  from each of the two nuclei to produce nuclear overlap integral,  $T_{AA}$ ,

$$\begin{aligned} T_A(\vec{r}) &= \int dz \rho_A(\sqrt{|\vec{r}|^2 + z^2}), \text{ and} \\ T_{AA}(|\vec{b}|) &= \int d^2\vec{r} T_A(\vec{r}) T_A(\vec{r} - \vec{b}). \end{aligned} \quad (2.15)$$

For a given impact parameter  $b$ , the product of  $T_{AA}(|\vec{b}|)$  and  $\sigma_{NN}$  gives the average number of nucleon-nucleon collisions. It is  $T_{AA}$  that modulates the photon flux. As input to the Poisson distribution,  $T_{AA}$  reduces Eq. 2.13 at values of  $b$  where the nuclei overlap significantly and eliminates the divergency in the photon flux. The convolution of the photon flux with the  $b$ -dependent probability



that no nucleon-nucleon collisions occur removes the divergency in Eq. 2.13.

The Poisson distribution gives the probability that no collisions occur at a given  $b$  using the mean number of nucleons in the overlap region given by  $T_{AA}$ :

$$P_0(b) = \exp[-T_{AA}(b)\sigma_{NN}], \quad (2.16)$$

where  $\sigma_{NN}$  is the cross section for a nucleon-nucleon interaction, which gives the probability that a collision will occur given the average number of nucleons in the overlap region. The photon flux is averaged over impact parameter by integration of the  $b$ -dependent photon flux multiplied by the  $b$ -dependent probability of having no nucleon-nucleon interactions:

$$\frac{dN_\gamma(k)}{dk} = \int_0^\infty 2\pi b db P_0(b) \int_0^R \frac{r dr}{\pi R_A^2} \int_0^{2\pi} d\phi \frac{d^3 N_\gamma(k, b + r \cos(\phi))}{dk d^2 r}. \quad (2.17)$$

Although Eq. 2.17 goes down to  $b = 0$  where the photon flux is infinite, the fact that the probability of having a nucleon-nucleon collisions is high eliminates the divergency.

A power-law fit to the proton photoproduction data gives an analytic expression for the energy dependence of the proton photoproduction cross section. The fitting function depends on the photon-proton center of mass energy. The parameterization of the forward proton photoproduction cross section fit:

$$\left. \frac{d\sigma(\gamma p \rightarrow V p)}{dt} \right|_{t=0} = b_v (XW^\epsilon + YW^{-\eta}), \quad (2.18)$$

where  $W$  is the center of mass energy of the proton-photon system in Eq. 2.18. The remaining variables in Eq. 2.18 are power-law fit parameters. The  $XW^\epsilon$  term characterizes pomeron mediated interactions, and the  $YW^{-\eta}$  term characterizes meson mediated interactions [15].  $J/\psi$ 's high mass relative to the  $\pi$  and  $\rho^0$  renders the second term in Eq. 2.18 negligible as the term falls rapidly with increasing  $W$ . Eq. 2.18 allows for extrapolation and interpolation of the measured forward proton photoproduction cross section. The fit to the data provides estimates for energies that have not yet been probed experimentally. The proton photoproduction cross sections from the electron-

proton scattering data is a direct input to the STARlight model. In this method, a power-law fit to the proton photoproduction data is the input for the Glauber calculation.

Vector meson dominance and the optical theorem allow for the calculation of the total proton-meson scattering cross section from the fit given by Eq. 2.18. The optical theorem relates the total cross section,  $\sigma$ , to the corresponding forward scattering cross section,  $d\sigma/dt|_{t=0}$ , where  $t$  is the momentum transfer squared. The most likely fluctuations of the photon are to vector mesons because of the quantum numbers of the photon. Due to this consideration, vector meson dominance asserts that only the vector meson fluctuations of the photon need to be considered. The forward scattering cross section is given by the following

$$\begin{aligned} \frac{d\sigma(\gamma p \rightarrow V p)}{dt} \Big|_{t=0} &= \frac{4\pi\alpha}{f_v^2(M_V, \Gamma_{l+l-})} \frac{d\sigma(V p \rightarrow V p)}{dt} \Big|_{t=0}, \\ \sigma(V p)_{tot}^2 &= 16\pi \frac{d\sigma(V p \rightarrow V p)}{dt} \Big|_{t=0}, \end{aligned} \quad (2.19)$$

where  $M_V$ , is the mass of the vector meson, and  $\Gamma_{l+l-}$ , is leptonic decay width. The result of combining vector meson dominance and the optical theorem in Eq.2.19 provides the cross section for a meson to scatter off a proton.

The Glauber model allows for Eq. 2.19, the proton-meson scattering cross section, to be used to calculate a nucleus-meson scattering cross section. The Glauber model is used to calculate nuclear cross sections from nucleon interaction cross sections by use of  $T_{AA}$ . The combination of the mean number of nucleons in the overlapping region of a nucleus-nucleus collision,  $T_{AA}$ , the nucleon cross section,  $\sigma$ , and the Poisson distribution make-up the core of the Glauber model. For the total nucleus-meson scattering cross section, the equation has the following form:

$$\sigma_{tot}(VA) = \int d^2\vec{r} (1 - e^{-\sigma_{tot}(Vp)T_{AA}(\vec{r})}). \quad (2.20)$$

In Eq. 2.20, the term  $e^{\sigma_{tot}(Vp)T_{AA}}$  gives the probability of having no meson-nucleon scatterings from the Poisson distribution. The probability of having at least one scattering is given by subtracting

one from the term  $e^{\sigma_{tot}(VP)T_{AA}}$  in Eq. 2.20.

Reversing the process used for the proton, Eq. 2.20, the meson nucleus scattering cross section, relates to forward nuclear photoproduction cross section through the optical theorem. Using the optical theorem, the nuclear photoproduction cross section is given by

$$\begin{aligned} \frac{d\sigma(\gamma A \rightarrow VA)}{dt} \Big|_{t=0} &= \frac{\alpha \sigma_{tot}^2(VA)}{4\pi f_v^2}, \\ \sigma(\gamma A \rightarrow VA) &= \frac{d\sigma(\gamma A \rightarrow VA)}{dt} \Big|_{t=0} \int_{t_{min}}^{\infty} dt |F(t)|^2, \end{aligned} \quad (2.21)$$

where  $F$  is the Fourier transform of the nuclear density function,  $\rho_A$ . Eq. 2.21 is joined with the photon flux incident on the nucleus resulting in the following

$$\sigma(AA \rightarrow AAV) = 2 \int dk \frac{dN_\gamma}{dk} \sigma(\gamma A \rightarrow VA). \quad (2.22)$$

The factor of 2 in Eq. 2.22 comes from the fact that both of the two colliding nuclei contribute. Vector meson production rates in UPC collisions can be calculated by Eq. 2.22. In this thesis the measured UPC  $J/\psi$  cross section is compared to the STARlight predictions.

## 2.3 The Adeluyi and Bertulani model

To calculate the UPC  $J/\psi$  photoproduction cross section, the Adeluyi and Bertulani model uses the nuclear gluon density to characterize the nucleus and the Weizsäcker-Williams approximation for the probing photon flux. The AB method combines these components such that the nuclear gluon density is a direct variable. The nuclear gluon density term in the AB formulation allows for the use of a variety of nuclear gluon density models. A range of nuclear gluon densities are present in the available models resulting in a wide range of possible cross section values. The UPC  $J/\psi$  photoproduction cross section is correlated with the gluon density of the nucleus, increasing with higher densities and decreasing with lower densities. In the AB approach, the calculation of the UPC  $J/\psi$  photoproduction cross section allows experiments to constrain many different nuclear

gluon density models.

In the AB method, the photon interacts with the nucleus by fluctuating to a quark-antiquark pair. For  $J/\psi$ , the photon fluctuates to a  $c\bar{c}$  pair. The probability for the photon to fluctuate to a  $c\bar{c}$  pair depends on the  $M_{J/\psi}$ , the mass of  $J/\psi$ ,  $\Gamma_{l+l^-}$ , the  $J/\psi$  leptonic decay width, and  $\alpha$ , the electromagnetic coupling constant. These three variables connect the  $c$  quark to the electromagnetic force mediator, the photon. Recast as a  $c\bar{c}$  pair, the photon couples to the nuclear gluon density. The AB method uses the fluctuation of the photon to a  $c\bar{c}$  pair as the foundation for calculating the forward  $J/\psi$  photoproduction cross section.

The  $c\bar{c}$  pair arising from the photon fluctuation scatters off the gluons of the nucleus. The density of gluons in the nucleus determines how likely and therefore how large the cross section is for the quarks to scatter and form a  $J/\psi$ . The forward scattering cross section is the portion of those scattering events which transfer the minimum amount of momentum between the photon and the nucleus. The forward cross section for  $J/\psi$  photoproduction in the nucleus has the following form [16]:

$$\left. \frac{d\sigma_{\gamma A \rightarrow J/\psi A}}{dt} \right|_{t=0} = \xi_{J/\psi} \left( \frac{16\pi^3 \alpha_s^2 \Gamma_{l+l^-}}{3\alpha M_{J/\psi}^5} \right) [xG_A(x, \mu^2)]^2, \quad (2.23)$$

where  $\xi_{J/\psi}$  is an experimentally derived correction factor,  $\alpha_s$  is the strong coupling constant,  $x$  is the momentum fraction of the nucleus the scattering gluons carry, and  $G_A$  is the gluon density of the nucleus. Both the  $c$  and  $\bar{c}$  couple to the gluon density, and the double coupling results in the squared dependence of the cross section on the gluon density in Eq. 2.23. Fitting Eq. 2.23 to proton-electron scattering data sets  $\xi_{J/\psi}$  [16]. The forward scattering cross section given by Eq. 2.23 connects the photon flux to the gluon density and provides the input to calculate the total cross section by the optical theorem.

The optical theorem relates the forward cross section in Eq. 2.23 to the total photoproduction cross section. The total cross section gives the probability that a photon incident on the nucleus will produce a  $J/\psi$  regardless of the momentum transferred in the interaction. The total cross section

equation is given by

$$\sigma_{\gamma A \rightarrow J/\psi A}(k) = \frac{d\sigma_{\gamma A \rightarrow J/\psi A}}{dt} \Big|_{t=0} \int_{t_{min}(k)}^{\infty} dt |F(t)|^2, \quad (2.24)$$

where  $t_{min} = (M_{J/\psi}^2/4k\gamma_L)^2$ , which is the minimum amount of momentum transfer required to produce a  $J/\psi$  given the photon wave number  $k$ . The  $k$  dependence of  $t_{min}$  translates to the rapidity dependence of the total cross section. The total cross section for photoproduction, Eq. 2.24, provides the input to Eq. 2.28, which gives the rapidity dependence of the UPC photoproduction cross section. Eq. 2.24 as input to Eq. 2.28 allows for experimental comparison of the AB method to measurements of UPC photoproduction cross sections. With the AB method's direct use of the nuclear gluon density in Eq. 2.23, the AB method allows for experimental exploration of any gluon density model.

## 2.4 Leading Twist Approach Derivation

The Leading Twist Approach is another method for calculating UPC photoproduction cross sections. Contrary to the STARlight model, the LTA model introduces additional nuclear effects originating from modification of the nuclear gluon density. The LTA method uses the Weizsäcker-Williams approximation to calculate the photon flux created by the colliding nuclei. As in the STARlight method, the probability of having no hadronic collisions modulates the flux. The photon flux for the LTA method has the following form [17]:

$$n_{\gamma/A}^i(\omega_\gamma) = \frac{2\alpha Z^2}{\pi} \int_{b_{min}}^{\infty} db \frac{x^2}{b} \left[ K_1^2(x) + \frac{K_0^2(x)}{\gamma_L^2} \right] P_0(b) P_C^i(b), \quad (2.25)$$

where  $x = \frac{\omega b}{\gamma_L}$ , and  $K_0^2(x)$  term contributes a photon flux in the transverse direction, and  $P_C^i(b)$  is an modulation factor that requires various additional interactions. These interactions result in emission of neutrons from the receding nuclei as the nuclei relax from excited states. The terms  $P_C^i$  and  $K_0$  provide additional ways to distinguish UPC events from nuclear collisions experimentally

but leave the underlying interaction mechanism the same. For example, the additional terms in the LTA formulation of the photon flux produce calculations of asymmetric neutron emission, which separate UPC events from nuclear collisions.

The LTA model derives the nucleon cross section from derivations of the nucleon gluon densities from electron-proton scattering data and leading order perturbative quantum field theory calculations. The forward photoproduction cross section of the nucleon has the following form [17]:

$$\frac{d\sigma_{\gamma N \rightarrow J/\psi N}(t=0)}{dt} = \frac{16\Gamma_{l^+l^-}\pi^3}{3\alpha M_{J/\psi}^5} [\alpha_s \mu^2 x G_N(x, \mu^2)]^2, \quad (2.26)$$

where  $G_N$  is the gluon density of the nucleon,  $x$  is the fraction of the nucleon's momentum the gluon carries, and  $\mu$  is related to momentum at which the nucleon is being probed, which is equal to  $M_{J/\psi}/2$  for  $J/\psi$  photoproduction. By connecting the gluon density to the cross section, Eq. 2.26 allows for the gluon density to be experimentally probed.

The LTA model exploits the optical theorem to relate the forward photoproduction cross section of the nucleon to the nuclear cross section. The relation is

$$\sigma_{\gamma A \rightarrow J/\psi A}(\omega) = \frac{d\sigma_{\gamma N \rightarrow J/\psi N}}{dt}(\omega, t_{min}) R_g^2 \int_{t_{min}}^{\infty} dt |F(t)|^2, \quad (2.27)$$

where  $R_g$  is the nuclear modification function, the ratio between the gluon density of the nucleon,  $G_N$ , to the gluon density of the nucleus,  $G_A$ . As with the STARlight method, the optical theorem relates the forward cross section,  $\frac{d\sigma_{\gamma N \rightarrow J/\psi N}}{dt}(\omega, t_{min})$ , to the total cross section,  $\sigma_{\gamma A \rightarrow J/\psi A}$ .

From Eq. 2.27, the LTA method can predict the angular distribution of photoproduced  $J/\psi$  with respect to the beam axis. The angular distribution is expressed in the form of the rapidity dependency of the UPC photoproduction cross section given by

$$\frac{d\sigma_{A_1 A_2 \rightarrow A_1 A_2 J/\psi}}{dy} = n_{\gamma/A_1}(y) \sigma_{\gamma A_2 \rightarrow J/\psi A_2}(y) + n_{\gamma/A_2}(-y) \sigma_{\gamma A_1 \rightarrow J/\psi A_1}(-y), \quad (2.28)$$

where  $y = \ln\left(\frac{2\omega}{M_{J/\psi}}\right)$ . Eq. 2.28 is comprised of two terms, one for photons from the forward going

nucleus interacting with the backward going nucleus, and a second for the reverse situation. The integration of Eq. 2.28 over  $y$  produces the factor of 2 that is present in Eq. 2.22. The rapidity distribution of the photoproduction cross section given in Eq. 2.28 provides a more detailed prediction and allows for more direct experimental comparisons.

## 2.5 Photon-induced nuclear break-up

In addition to the photoproduction of quark anti-quark resonances such as the  $J/\psi$ , photo-nuclear interactions can also result in emission of a neutron from the struck target nucleus. To calculate the cross section for neutron emission in UPC events, the photon flux calculated from the Weizsäcker-Williams approximation is combined with the nuclear photon absorption cross section. The absorption of photons can be described by two processes, namely the Giant Dipole Resonance (GDR), and the dissociation of deuterium. In this section, the theoretical description of photon-induced nuclear break-up is discussed.

Following the formulation in [18], the cross section for a nucleus to absorb a photon,  $\sigma_{PN}$ , is given by

$$\sigma_{PN} = \sigma_{GDR} + \sigma_{QD}. \quad (2.29)$$

The Giant Dipole Resonance (GDR) cross section,  $\sigma_{GDR}$  is the result of the collective motion of the protons relative to the neutrons and dominates at lower photon frequencies. The Quasi-Deuterium (QD) cross section,  $\sigma_{QD}$ , represents the nucleus as a collection of proton-neutron pairs (deuterium) and dominates at higher photon energies.

There are two models for the GDR: the Goldhaber and Teller model, and the Steinwedel and Jensen model. Goldhaber and Teller treats the protons and neutrons as two separate and ridged density profiles that, when excited, oscillate with respect to each other [19]. Steinwedel and Jensen modeled the protons and neutrons as fluids contained in a single sphere that have shifting density profiles [19].

In the Goldhaber and Teller model, the potential that holds protons and neutrons together de-

depends on the difference of the neutron and proton densities squared. Assuming the neutron and proton densities have the same shape, if the two fully overlap, there is no difference in the densities and the potential energy is zero. If the two density distributions are separated, the overlap in the shape will not cancel. In the separated configuration, there will be a non-zero potential energy. The potential energy has the form of a harmonic oscillator with a spring constant that depends on the initial density distribution [19] given by

$$U = \frac{1}{2}Kz^2, \quad K = k \int d^3r (\nabla \rho_0)^2. \quad (2.30)$$

If the nucleus has a shape cut off in density at its edge, then the integral is dominated by the region at the surface, and the spring constant,  $K$ , becomes proportional to  $A^{2/3}$ , where  $A$  is the mass number of the nucleus. The surface area of a sphere is proportional to its volume to the  $2/3$  power explaining the mass dependence. Due to this dependence, the frequency of the giant dipole resonance in the Goldhaber and Teller model is given by

$$\omega = \sqrt{\frac{K}{M}} \propto \sqrt{\frac{A^{2/3}}{A}} = A^{-1/6}. \quad (2.31)$$

This dependence describes light nuclei well, but it does not describe heavier nuclei [19]. The Steinwedel and Jensen model can be used to describe heavier nuclei. In this model, the proton and neutron fluids are confined to a single sphere where they are allowed to slosh back and forth creating the same effect as the Goldhaber and Teller model. Here there is no global separation of the proton and neutron fluids. The dipole is created by under-densities and over-densities of the proton and neutron fluids. It can be shown that this results in a frequency of oscillation which depends on one over the radius of the nucleus [19]:

$$\omega \propto \frac{1}{R} \propto A^{-1/3}. \quad (2.32)$$

As before, the relationship in Eq. 2.32 arises from the geometry of a sphere. The dependence of



the giant dipole resonance that is seen in the Steinwedel and Jensen model describes medium and heavier mass nuclei well. Empirically, both models are put together to give the following mass number dependence of the dipole resonance [19]

$$E_{GDR} = 32.2A^{-1/3} + 20.6A^{1/6}. \quad (2.33)$$

In order to compute the effect of an excitation in either model, the harmonic oscillator solutions found earlier can be driven by an interacting force. The resulting differential equation can then be solved using a Fourier transform to eliminate the time derivatives. In this model the driven harmonic has the following Lorentzian form:

$$\sigma_{GDR}(E_\gamma) = \frac{\sigma_{max} E_\gamma \Gamma_{GDR}^2}{\left(E_\gamma^2 - E_{GDR}^2\right)^2 + E_\gamma^2 \Gamma^2}, \quad (2.34)$$

where  $\sigma_{max}$  is the maximum cross section reached when  $E_\gamma = E_{GDR}$ ;  $E_{GDR}$  is the peak resonance energy, and  $\Gamma_{GDR}$  is the width of the resonance. The width of this distribution lies in a range from 4-8 MeV and depends on the orbital arrangement to the neutrons and protons in the given nucleus [19].

For higher energy photons, the quasi-deuterium cross section is needed. The nucleus is treated as a collection of proton-neutron pairs, which are screened by the rest of the nucleus, in the quasi-deuterium approach. This behavior is modeled by [18]

$$\sigma_{QD}(E_\gamma) = L \frac{(L-A)Z}{A} \sigma_d(E_\gamma) F(E_\gamma), \quad (2.35)$$

where  $\sigma_d$  is the deuterium disintegration cross section for  $\gamma + d \rightarrow p + n$ ;  $F$  is a function from Pauli blocking of fermions, and  $L$  is an empirical parameter set by data to 6.5 [18]. Certain energy levels are not available to the products of the deuterium disintegration process because of the presence of the rest of the nucleus. The result is a reduction of the cross section relative to free deuterium.

$F$  can be modeled with an exponential cutoff below 20 MeV, a polynomial in the intermediate

range with nearly linear dependence on  $E_\gamma$ , and an inverted exponential above 140 MeV, pushing  $F$  to one at higher values of  $E_\gamma$  [18]. Essentially, the model at low photon energies disallows deuterium disintegration because the products have no available state to occupy, and at high energies the rest of the nucleus becomes transparent and looks more and more like a collection of deuterium. The deuterium disintegration cross section is found empirically and is fit to the following function [18]:

$$\sigma_d(E_\gamma) = 61.2 (E_\gamma - 2.224)^{3/2} / E_\gamma. \quad (2.36)$$

In order to produce a final state for the target nucleus, a branching ratio is needed. The branching ratio gives the probability that the photo-excited nucleus will end up in a particular state. This determines the sort of emission that will result from the de-excitation process [18].

All the tools are now assembled to calculate the cross section for neutron emission. The first step in the calculation is to assume that the number of photons absorbed by either nucleus in the collision obeys the Poisson distribution [20, 18]. The average number of absorptions as a function of impact parameter,  $m(b)$ ,

$$m(b) = \int_{\omega_{min}}^{\omega_{max}} N(\omega, b) \sigma_{PN}(\omega) d\omega. \quad (2.37)$$

where  $\sigma_{PN}$  is the photo-nuclear cross section, and  $N$  is the photon flux (see Eq. 2.13).

In [18], the probability of any final state  $i$  due to the absorption of a single photon is given by

$$P_i(b) = \int_{\omega_{min}}^{\omega_{max}} P_a(b, 1) q(b, \omega) f_i(\omega) d\omega = e^{-m(b)} \int_{\omega_{min}}^{\omega_{max}} N(b, \omega) \sigma_{PN}(\omega) f_i(\omega) d\omega, \quad (2.38)$$

where  $P_a$  is the probability that the target absorbs a single photon as calculated by following the Poisson distribution;  $q$  is the probability that the photon will have the frequency  $\omega$ , and  $f_i$  is the branching ratio to a given final state. The following equation describes  $q$  [21]

$$q(b, \omega) = \frac{N(b, \omega) \sigma_{PN}(\omega)}{m(b)} \quad (2.39)$$

Integrating over the impact parameter to get an area that is weighted by the probability functions gives [20, 18]

$$\sigma_i = 2\pi \int_{b_0}^{\infty} b P_i(b) db. \quad (2.40)$$

Three parameters arise when calculating the cross section in Eq. 2.40, the minimum impact parameter  $b_0$ , the minimum emitted photon frequency  $\omega_{min}$ , and the maximum emitted photon frequency  $\omega_{max}$ . A minimum impact parameter ensures that the Bessel function in the photon flux in Eq. 2.13 is not evaluated at zero. At zero, the modified Bessel function does not converge. Physically, a minimum impact parameter is selected in order to separate the domains between electromagnetic interactions and the strong interactions that happen inside the nucleus. To serve this end, the minimum impact parameter is set to the radius of the nuclei [20, 18]. This excludes collisions where the nuclei overlap in the calculation, and ensures that only electromagnetic interactions are involved.

## 2.6 Experimental Results

### 2.6.1 UPC measurements at RHIC

One of the first results from RHIC was a UPC measurement, the measurement of the neutron spectrum from photon-induced nuclear break-up [3]. Neutrons due to the nuclear photon absorption are emitted with momenta on the order of the giant dipole resonance, about 60 MeV. Momenta of 60 MeV compared to the 100 GeV beam energy at RHIC result in neutron emission at very small angles,  $\sim 2\text{mrad}$ , relative to the beam. These neutrons are captured by calorimeters, which are set in line with the beam called Zero Degree Calorimeters (ZDCs). These detectors are described in Section 3.4. Figure 2.2 shows the charge recorded by the ZDCs. The peak at  $\sim 30$  in Fig. 2.2 is due to emission of a single neutron. Each successive peak is due to emission of an additional neutron. From these peaks, the cross section for nuclear break-up by neutron emission by both nuclei was measured. The fraction of nuclear interaction in all events with neutrons on both sides of the interaction point was found to be  $0.661 \pm 0.014$  [3], which is in agreement the value 0.659

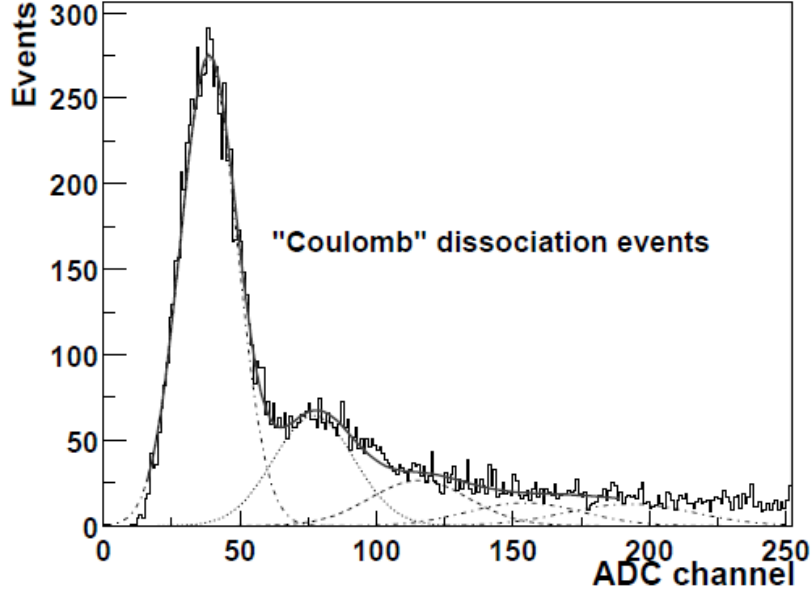


Figure 2.2: ZDC neutron spectrum at RHIC with each a Gaussian fit to the 1, 2, 3, 5, and 5 neutron peak [3].

predicted by the model described in [18].

Nuclear collisions were separated from photon-induced break up by counting hits in the central scintillating counter similar to a tracker. Events with hits on both sides of the interaction point were categorized as nuclear interactions, and those with no hits or hits on only one side were categorized as electromagnetic interactions. The difference in the charge measured on each of the two sides of the interaction point, by the two ZDCs, is divided by the total charge for both ZDCs (see Fig. 2.3). Figure 2.3 shows that events created by electromagnetic interactions result in asymmetric neutron emission, whereas nuclear interactions produce neutrons on both sides. In the analysis presented in this thesis, the energy asymmetry in the ZDCs is used to select UPC events. This will be discussed in Chapter 5.

Both the  $\rho^0$  and  $J/\psi$  meson photoproduction cross sections in UPC events were measured at RHIC. STAR measured the photoproduction of the  $\rho^0$  meson at collisions energies per nucleon of 62.4 GeV [22], 130 GeV [23], and 200 GeV [24]. The  $J/\psi$  was measured by PHENIX at 200 GeV [25]. The  $\rho$  measurements by STAR were in good agreement with the theory calculation method described in Section 2.2. The  $J/\psi$  measurement where limited by statistic as only 10  $J/\psi$

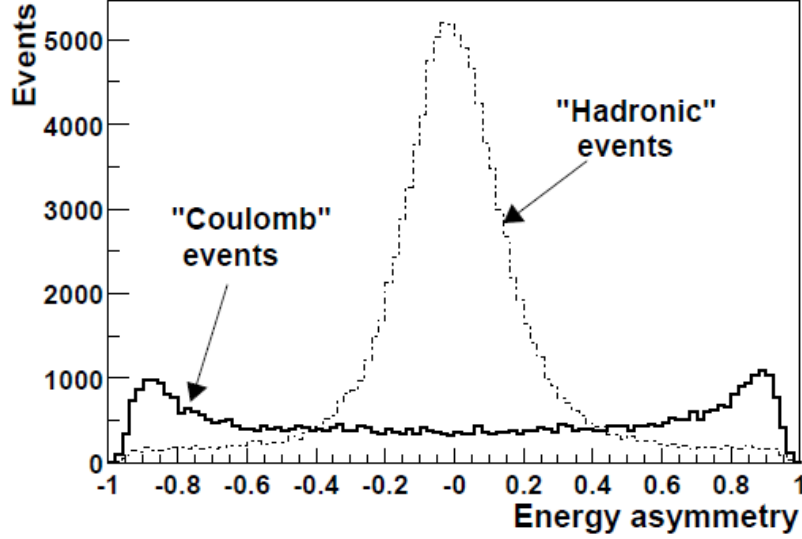


Figure 2.3: The energy asymmetry in the ZDCs for photon-induced interaction, coulomb events, and nuclear interaction, hadronic events [3].

candidates were found.

## 2.6.2 UPC $J/\psi$ at the LHC

The increase in beam energy from 200 GeV at RHIC to 2.76 TeV at the LHC results in an increase in the Lorentz  $\gamma$  of about 10. Because the photon flux depends on  $\gamma^2$ , the photon flux at the LHC increases by a factor of about 100 compared to RHIC. All major heavy ion experiments, ALICE and CMS, have studied the production of UPC events. ALICE has studied coherent  $J/\psi$  photoproduction in ultra-peripheral PbPb collisions at  $\sqrt{s_{NN}} = 2.76$  TeV. The cross section for this process was measured at both forward-rapidity,  $y = 3$ , and mid-rapidity,  $y = 0$ . With an integrated luminosity of  $55 \mu b^{-1}$ , ALICE measured  $78 \pm 10(\text{stat})^{+7}_{-11}(\text{syst})$  coherent  $J/\psi$  candidates at forward rapidity. The measured cross section was  $1.00 \pm 0.18(\text{stat})^{+0.24}_{-0.26}(\text{syst})$  mb. For a symmetric system like PbPb collisions, as opposed to pPb collisions, there is an ambiguity between which ion is the target and which is the photon emitter. Therefore, the cross section has a contribution from the low- $x$  and high- $x$  parts of the gluon density. At  $y = 3$  for PbPb collisions at the LHC, the cross section has a contribution from both  $x = 5 \times 10^{-5}$  and  $x = 2 \times 10^{-2}$ . This ambiguity is not present

at  $y = 0$ . ALICE has also measured the coherent  $J/\psi$  photoproduction cross section at  $y = 0$ , using a integrated luminosity of about  $23 \mu b^{-1}$ .  $291 \pm 18$  (stat)  $\pm 4$  (syst) and  $265 \pm 40$  (stat)  $\pm 12$  (syst) coherent  $J/\psi$  candidates were measured in the dimuon and dielectron channels, respectively. The combined cross section from both channels was measured to be  $2.38^{+0.34}_{-0.24}$  (stat+syst) mb. At  $y = 0$   $x \sim 10^{-3}$ , which is a smaller  $x$  than at forward rapidity, and more sensitive to the nuclear gluon shadowing (see Fig. 2.4).

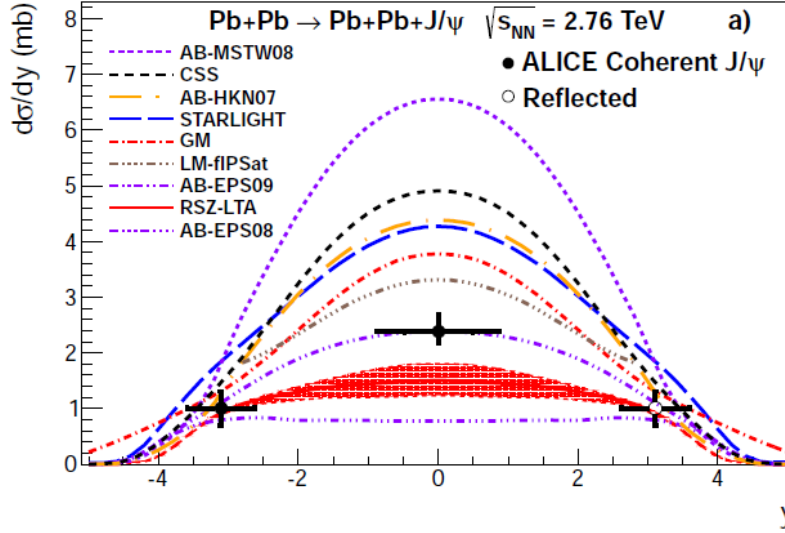


Figure 2.4: Coherent  $J/\psi$  photoproduction cross section in ultra-peripheral PbPb collisions at  $\sqrt{s_{NN}} = 2.76$  TeV, measured by the ALICE experiment at forward and mid-rapidity [1].

The ALICE data points have been compared to several theoretical models. The UPC photoproduction cross section calculations depend significantly on how the nucleus is represented in the calculation. The results from the STARlight, LTA, and AB methods vary from a relatively large cross section in the STARlight model, ranging through a variety of values in the AB method, to a relatively small cross section in the LTA method. Each of these methods utilizes the same probe of the nucleus, the equivalent photon flux that is calculated using the Weizsäcker-Williams approximation (see Section 2.1). The three methods deviate in how they calculate the forward photoproduction scattering cross section. The differences in the UPC photoproduction cross sections predicted by the different models demonstrates the amount of experimental sensitivity there is to distinguishing between the models. The dependence of the cross section on rapidity is clearly

Model	$\sigma_{AA \rightarrow AAJ/\psi}(mb)$
STARlight/STARlight MC	23
LTA	9
AB-MSTW08	34
AB-EPS08	7
AB-EPS09	14
AB-HKN07	23

Table 2.1:  $\sigma_{AA \rightarrow AAJ/\psi}(mb)$  the LTA, STARlight, AB methods. Four different gluon density models are used in the AB method. STARlight is a simulation software package that utilizes the STARlight model.

visible.

The cross section value calculated by Eq. 2.22 in the STARlight, LTA, and the various gluon density models in AB method vary significantly. Table 2.1 gives the predicted values for the three main methods taken from [26], [17], and [15]. The cross sections in Table 2.1 differ by a factor of 4 from the smallest to largest and create an experimental opportunity. The clear discrepancy between the models in Table 2.1 demonstrates the high amount of experimental sensitivity there is for distinguishing between the models.

The nuclear suppression factor,  $S$ , demonstrates the difference between how the models represent the nucleus.  $S$  is the ratio between the nuclear photoproduction cross section and the free nucleon photoproduction cross section. It is a measure of how the nuclear gluon densities evolve in each of the models. Figure. 2.5 from [27] shows the nuclear suppression, which is equivalent to  $R_g$  in Eq. 2.27, for the LTA and AB methods. Fig. 2.6 shows the nuclear suppression for the STARlight method [27]. Fig. 2.5 and Fig. 2.6 show that as the momentum of the probing photon goes up, increasing  $W_{\gamma p}$ , and momentum of the probed gluon goes down, decreasing  $x$ , the nuclear gluon density decreases relative to the free nucleon. The nuclear suppression factor,  $S$ , allows for the different models' representations of the gluon content of the nucleus to be directly compared to each other and to data.  $S$  can be measured from data by assuming a Weizsäcker-Williams photon flux and provides insight into nuclear gluon densities.

In addition, ALICE reported the measurement of the incoherent  $J/\psi$  photoproduction cross

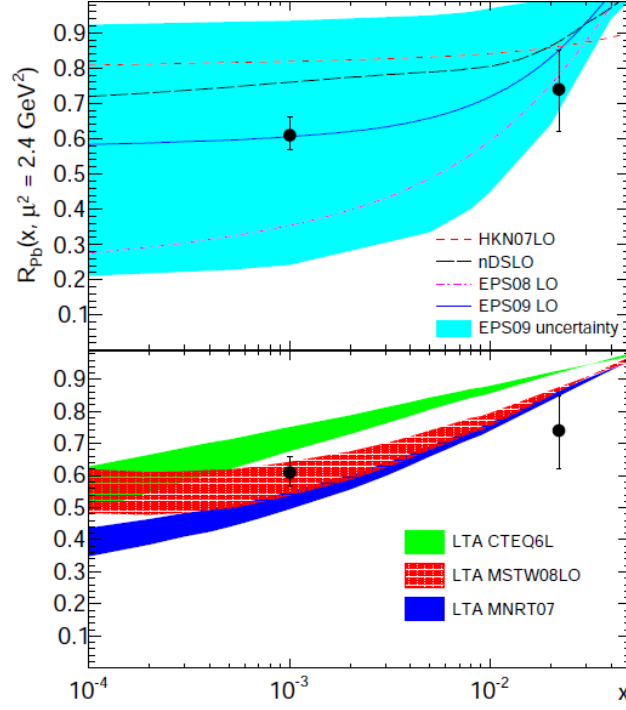


Figure 2.5: Nuclear suppression factor,  $S$ , in the AB and LTA methods.

section at mid-rapidity. This provided additional constraints to the models for gluon shadowing.

In Chapter 6, the coherent UPC  $J/\psi$  photoproduction cross section using CMS is described. The measurement in this thesis adds to existing ALICE results, covering an intermediate range of  $x$  values.



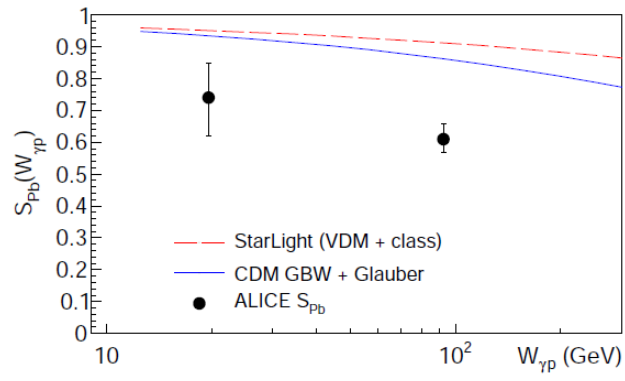


Figure 2.6: Nuclear suppression factor,  $S$ , in STARlight method.

## Chapter 3

# The Compact Muon Spectrometer detector

The Compact Muon Spectrometer (CMS) is housed at interaction point 5 of the LHC. The LHC is designed to pursue physics at the TeV scale. This is the scale where electroweak symmetry breaking is believed to occur [28]. While this means that the search for the standard model Higgs boson was the central driving design consideration, the wide range of possibilities for finding new physics signals requires a general purpose detector. The expedient discovery of new physics through low cross section interactions requires high luminosity. Muon capabilities developed for the Higgs boson can be used to study  $J/\psi$ . A versatile trigger is needed to accommodate the high interaction rates that accompany the high luminosities. By exploiting the versatility of the trigger and muon systems it is possible to explore processes like UPC  $J/\psi$  production, which push to the low energy edge of the experiment's capabilities.

The general purpose design of CMS is dominated by the massive 4T superconducting solenoid at its core. The magnets is 13m long with a 6m diameter, and pushes the limits of power and compactness [4]. These two conflicting limits are achieved through the novel design of interweaving structural and conducting elements together in the coil of the solenoid.

Within the solenoid resides three different sub detectors. The inner most is the world's largest silicon tracker [4]. The tracker is surrounded by a highly effective lead tungstate crystal electromagnetic calorimeter (ECAL). ECAL is encapsulated in a brass scintillating hadronic calorimeter

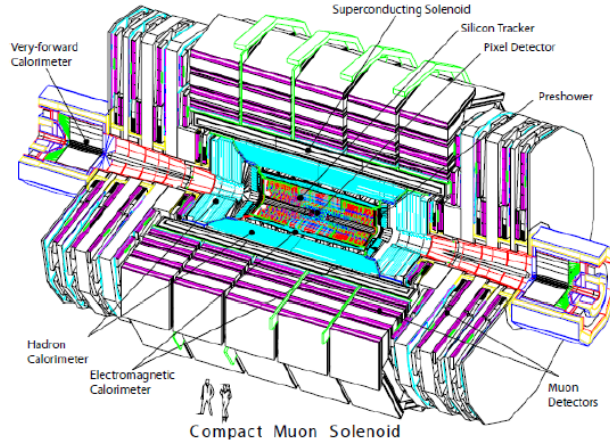


Figure 3.1: The Compact Muon Solenoid layout [4].

(HCAL). Outside the magnet, muon chambers are used to aid in the measurement and triggering of muon events. Altogether CMS weighs 12,500 metric tons, has a diameter of 14.6m, and a length of 21.6m [4].

### 3.1 Tracker

The Silicon Tracker is the innermost sub-detector of CMS, and has active elements as close as 4.4cm to the interaction point [4]. The tracker has a length 5.8m, a diameter of 2.6m and covers a range in pseudorapidity of  $|\eta| < 2.5$ . At the center of the tracker are three rings of silicon pixels around the beam with two disks of silicon pixels to cap the rings. The pixel portion of the silicon tracker is comprised of  $66 \times 10^6$  pixels. The silicon pixels are surrounded by silicon strips. The silicon strips are separated into 4 different sections: the Tracker Inner Barrel, the Tracker Inner Disk, the Tracker Outer Barrel, and the Tracker End Caps. The silicon strip detectors as a whole are comprised of  $9.3 \times 10^6$  silicon strips. The high number of pixels and strips allow for the ability to distinguish and collect enough distinct points to reconstruct the path of the 1000 or so charged particles per bunch crossing expected at peak luminosity [4].

The amount of material present in the tracker is substantial enough to alter the path of particles as they pass through the tracker. Fig. 3.3 shows the amount of material in the tracker as a function

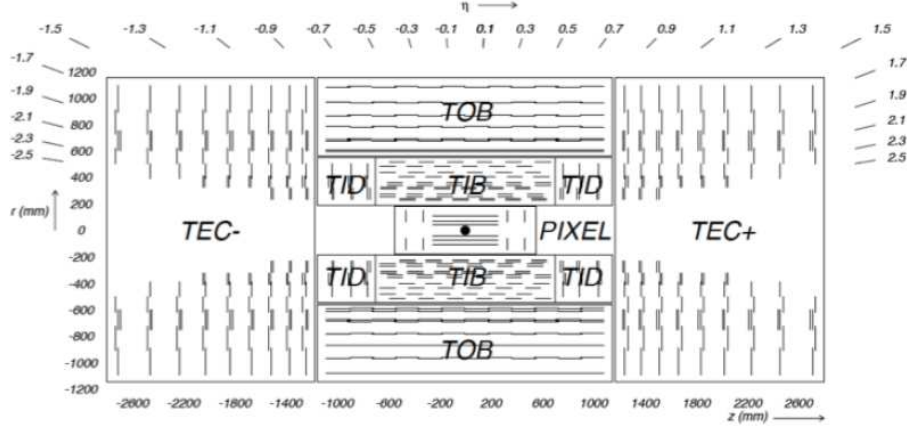


Figure 3.2: Layout of the silicon tracker with the pixels closest to the interaction point, marked with a black dot, and the strips segments beyond the pixels.

of radiation lengths ( $X_0$ ). The radiation length is the mean distance a high energy particle travels before giving up one  $e$ -fold of kinetic energy through electromagnetic interactions. For example, after one radiation length  $E \rightarrow E/e$ , where  $e \sim 2.7$  the base of the natural logarithm. As opposed to the deflection angle set by the strength of the magnetic field, the momentum resolution for lower momentum tracks is limited by the lose of energy due to scattering of these particles off the material of the detector. For UPC  $J/\psi$ , this is the primary factor contributing to the resolution of the reconstructed muon tracks.

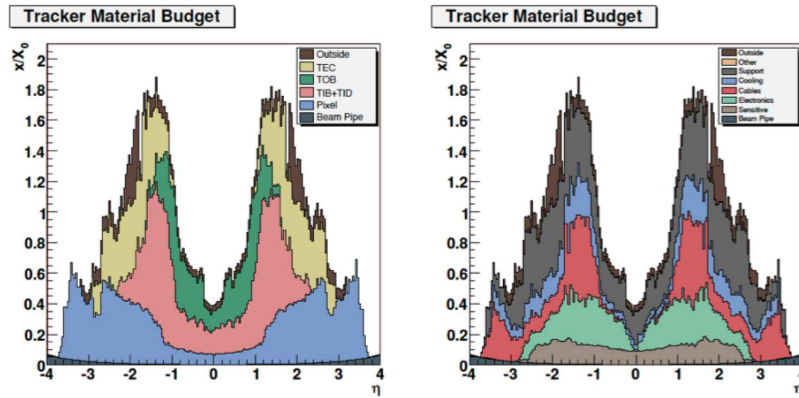


Figure 3.3: Material budget in the tracker broken down by sub-detector(left) and category (right).

## 3.2 ECAL

The next detector beyond the tracker is the electromagnetic calorimeter system, ECAL. The calorimeter system is made of 61,200 lead tungstate ( $\text{PbWO}_4$ ) crystals in the central barrel and 7,324 on each of the two endcaps [4]. The barrel (EB) covers a pseudorapidity range  $|\eta| < 1.479$  and has an  $\eta - \phi$  segmentation of approximately  $0.0174 \times 0.0174$ , depending slightly on the position of the fixed sized crystals. Lead tungstate is very dense giving the ECAL crystals a high number of interaction lengths within a short depth. The crystals of the barrel have a depth of 230 mm corresponding to  $25.8 X_0$ . The endcaps (EE) cover the pseudorapidity region  $1.479 < |\eta| < 3$ . In the endcap the crystals have an exposed area of  $28.62 \times 28.62 \text{ mm}^2$ , and a depth of 220 mm corresponding to  $24.7 X_0$ . The energy resolution of the ECAL as measured by test beam data can be seen in Figure 3.4. The fractional energy resolution reduces quickly above 10 GeV and levels off

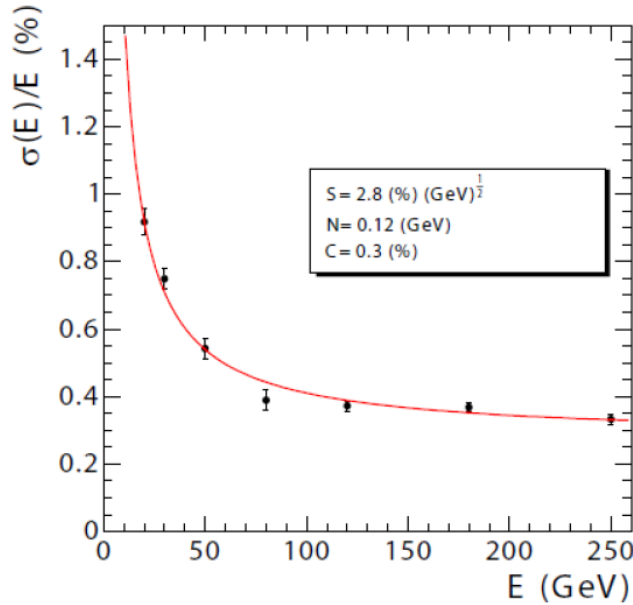


Figure 3.4: The energy resolution of ECAL as a function of energy [4].

at about 0.5% for energies above 100 GeV. For  $J/\psi$  with rapidity near 2, the electron will carry at least 10 GeV and can be resolved by the ECAL.

### 3.3 HCAL

The HCAL like the ECAL has both a barrel (HB) and endcaps (HE). The pseudorapidity region  $|\eta| < 1.3$  is covered by HB [4]. HB has an  $\eta - \phi$  segmentation of  $0.0897 \times 0.0897$ , and is 25 times more sparsely granulated than EB. HE covers the pseudorapidity region  $1.3 < |\eta| < 3$ . HE, like EE and the tracker endcaps, is aligned perpendicular to the beam axis resulting in granularity that changes with  $\eta$ . In the region  $1.3 < |\eta| < 1.6$  HE has an  $\eta - \phi$  segmentation of  $0.0897 \times 0.0897$ . The  $\eta - \phi$  segmentation roughly doubles to  $0.17 \times 0.17$  in the region  $1.6 < |\eta| < 3$ . The energy resolution of the barrel and endcaps can be seen in Figure 3.5. The thickness of the hadronic calorimeter is best described in interaction lengths, the mean distance for a particle to give up an  $e$ -fold of energy through nuclear interactions. At  $\eta = 0$  the barrel has a thickness 5.82 interaction lengths ( $\lambda_I$ ), and increases as the path length through the material increases to  $10.6 \lambda_I$  at  $|\eta| = 1.3$ .

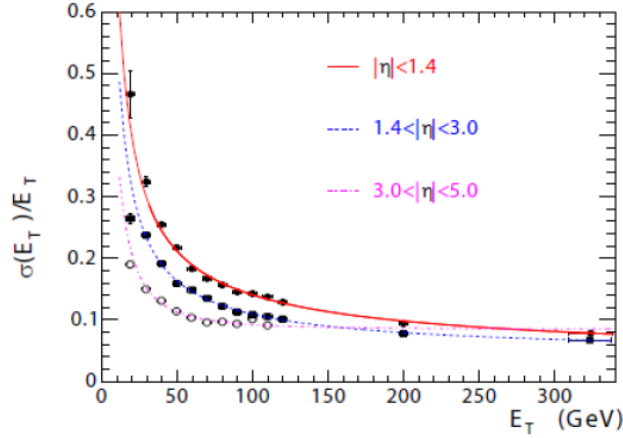


Figure 3.5: The  $E_T$  resolution of HCAL as a function of  $|\eta|$  and  $E_T$  [4].

In addition to HB and HE, HCAL has two additional calorimeters. Because the space between ECAL and the magnet is restricted to 1.18 m, an outer hadronic calorimeter section (HO) is placed beyond the magnet in the region  $|\eta| < 1.3$  [4]. The main function of HO is to collect energy from the highest energy hadrons before they reach the muon system. HO is not used in this analysis, but does contribute to the material budget. To increase the total calorimetric coverage, HCAL also has a quartz fiber calorimeter (HF) in the forward region,  $3 < |\eta| < 5$ . For the majority of HF's

13  $\eta$  rings the  $\eta - \phi$  segmentation is  $0.175 \times 0.175$ . In the lowest  $|\eta|$  ring the segmentation is  $0.111 \times 0.175$  in  $\eta - \phi$ . In the highest two  $|\eta|$  rings the segmentation in  $\phi$  is 0.349, with an  $\eta$  segmentation of 0.175 in the outer and 0.300 in the innermost ring. The longitudinal direction is effectively segmented by using both short and long fibers. The energy deposited deeper than 22cm is measured in both the short and long fibers, where as the long fibers are present throughout. This allows electromagnetic showers to be distinguished from purely hadronic showers [4].

The energy resolution for HF can be seen in Figure 3.5. As with the ECAL, the fractional resolution increases with energy. This is due to the random nature of shower development. At larger energies, the fluctuations in the shower of particles collected in the calorimeter tend to average out.

### 3.4 ZDC

Beyond HF, the Zero Degree Calorimeters (ZDCs) covers the very forward rapidity region. The ZDCs sit between the beam pipes on either side of the interaction point covering the area around  $\theta = 0$ ,  $|\eta| > 8.3$ . In heavy ion collisions the ZDC has the ability to measure neutral particles that do not participate in the collision [4]. This detector plays an important role in the analysis described in this thesis by measuring energy due to neutrons produced by photon-induced nuclear break. These measurements are used to identify events with asymmetric neutron emission, reducing the contribution to the sample by peripheral heavy-ion

The ZDC has a total of 18 channels. Half of these 18 channels are on either side of the interaction point. The 9 channels on the side of CMS that correspond to positive  $\eta$  are denoted  $ZDC^+$ , where as the 9 channels on the negative side are denoted  $ZDC^-$ . The 9 channels on each side are further sub-divided into an electro-magnetic (EM) section and a hadronic (HAD) section. The EM section is positioned in front of the HAD section with respect to the interaction point and is segmented transverse to the beam direction. The 5 EM sections are positioned in front to absorb the energy from electro-magnetically induced showers, which develop over a shorter distance than

hadronically induced showers. The transverse segmentation allows for a measurement of the transverse shower width and the size of the beam spot at the ZDC. The HAD section is segmented in the direction of the beam and consists of 4 channels. The longitudinal segmentation allows for absorption of the full extended hadronic shower and the ability to measure the longitudinal shower shape.

Each of the 18 channels contains a tungsten target and quartz fibers. The dense tungsten target is used to initiate the shower. The quartz fibers shine Cerenkov light as the high momentum charged particles from the shower pass through it. The light from the quartz fibers is channeled to photo-multiplier tubes, one for each ZDC channel. Through a cascade of photon induced electrical discharges, the photo-multiplier converts the Cerenkov light to an electrical pulse.

This electrical pulse travels  $\sim 200$  m down a coaxial cable from the LHC tunnel to the counting house in the CMS service cavern. There the electrical pulse is digitized by the Charge Integrator and Encoder (QIE). The QIE integrates the current each 25 ns. The charge is then mapped logarithmically to the 128 bits. This bit is sent across a small fiber optic cable to the HTR firmware card. Here each 25 ns signal is stored in a 250 ns buffer, and the timing is synchronize with the rest of the detector to ensure the ZDC signal arrives at the central data acquisition system at the same time as the other sub detectors from the same collision.

## 3.5 Muons

The muon system resides just outside of the superconducting magnet. It consists of three complementary systems: drift tube (DT) chambers in the barrel, cathode strip chambers (CSC) in the endcaps, and resistive plate chambers (RPC) in both the barrel and endcap regions [4]. Each of these gaseous detectors function in the same way. As the muon penetrates the gas volume electrons are knocked off of the gas atoms and these electrons are collected in the positively charged anode, whereas the ionized gas moves to the cathode. The DTs in the barrel and the CSCs in the endcap have better spatial precision relative to the RPCs, which are quicker and have more precise timing.



The combination of the DTs and RPCs in the barrel and the CSCs and RPCs in the endcap allow for fast triggering and muon identification during data reconstruction.

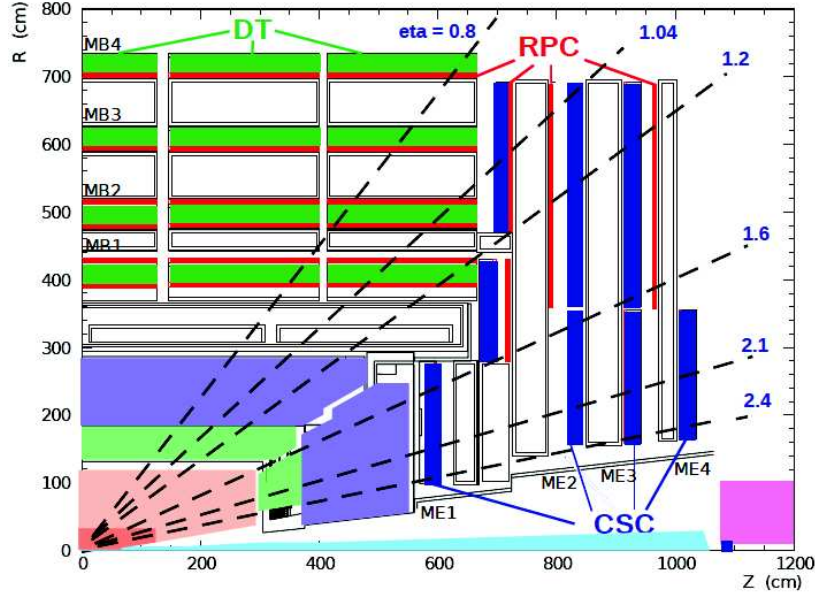


Figure 3.6: The CMS muon system showing the four DT stations in the barrel (MB1-MB4), the four CSC stations in the endcap (ME1-ME4), and the RPC stations.

As seen in Fig. 3.6, the DTs reside only in the barrel, covering the region  $|\eta| < 1.2$ . Consisting of a total of 172,000 cells, the DT cells are collected into 250 chambers. The DT chambers are interwoven into the magnet field return yoke and are labeled by 5 segmentations in  $z$ , YB-2 to YB+2. Each  $z$  segment is divided into 12  $\phi$  segments labeled 1 at  $\phi = 0$  and going to 12 rotating in positive  $\phi$  with segments 4 and 10 contain 2 chambers. The segmentation in  $r$  is divided into four parts, MB1-MB4. Fig. 3.7 shows how each chamber is made of three super layers. Super layers  $SL \Phi_1$  and  $SL \Phi_2$  measure  $(r, \phi)$ , whereas  $SL \Theta$  measures  $z$ .

The RPCs complement the DTs in the barrel and the CSCs in the endcap primarily for the purpose of triggering. Throughout the barrel and endcap there are a total of 1020 RPC modules, 480 in the barrel and 540 in the endcap. Denoted by the red lines in Fig. 3.6, the RPCs are mounted on both sides of the DTs in the barrel for the inner most layers, MB1 and MB2. For the outer two layers of the barrel, MB3 and MB4, a single layer of RPCs is mounted on the inner side of the DTs. Each corresponding DT segment has two RPCs modules, except in MB2 where some

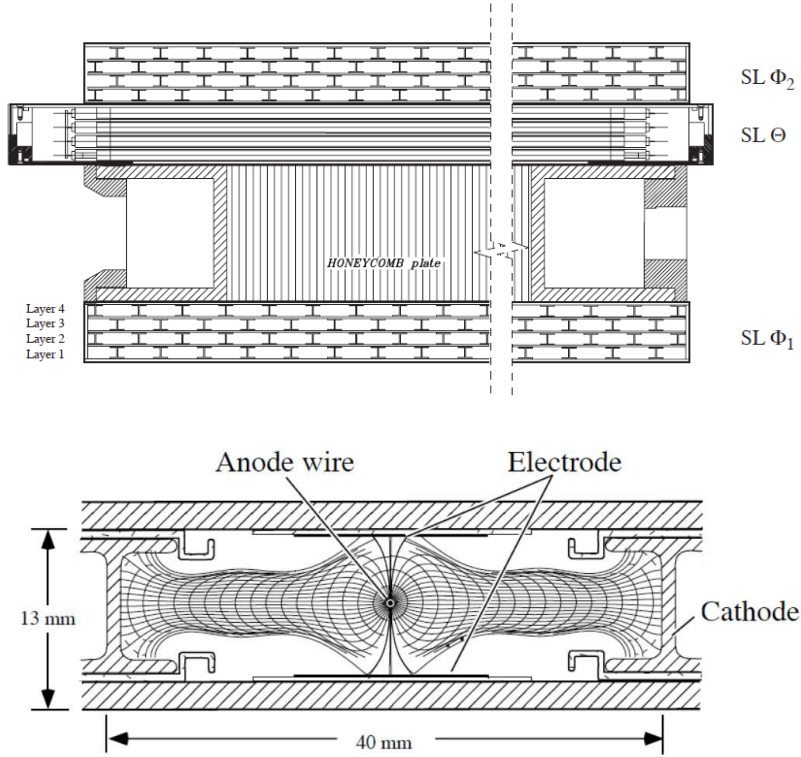


Figure 3.7: Schematic of the DT chambers and an individual DT cell.

segments contain 3 RPC modules. The outer ring of the muon endcap are instrumented with RPCs covering up to  $|\eta| = 1.6$ .

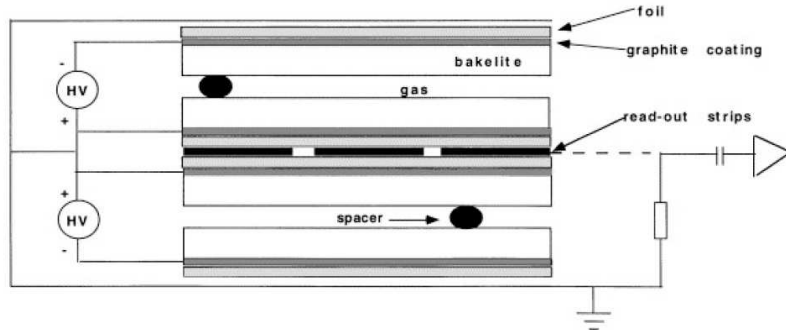


Figure 3.8: Schematic of a RPC cell.

There is a total of 468 CSC modules in the muon system endcap. For the sectors in  $z$ , ME2, ME3, and ME4 in the endcap, the modules in the ring closest to the beam are covering  $20^\circ$  in  $\phi$ . The modules in ME1 and the modules in beyond in the inner ring in ME2 and ME3 have a  $10^\circ \phi$  segmentation. The 2 million wires of the CSCs are grouped into 400,000 channels and are powered

with 9000 high voltage supplies. The resolution of the CSCs is on the order of 1mm for position measurements in the plane perpendicular to the beam and is 99% efficient for muons that pass through all four sectors, ME1, ME2, ME3, and ME4. Because of the relatively low momentum of the muons originating from  $J/\psi$  in UPC events, the muons in the analysis discussed in this thesis are all in the range  $1.6 < |\eta| < 2.4$  and rely on the CSCs for triggering.

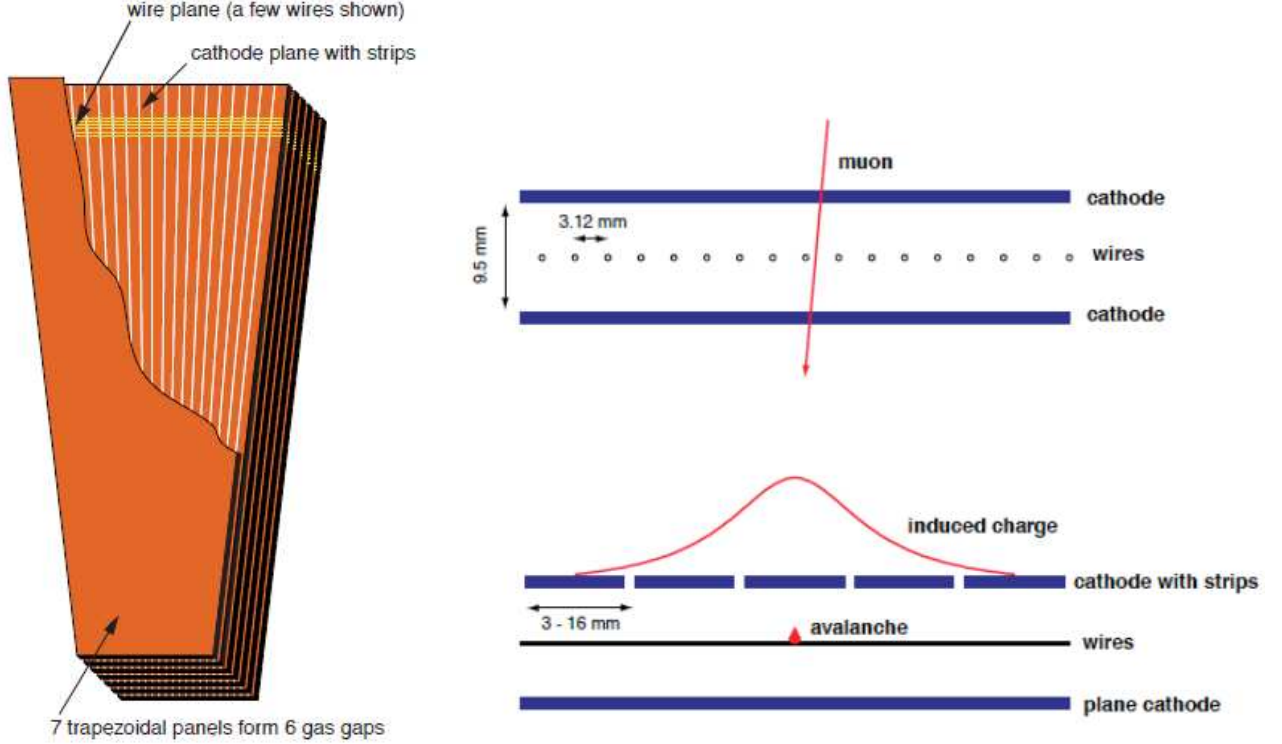


Figure 3.9: Schematic of the CSC chambers and an individual CSC cell.

The primary function of the muon systems are to allow for triggering on and identification of muons. The tracker is still the primary instrument for measuring the muons. Fig. 3.10 shows the resolution of reconstructed muons with the tracker only is only improved upon for muons with momenta above 100 GeV. For UPC  $J/\psi$  events, where muons momenta are between 1-2 GeV, the muon system does not provide any advantage in terms of improved resolution. The muon system is however important in distinguishing which tracks are due to muons as opposed to other charged particles. Because of their increase mass relative to electrons, muons emit less bremsstrahlung, or breaking radiation, as it penetrates the inner layers of the CMS on its way to

the muon systems. Fig. 3.11 shows the amount of material traversed by particles traveling through CMS as a function of  $|\eta|$ . The total of nearly 10 interaction lengths between the interaction point and the muon chambers ensures that hadrons like charged pions, which nearly exclusively decay to muons, are collected in the calorimeters before converting to muons. By eliminating backgrounds from both electrons and hadrons, the CMS muons system allows for identification of muons for both triggering and reconstruction.

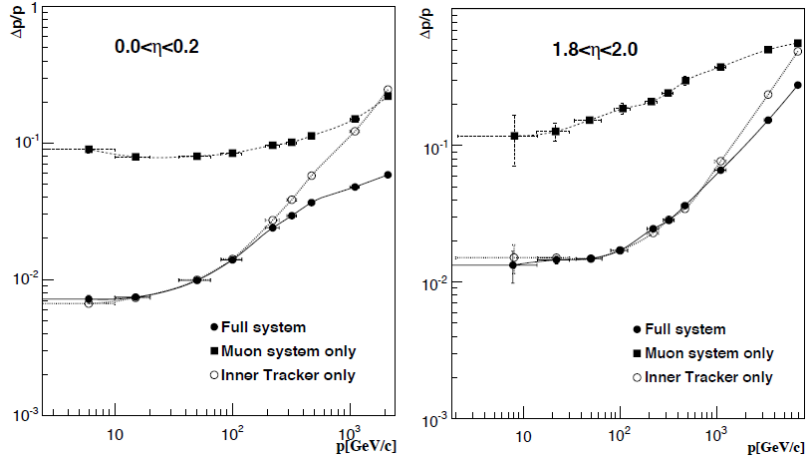


Figure 3.10: The momentum resolution of the muon system using only the tracker and the whole muon system in the barrel (left) and end cap (right).

The low-momentum nature of UPC physics creates complications due to the large amount of material between the interaction point and the muon systems. About 3 GeV of momentum is needed to reach the first layers of the muon system. In the rest frame of the  $J/\psi$ , the  $J/\psi$  equally shares its rest mass with its decay products creating 2 muons with momenta of about 1.5 GeV. For these daughter muons to reach the muon system, their parent  $J/\psi$  must be pushed to higher momentum by the initial particles which created the  $J/\psi$ . For this reason, muons from UPC  $J/\psi$ s are only detected at higher  $\eta$  values. Understanding this momentum restriction of the muon system was a major focus of the analysis discussed in this thesis with details described in Section. 6.4.

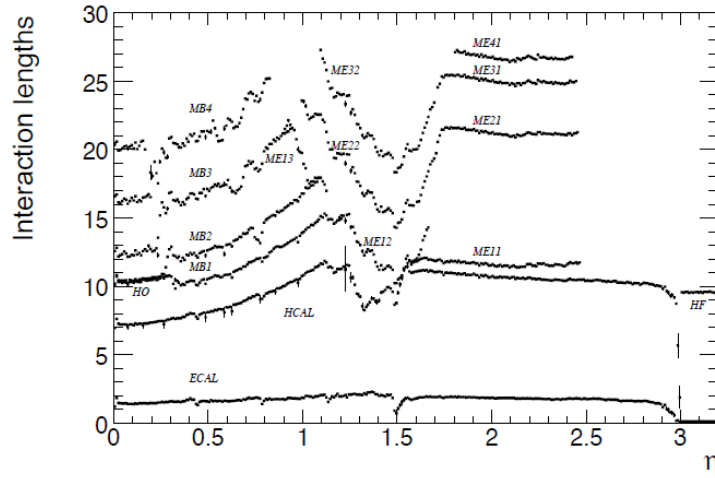


Figure 3.11: The amount of material in CMS as a function of  $\eta$  in number of interaction lengths.

### 3.6 Trigger

The CMS trigger is two tiered. The L1 trigger is the lower level hardware based system. The High Level Trigger (HLT) is a software base and runs on a computer farm located at point 5.

The purpose of the L1 trigger is to make quick decisions about which events will be kept temporarily for further processing. The L1 trigger is used to identify events where the tracker should be read out. Only the calorimeters and the muon system are used in the L1 trigger. Each of the sub-detectors has its triggering hardware. The output from the sub-detectors is synchronized to ensure that the signal from each of the sub-detectors comes from the same collision. The global trigger hardware then makes the final decision to initiate the HLT and to read out the tracker.

If an event passes the L1 trigger, the data from all the sub-detectors, including the tracker are sent to the HLT computing farm. At this level the raw data from all the sub-detectors is unpacked and combined. The information from the calorimeters, muon system, and tracker can all be used to reconstruct basic physic objects in the HLT farm. For example, tracks can be associated with either ECAL energy clusters to form electron candidates, tracks can be combined with hits in the muon system to create muon candidates. At the HLT, the whole detector is used to select events. The raw data from the events that survive the HLT are recorded permanently, those that do not are lost forever.

The HLT farm must always be ready to accept events from the L1 trigger. For this reason, the amount of computing time each HLT trigger path uses must be balanced. For more rare L1 triggers, which will occur at a lower rate, more complex reconstruction software can be used. Conversely, simpler, faster, methods must be used for more common high rate triggers. Because of this time constraint in the HLT farm, the reconstruction algorithms used for triggering tended to differ from the final reconstruction algorithms. In the HLT these algorithms are optimized for quickness, whereas the final reconstruction is optimized for precision and accuracy. By having the ability to spend different amounts of computing time on different L1 triggered events, the complexity of the event selection offered by the HLT is heightened.

The two tiered triggering system creates very low dead times while maintaining purity and selectivity. During data taking the L1 trigger is continuously monitoring, and the HLT allows for sophisticated event selection. The wide gamete of physics topics that are pursued by the CMS collaboration are a testament to the effectiveness and versatility of the CMS two tiered triggering system. In Chapter 5, the development of L1 triggers and HLT paths for selecting UPC events is discussed.

# Chapter 4

## ZDC reconstruction

### 4.1 Break up determination

As described in Section 2.4, UPC  $J/\psi$  photoproduction can be accompanied by the emission of neutrons from either of the two colliding nuclei. The various neutron emission scenarios, or break-up modes, can be distinguished by the two ZDCs. By separating events where the ZDC signal is consistent with 1 neutron versus several neutrons, or where neutrons are present on only one or both sides, the fraction of events which corresponds to a given break-up mode can be measured and compared to theory.

In order to maximize the ability to explore the one neutron peak, which sits at the bottom of the ZDCs dynamic range, a new ZDC reconstruction method was devised. This new reconstruction method was then used to establish a one neutron and many neutron threshold. This section describes the ZDC signal reconstruction and how the neutron thresholds on this signal were set.

#### 4.1.1 ZDC signal reconstruction

The signal from each ZDC is built up from the pulse shapes for each of the 18 individual ZDC channels. The pulse shape is recorded in 250 ns second chunks and is divided into 10 time slices of 25 ns (see Fig 4.1). Counting from 0, the 4th time slice is synced with the timing of the rest of

the detector and corresponds to when the products of the recorded collision reached the ZDC. The channel signal is therefore taken from the 4th time slice.

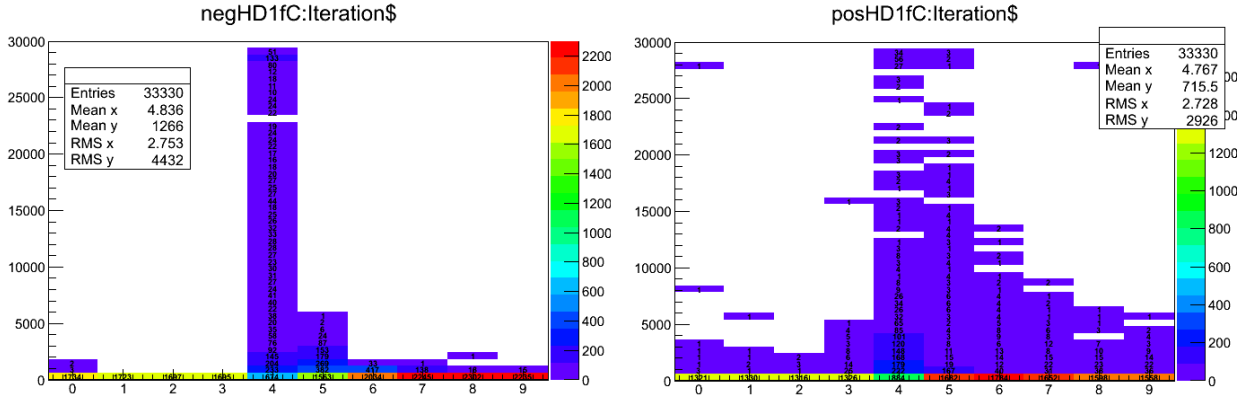


Figure 4.1: Average ZDC pluse shape is plotted as the charge as a function of time slice for the first hadronic from  $ZDC^-$  (left) and  $ZDC^+$  (right).

The ZDC signal sits on top of a low frequency noise pedestal with a period of about  $2\mu$  seconds. Over the time scale of 250 ns, this low frequency noise signal appears as a constant that shifts randomly from event to event. The contribution from this noise is therefore measured event by event in order to subtract it. Time slice 5 is used for this purpose. Time slices 1 and 2 could also be used to estimate the low frequency noise. However because the noise fluctuates to negative values of charge that cannot be measured, these time slices can only provide a measurement of the noise half the time. By using time slice 5 which contains the falling tail of the signal, the noise can be measured any time the signal raises significantly above the noise. If the fraction of signal in time slice 4 and 5 are constant and the noise contributes the same value to both time slices, the following formula is applicable:

$$Ts4 \propto (Ts4 + C) - (Ts5 + C) = Ts4 - R_{Ts5/Ts4} Ts4 = Ts4(1 - R_{Ts5/Ts4}), \quad (4.1)$$

where  $Ts4$  is the signal contribution in time slice 4,  $Ts5$  is the signal contribution to time slice 5,  $C$  is a random noise constant from the low frequency noise, and  $R_{Ts5/Ts4}$  is the ratio between the signal contribution from time slice 5 over time slice 4. Figure 4.2 demonstrates the consistency



of the fraction and validates the unconventional method of using the falling tail of the signal to estimate the low frequency noise. By using time slice 5, the chances of measuring the noise are maximized. Separating the signal from the noise is especially important because the ZDC signal for the one neutron peak sits near the noise at the bottom of the ZDC dynamic range.

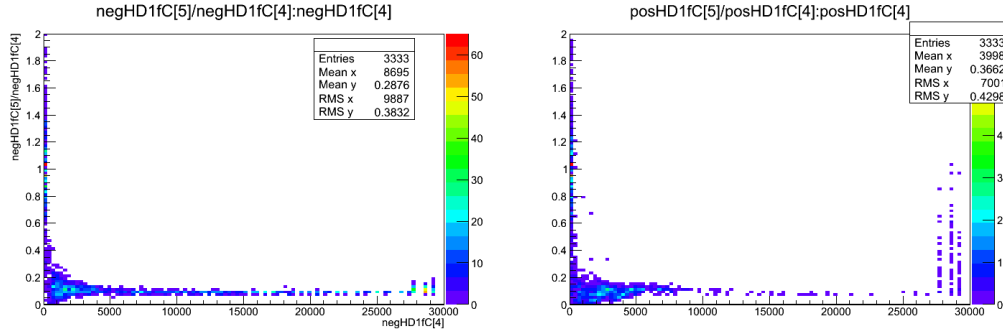


Figure 4.2: The fraction of signal in time slice 5 over time slice 4 as a function of the signal in time slice 5 in ZDC<sup>-</sup> (left) and ZDC<sup>+</sup> (right).

When summing the 9 channels in each ZDC only channels with signals above zero in time slices 4 and 5 were included. The EM, electromagnetic, section of the calorimeter is more densely packed with quartz fibers and therefore has a higher gain relative to the HAD, hadronic, section. To account for this, the EM channels were weighted with a factor of 0.1 to match the HAD channel gains.

#### 4.1.2 Determination of the one neutron thresholds

The ZDC thresholds used to establish the various break-up modes were measured from zero bias data. Figure 4.3 shows the weighted sum of the EM and HAD sections for ZDC<sup>-</sup> and ZDC<sup>+</sup> for the zero bias dataset. The neutron spectrum for this dataset is biased since the trigger only required that both beams were present in CMS. This does, however, include a significant electronic noise contribution due to events where no neutrons are emitted in the direction of the ZDC. It is clear from Fig. 4.3 that the gain of ZDC<sup>+</sup> is lower than that of ZDC<sup>-</sup>. This is because of a damaged phototube on the first HAD section of ZDC<sup>+</sup>.

To determine the thresholds for one and multiple neutrons, the ZDC<sup>+</sup> and ZDC<sup>-</sup> spectra were

fit. Four Gaussian functions were combined to fit the spectra. The electronic noise was fit to a Gaussian around zero. The one, two, and three neutron peaks are fit to Gaussians that are successively broader. The mean of each peak was initially set to multiples of the mean of the one neutron peak. The threshold for a neutron in the ZDC was taken from the fits in Fig. 4.3. Any signal greater

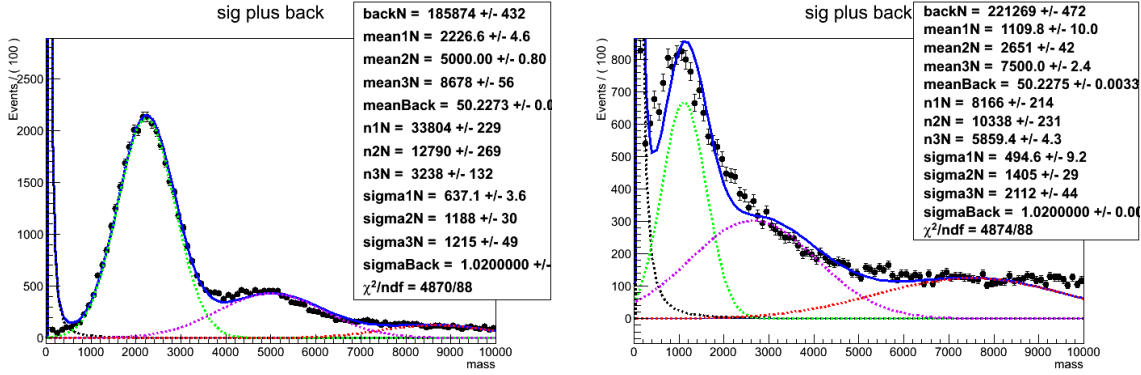


Figure 4.3: Fit to the signal spectra for ZDC<sup>-</sup> (left) and ZDC<sup>+</sup> (right)

$2\sigma$  below the mean of the one neutron peak was considered signal. Any signal greater than  $2\sigma$  above was considered multiple neutrons. The single neutron break up modes were separated from the multiple neutron modes by use of these definitions.

Several of the break-up mode calculations that have been done involve single sided configurations where neutrons are present on one side of the interaction point and not the other. These modes can be hard to identify because the single neutron peak in ZDC<sup>+</sup> overlaps with the noise peak at zero. To identify events where the ZDCs only measured noise, the noise spectrum were measured directly. Placing an additional criteria based on the ZDCs noise distributions for when the ZDCs are devoid of signal provides assurance that the events tagged as single sided events are truly single sided.

The noise distributions for the EM sections and the HAD sections were measured separately from out of time time slices. In Fig. 4.1 higher than average signal can be seen in the 0th time slice, which precedes the main signal time slice time slice 4 by 200 ns. This is due to events where activity was present in the ZDC for two consecutive collisions. Time slices 1 and 2, however, occurred between collisions. These time slices, which occur out of time, were used to measure the

noise spectrum.

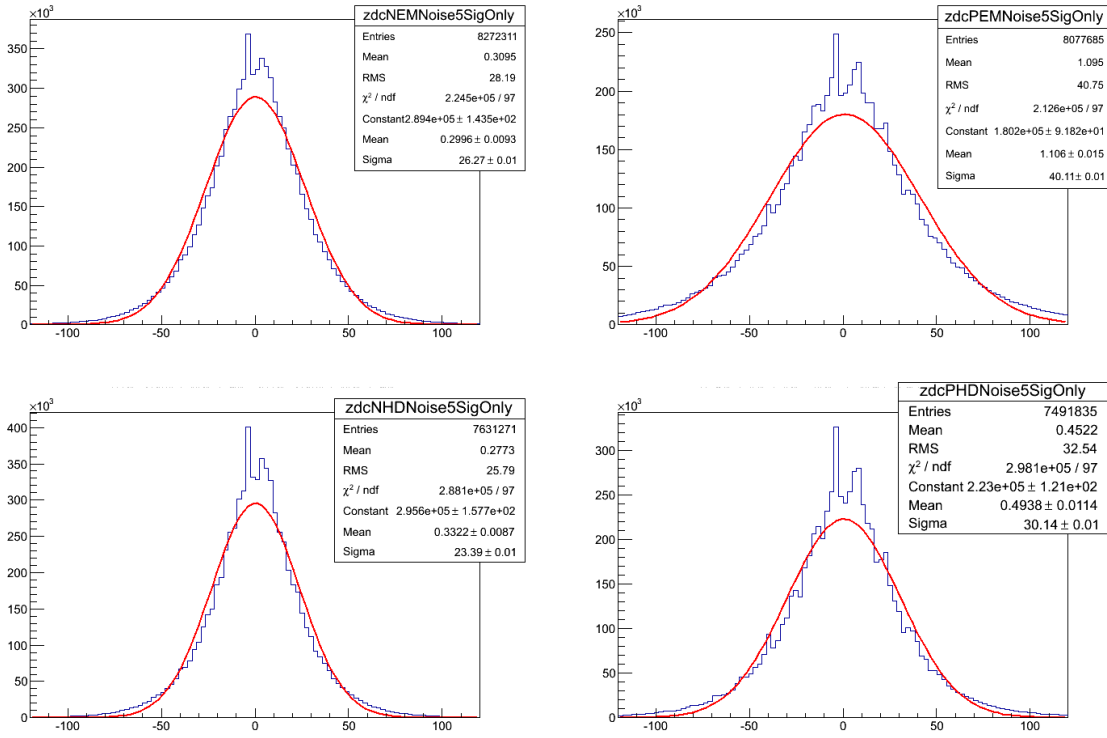


Figure 4.4: ZDC noise spectra from ZDC<sup>-</sup> EM section (upper left), ZDC<sup>+</sup> EM section (upper right), ZDC<sup>-</sup> HAD section (lower left), and ZDC<sup>+</sup> HAD section (lower right) from out of time slices.

As with the signal measurements, the low frequency noise pedestal is subtracted event by event by subtracting time slice 2 from time slice 1 leaving only the high frequency noise. The noise distributions do not depend on the amount of quartz fibers, but because the signal does, the noise distributions for EM and HAD sections are measured separately. Figure 4.4 shows the noise spectrum for each of the EM and HAD sections for the two ZDCs. If the HAD or EM signals measured from time slices which match the timing for a collision, time slices 4 and 5, are less than  $2\sigma$  above the mean of the noise distribution or lower, these sections are considered consistent with noise. A ZDC is considered consistent with noise if both the HAD section and EM section from that ZDC have signal measurements consistent with noise.

### 4.1.3 ZDC reconstruction method comparison

In this section the nominal ZDC reconstruction method designed for this thesis is compared to an alternative comparison method. This additional method, used in previous ZDC measurements, differs in the way the signal time slices are used to calculate the signal from each channel. In the additional comparison method, the signal is taken from the sum of time slices 4, 5, and 6. To estimate the event by event noise pedestal the sum of time slice 1 and 2 are used. The signal for an individual ZDC channel is then calculated as the sum of the signal time slices minus the sum of the noise time slices weighted by a factor of 3/2 to account for the differing number of noise versus signal time slices. As in the nominal method described in Section 4.1, the comparison method combines the channels to create a signal measurement from the whole of each side of the ZDC, one measurement for  $ZDC^+$ , and one for  $ZDC^-$ . The noise subtracted signal from each of the HAD channels are added together. Then the EM section channels are summed. The EM section is weighted by a factor of 0.1 as in the nominal method. After the weighting the EM and HAD channels are added to each to create one measurement for  $ZDC^+$  and another measurement for  $ZDC^-$ . Figure 4.5 shows the spectra for  $ZDC^+$  and  $ZDC^-$  using the comparison method. The same fit used for the nominal method is applied to the comparison method. As in the nominal method, the single neutron threshold is set to  $2\sigma$  below the mean from the fit to the one neutron peak. The multi-neutron threshold was set to  $2\sigma$  above the one neutron peak.

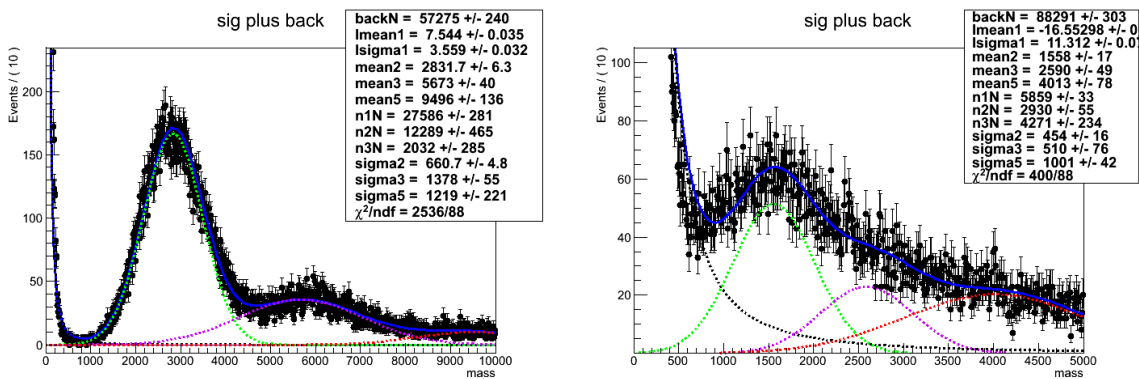


Figure 4.5: Fit to charge spectrum from  $ZDC^-$  (left) and  $ZDC^+$  (right) using the comparison reconstruction method

The advantage of the comparison method is that by using multiple signal and noise time slices the signal and noise are effectively averaged reducing time slice to time slice fluctuations. However, by using time slices 1 and 2 for measuring the noise, the noise can only be measured half the time due to unmeasurable negative fluctuations of the dominant low frequency component of the noise. The nominal method relative to the comparison method separates low signal from the noise more effectively for both sides of the ZDC. This is particularly important for  $ZDC^+$  where the 1st HAD section had a lower gain than the other sections. The  $ZDC^+$  and  $ZDC^-$  signals near the one neutron peak using the comparison and nominal reconstruction methods were plotted for comparison in Fig. 4.6. In Fig. 4.6, the shrinking of width of the noise peak around zero in the

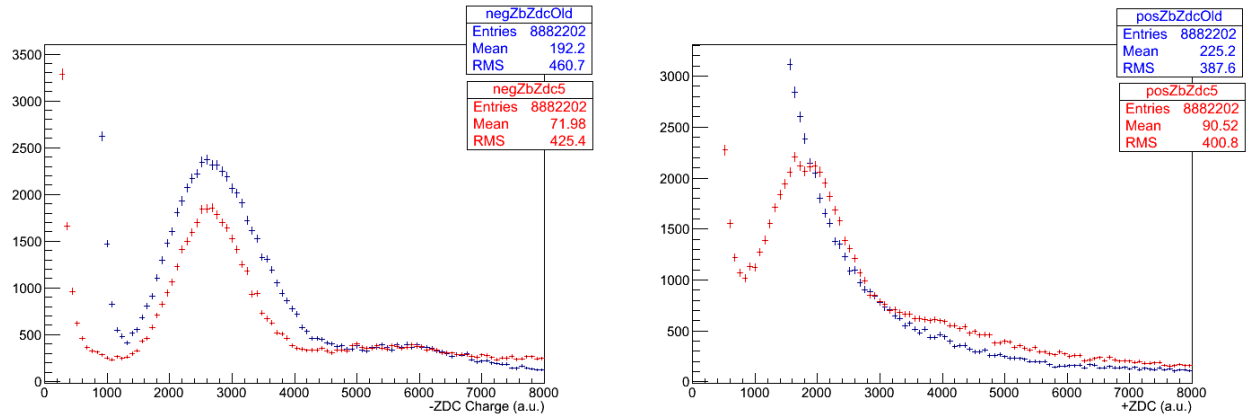


Figure 4.6: Comparison of the nominal (red) ZDC reconstruction method and the comparison (blue) method for  $ZDC^-$  (left) and  $ZDC^+$  (right).

nominal method versus the old method is apparent for both  $ZDC^+$  and  $ZDC^-$ . For the comparison method no single neutron peak is resolved in  $ZDC^+$ , whereas the single neutron peak is resolved using the nominal method.

Timing cuts were applied to enhance the signal relative to the background in order to resolve the one neutron peak in  $ZDC^+$  using the comparison method. Because the products of the collision are synced with time slice 4, noise can be rejected by selecting channels where the maximum signal falls into time slice 4. The noise will have no preferred time slice (see Fig. 4.1). Using this fact, signal can be preferably selected by requiring that the hadronic channels of the ZDC have a peak signal in the fourth time slice. Through these timing cuts the single neutron peak was recovered

using the comparison reconstruction for  $ZDC^+$ .

To examine the effectiveness of the timing cuts, event by event noise subtraction was removed from the comparison reconstruction. The signal from each channel was taken from time slices 4,5, and 6 with out subtracting 1 and 2. The signal spectrum from  $ZDC^-$  was then plotted with the result shown in Fig. 4.7. As each additional hadronic channel is required to have a maximum

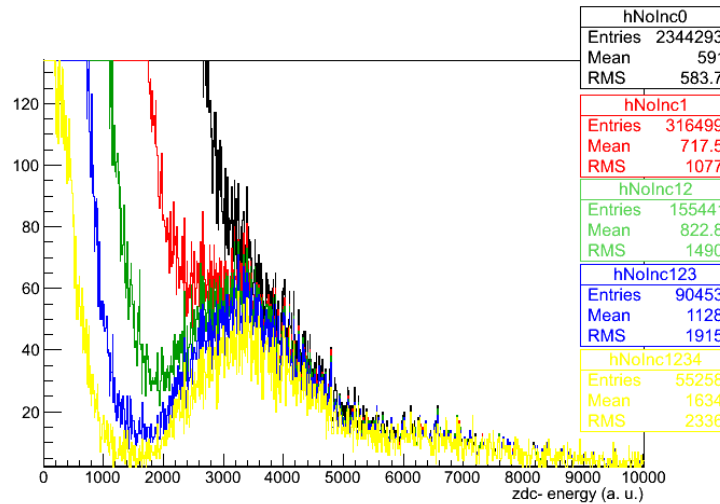


Figure 4.7: Effects of requiring in-time signal in successively more ZDC hadronic channels, no timing, at least one (red), at least two (green), at least three (blue), and all four (yellow) HAD channels have a maximum signal in the fourth time slice.

signal in the fourth time slice, the single neutron peak emerges. Figure 4.7 demonstrates that the single neutron peak can be recovered from the noise using timing cuts alone.

Using the comparison noise subtraction method, the same signal that emerges from the timing cuts alone appear without timing cuts. Figure 4.8 confirms that both noise subtraction and the timing requirement produce the same signal. This gives confidence that the signal is not an artifact of either cut, but the true neutron signal.

Figure 4.8 and Fig. 4.7 demonstrate the consistency of using timing cuts and noise subtraction to enhance the signal neutron peak. Figure 4.8 confirms the legitimacy of the timing requirement method in  $ZDC^-$  by showing that the same signal emerges from the noise subtraction method as the timing method. Fig. 4.6 demonstrates the correspondence between the nominal noise subtraction method and the comparison method in  $ZDC^-$  where signal is better separated from the electronic

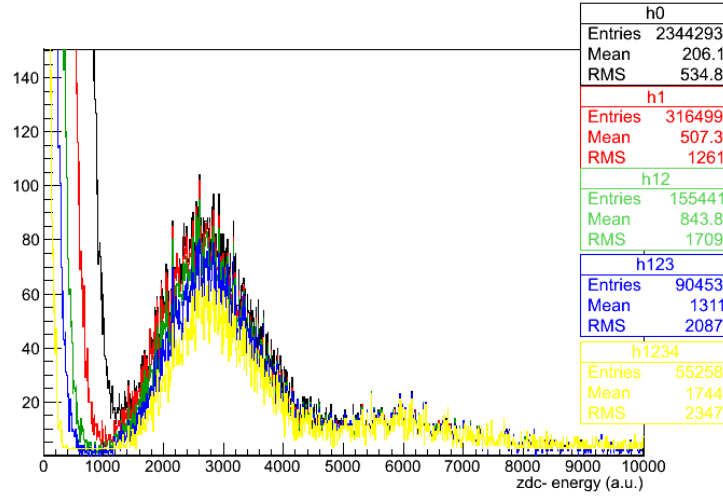


Figure 4.8: Effect of ZDC signal timing requirements after noise subtraction.

noise. This provides confidence that the signal seen in  $ZDC^+$  using the nominal method is the one neutron peak.

# Chapter 5

## UPC Trigger development for CMS

Rare physics process at the LHC require dedicated triggers in order to sort these processes from the billions of ordinary nucleus-nucleus collisions. Unlike most heavy-ion triggers, UPC triggers are optimized for low- $p_T$  and low multiplicity events. For this reason trigger development specific to UPC events was required to carry out the analysis in this thesis.

The increase in collision rate of the LHC PbPb beams from 2010 to 2011 was nearly a factor of 15. To accommodate this increase in rate, the 2011 trigger scheme needed to be more selective than in 2010 where CMS could take any event which appeared to have a collision. The available bandwidth was allocated equally amongst the various heavy ion analysis groups to pursue as wide a physics program as possible. From this consideration, bandwidth limits were placed on the trigger rates for each analysis group's trigger package.

### 5.1 L1 trigger

The UPC L1 triggers were designed to study UPC  $J/\psi$  production via the dimuon and dielectron channels (see Section 3.6). To achieve this, the loosest muon and electron triggers were combined with a trigger on energy in the ZDCs and no activity in BSCs (BSC veto). Additional triggers were commissioned in case radiation damage during the run reduced the sensitivity of the BSCs. This required no activity in HF (HF veto). These triggers are summarized in Table 5.1. The ECAL2



and ECAL5 triggers in Table 5.1 indicate a 5 and 2 GeV threshold on  $E_T$  measured in the ECAL. The MuonOpen trigger indicates that the trigger only requires a muon candidate in one of the three muon sub-systems and that there is no momentum threshold. ZDC in the trigger names indicate energy constant with at least one neutron. The sign on the ZDC label indicates which of the two ZDCs is required.

L1 trigger name	Rate (Hz)	Prescale	Id	Type
MuonOpen and (ZDC <sup>+</sup> or ZDC <sup>-</sup> ) and BSC veto	2.1	1	1	Physics
ECAL2 and (ZDC <sup>+</sup> or ZDC <sup>-</sup> ) and BSC veto	1.8	2	2	
ECAL5 and (ZDC <sup>+</sup> or ZDC <sup>-</sup> ) and BSC veto	0.3	1	3	
(ZDC <sup>+</sup> or ZDC <sup>-</sup> )	35	1500	4	Monitor
MuonOpen and (ZDC <sup>+</sup> or ZDC <sup>-</sup> ) and HF veto	0	off	5	Backup
ECAL2 and (ZDC <sup>+</sup> or ZDC <sup>-</sup> ) and HF veto	0	off	6	
ECAL5 and (ZDC <sup>+</sup> or ZDC <sup>-</sup> ) and HF veto	0	off	7	

Table 5.1: List of 2011 L1 seeds.

The cumulative L1 trigger rate for all the UPC L1 trigger seeds was required to be no greater than 200 Hz. This requirement comes from the need to keep the tracker read-out rate low. The trackers baseline voltage can fluctuate due to the high tracker hit multiplicities in PbPb collisions. In order to monitor the zero suppression of the tracker, the zero suppression algorithm was executed using the HLT computing farm rather than in the tracker firmware.

In order to record the efficiency monitoring data, the ZDC triggers were reduce to a lower rate by only keeping a fraction of the total trigger rate. The factor that the trigger rate is reduced by is called the prescale. A prescale of 2 for example means that half the triggers that were accepted. If the prescale is set to 1, then whole trigger rate is accepted. The prescales for the triggers were set to balance the competing objectives of rate reduction and increasing the overlap between the monitoring and signal triggers.

## 5.2 HLT trigger

An event must pass the selection criteria of an HLT path in order to be recorded. As opposed to the L1 trigger, which has access only to information from calorimeters and muon chambers, the HLT has access to all of the CMS sub-detectors including the tracker. Reconstruction of a track in the pixel detector is used by the UPC trigger paths. The use of the pixel detector only, as opposed to using the whole tracker including the silicon strip detector, allows for quick track reconstruction saving computing cycles. The UPC triggers were required to have at least one reconstructed pixel track in order to reject backgrounds where no particles are reconstructed by the tracker. For the muon trigger in Table 5.2 the rate was reduced by nearly a factor of 4 compared to its L1 seed rate in Table 5.1.

HLT trigger	Rate (Hz)	L1 prescale	HLT prescale	L1 seed	Type
L1UPCMuon and Pixel Track	0.52	1	1	1	Physics
L1UPCECAL2 and Pixel Track	1.65	2	1	2	
L1UPCECAL5 and Pixel Track	0.26	1	1	3	
L1ZDCOr	3.6	1500	11	4	Monitor
L1ZDCOr and Pixel Track	2.8	1500	1	4	
L1UPCMuonHFVeto and Pixel Track	0	off	off	5	Backup
L1UPCECAL2HFVeto and Pixel Track	0	off	off	6	
L1UPCECAL5HFVeto and Pixel Track	0	off	off	7	

Table 5.2: List of 2011 HLT trigger.

The total HLT output for the UPC trigger package was limited to 20 Hz. The limiting factor for the HLT rate was the amount of disk space given to this analysis. To meet the bandwidth requirements and collect a significant sample of data for estimating efficiencies, the prescales were balanced with the goal of achieving at least 5% statistical precision on the efficiency measurements. As an example of the balancing of the prescales, the HLT ZDC trigger that did not require a pixel track was given a additional prescale factor of 11 on the HLT. The ZDC path that also required a pixel track on the HLT, which used the same L1 seed, was only prescaled at the L1. The prescale of 11 was set to ensure that at least 1000 of the pixel track ZDC triggers overlapped with the ZDC L1 only triggers so that efficiency of the pixel track requirement in the trigger could be estimated

from the tracks lost.

## 5.3 Studies of 2011 PbPb data

The UPC triggers for the 2011 PbPb run make several studies possible. Three such studies are discussed below:  $\gamma\gamma \rightarrow e^+e^-$ , UPC interactions in peripheral nuclear collisions, and forward UPC  $J/\psi$  using HF.

### 5.3.1 High mass $\gamma\gamma \rightarrow e^+e^-$ in PbPb 2011

This measurement would make use of the electron triggers and combine the current di-muon data with di-electron data from the ECAL triggers. Because of the smaller mass of the electron, di-electron production is slightly favor compared to di-muon production. STARlight predicts that di-electron cross section is a factor of 2.5 higher in Xn break-up mode than for the di-muons channel when looking at masses above 4 GeV. The ECAL is position just beyond the tracker, whereas the muon system is the outermost sub-detector. This elevates the main reduction of muon acceptance, which is the material budget.

The contribution from higher order diagrams can be explored by studying photoproduction of di-lepton pairs. Because the Pb nucleus has a charge 82 times higher than the proton, the electromagnetic coupling is stronger, and therefore, higher order terms is the perturbative expansion would potentially be more important. By measuring the cross section for  $\gamma\gamma \rightarrow e^+e^-$ , the extent to which higher order terms are needed in coherent photon coupling can be constrained. Recent results by ALICE favor very small contributions for higher order terms []. In addition, this analysis provides a useful cross check to the UPC quarkonia analysis such as  $J/\psi$  by verifying the cross section normalization.

### 5.3.2 UPC hadronic overlap

In the model calculations for UPC quarkonia photoproduction all hadronic interactions are rejected. However, inclusive  $p_T$  spectra of  $J/\psi$  measured by ALICE in peripheral PbPb collisions show a low momentum peak consistent with coherent photoproduction [29]. The ALICE spectra provide

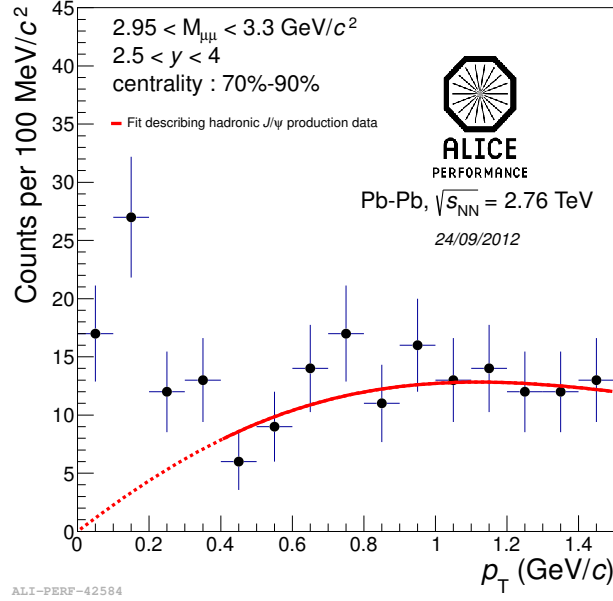


Figure 5.1: Coherent excess in inclusive  $J/\psi$   $p_T$  spectrum.

hints that UPC processes might also be present in peripheral nucleus-nucleus collisions at the LHC.

To study the overlap between photoproduction and hadronic production of quarkonia events, the inelastic sample and the UPC sample could both be used. The looseness of the rejection criteria to reject hadronic interactions, which uses the BSC detectors, leaves a significant overlap with peripheral hadronic collisions. The inclusive quarkonia sample from typical hadronic collisions can also be utilized. Coherent quarkonia photoproduction has a distinctive low  $p_T$  structure that can be used to identify photoproduced candidates in a sample that contains photoproduction combined with hadronic interactions. This measurement would open up the door to exploring the boundary between photoproduction and hadronic production.

### 5.3.3 UPC $J/\psi$ with muons in HF

As higher rapidities are explored both lower and higher momentum partons of the nucleus are probed. Because these two contributions to the UPC photoproduction cross section can be separated using neutron tagging in incoherent events, exploring higher dimuon rapidities becomes attractive. HF extends to 5 in  $\eta$ , which is 2.6 units beyond the edge of the tracker. By combining hits in HF with tracks in the tracker the higher dimuon rapidities could be explored. When combined with neutron tagging of incoherently produced quarkonia, the current study can be extended to probe lower- $x$  nuclear partons by identifying muons in HF.

## 5.4 Trigger development for the LHC pPb Run

Specific UPC triggers were also developed for the pPb run in 2013. For this period of running a much higher total trigger rate was read out relative to 2011. The total rate allocated for UPC triggers at the L1 in 2013 was 5 kHz and 50 Hz at the HLT. This factor of 5 increase in HLT and factor of 25 in L1 bandwidth, allowed for a change in emphasis from the L1 to the HLT.

The basic strategy in 2013 was the same as in 2012, use the loosest available ECAL and muon L1 triggers to push to capture the lowest  $p_T$  electrons and muons possible and reject hadronic interactions. Because of the L1 bandwidth restrictions in 2011, both the ZDCs and the BCSs were used on the L1 to reduce rates. In 2013 only the muon and ECAL triggers were used on the L1 allowing for rejection of hadronic interactions through cuts on track multiplicity. In addition, a more sophisticated trigger using full dimuon reconstructed was developed to increase purity. The main advantage in this shift in strategy was a higher purity due to the increased sophistication of the reconstruction on the HLT. In addition, an increase in cross section of the underlying physics process was achieved by relaxing the neutron emission requirement.

The HLT triggers in 2013 rejected hadronic interactions through counting tracks. For the five UPC trigger paths included in the HLT menu, three levels of reconstruction were done at the HLT.

- Pixel tracks were reconstructed from the inner pixel section of the silicon tracker alone,

tracks were reconstructed using the full tracker using the strips as well, and full dimuon reconstruction was done using the tracker and muon detector.

- The least restrictive pixel track paths required at least one track reconstructed from the pixel detector and less than 10 pixel tracks in the event.
- Full tracking paths were added on top of the pixel track paths and included an additional requirement of one full track and less than 7 reconstructed tracks.
- The most restrictive path added to the pixel and full tracking paths and required reconstruction of dimuons with a mass between 2 and 12 GeV.

### 5.4.1 pPb $J/\psi$

The CMS UPC triggers commissioned for the 2013 LHC pPb will allow for the study of  $J/\psi$  photoproduction. This process is dominated  $\gamma - p$  interactions [1]. The measurement would primarily probe the proton gluon densities. In Eq. 2.13 the photon flux depends on the square of the number of protons in parent nucleus,  $Z^2$ . However, the cross section of the target only increase as the total number of nucleons to  $A^{2/3}$ . The much higher photon flux from the Pb-ion compensates for the decreased size of the proton.

A pPb UPC  $J/\psi$  measurement will complement the measurements done at HERA [2], and measurements done by ALICE [3]. CMS will contribute by adding additional kinematic coverage and cover a unique range of  $\gamma p$  center of mass energies,  $W_{\gamma p}$ . The difference in beam energies and species at LHC versus HERA result in access to different  $W_{\gamma p}$ . ALICE and CMS have different acceptance in  $J/\psi$  rapidity, which also translates to coverage of different  $W_{\gamma p}$ . In addition, an excess in the UPC cross section compared to HERA measurements would indicate a non-exclusive contribution to the pPb UPC  $J/\psi$  cross section. This measurement will both help enhance the current understanding of the  $\gamma p$   $J/\psi$  photoproduction cross section as a function of  $W_{\gamma p}$ .

# Chapter 6

## Analysis

In this chapter the various parts of the analysis are explained. In Section 6.1, the simulations used to estimate the detector's ability to measure UPC processes are discussed. The selection of UPC events is detailed in Section 6.2. Extraction of the number of coherent  $J/\psi$  candidates is explained in Section 6.3. The determination of the detector's efficiency for measuring UPC events is explained in Section 6.4. Finally, Section 7 lays out the systematic uncertainties for the measurement.

### 6.1 Physics generators and Monte Carlo simulations

Every physical measurement is the product of the underlying physics folded with the response of the detector used to do the measurement. In order to understand the underlying physical process, the detector's effect on the measurement must be understood and accounted for. As instruments become more and more complicated, the interplay among all of the many parts of the detector makes an analytic approach to the problem untenable. For this reason, the numerical technique of Monte Carlo (MC) simulation is often the most effective approach for describing detector effects.

MC simulations use random number generation to model the many statistical effects of particles interacting with different parts of the detector. First, particles are generated according to theoretical distributions. These particles are then propagated through a simulation of the detector. As the

particles pass through the detector, random numbers are used to determine how these particles interact with the materials of the detector based on the known properties of the material. In this way, the theoretical distributions are convolved with a realistic model of the detector's response. A more detailed picture of how the detector shapes the underlying distributions emerges with each successive event. The final goal of the MC simulation is to produce a set of events that accurately reproduce what would be measured if the theoretical input describes nature well.

### 6.1.1 MC vs Data compairson

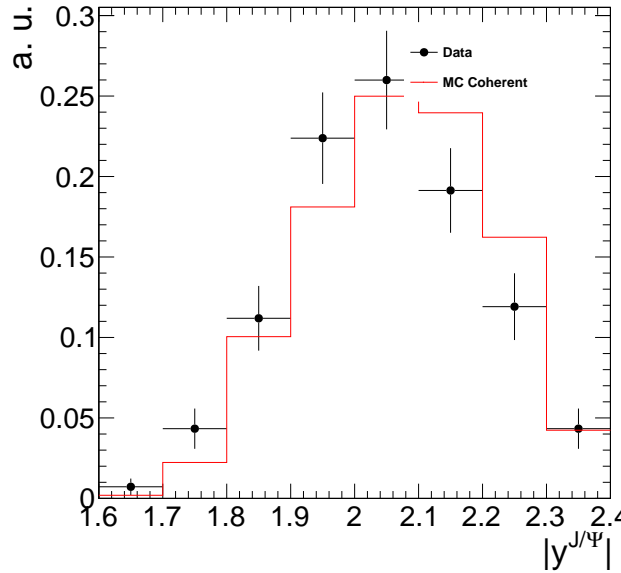


Figure 6.1: Comparison of the of the dimuon rapidity distributions between coherent  $J/\psi$  MC sample and data.

### 6.1.2 STARlight and particle gun MC in CMS

In this thesis, two classes of generator input samples were used, STARlight [?, 30] and a particle gun. The STARlight samples correspond to the theoretical calculations described in Section 2.2, while the particle gun produces particles with a user defined transverse momentum distribution and rapidity distribution and isotropic decay to muon pairs in the  $J/\psi$  rest frame. For STARlight, three different physical process were simulated: coherent  $J/\psi$  production, where the photon couples to



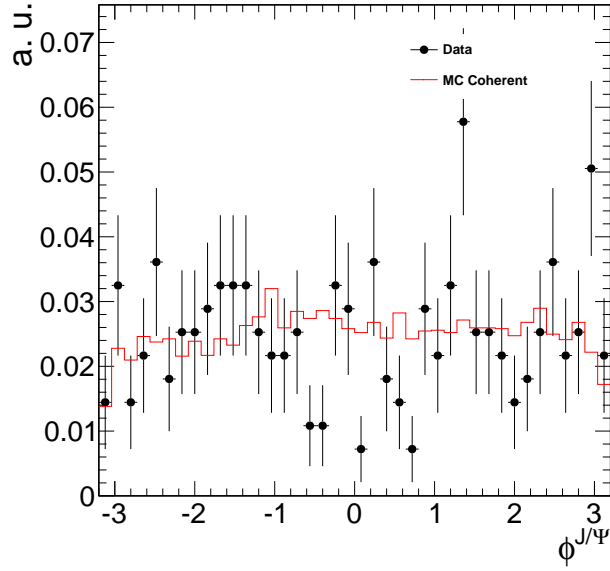


Figure 6.2: Comparison of the of the dimuon  $\phi$  distributions between coherent  $J/\psi$  MC sample and data.

the nucleus as a whole; incoherent  $J/\psi$  production; where the photon couples to a single nucleon within the nucleus, and photon-photon interactions, where the photons from the two nuclei interact with each other to produce a pair of oppositely charge muons. All three STARlight samples contain a  $\mu^+$  and  $\mu^-$  in the final state.

Because STARlight is not integrated into the standard CMS software framework (CMSSW) [?], a simulation software chain with 5 steps was developed. First, STARlight is run in the specified mode, and a single file is created for each physics process. In step 2, the STARlight output file is converted to the Les Houches (LHE) format [31], and the momentum of the parent  $J/\psi$  or the initial photon-photon pair is added to the record of each event. The event record produced by STARlight only contains the final state particles. To process the events in parallel, the STARlight files are subdivided in step 2, creating several LHE files from a single STARlight file. The LHE files are used as input to CMSSW.

Steps 3 to 5 take place within CMSSW. In step three the generated particles are propagated through the GEANT4 [32] detector simulation. This accounts for all the interactions with the detector and produces as output a format identical to the raw data that is recorded during data

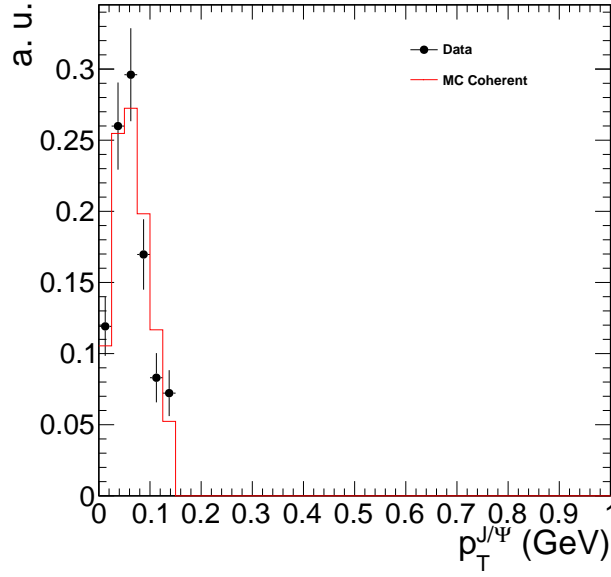


Figure 6.3: Comparison of the of the dimuon  $p_T$  distributions between coherent  $J/\psi$  MC sample and data.

taking. Steps 4 and 5 are processed using the same software as in data taking. In step 4 the reconstruction software used during data taking is run on the output of the detector simulation. The output of the reconstruction is reduced to the information that is needed for the final analysis in the final step.

The particle gun samples were created entirely within CMSSW.  $J/\psi$  mesons were created according to user defined  $p_T$  and rapidity distributions. The decay of  $J/\psi$ s to a  $\mu^+\mu^-$  pair was simulated with a uniform decay distribution, corresponding to unpolarized  $J/\psi$  particles. As with the STARlight samples, these muons are propagated through the GEANT4 simulation [32] of the detector, and the raw data is produced. The remaining steps of running the reconstruction code and reducing the data to the final data format needed for the analysis are identical to the STARlight production.

The momentum of the final state muons is the main driver of whether the candidate can be measured. One of the two daughter muons must have large enough momentum to fire the trigger, and both muons must have enough momentum to be reconstructed and tagged as a muon. There are at least 10 interaction lengths of material through which the muons must travel in order reach

the muon chambers (see Fig. 3.11). This imposes an effective momentum threshold of about 7 GeV in order for muons can fire the trigger.

The  $p_T$  distribution and the polarization of the  $J/\psi$ s produced are the main factors controlling the momentum of the muon daughters, which vary for the different MC samples. The polarization effects how the momentum is shared between the daughters [33]. In the rest frame of the parent  $J/\psi$ , equal momentum is given to each daughter muon. However in the lab frame of the detector, the muon daughters which are emitted from transversely polarized  $J/\psi$  will tend to be emitted in the direction the  $J/\psi$  is traveling and will have unequal momentum in the lab frame. The daughter traveling in the direction of the  $J/\psi$  will have increased momentum, whereas the daughter traveling opposite to the  $J/\psi$  direction will have decreased momentum.

In Fig. 6.4 the  $J/\psi$ s  $p_T$  from the STARlight generated coherent, and incoherent, and the dimuon  $p_T$  for photon-photon samples are compared. Both the coherent and the photon-photon samples are concentrated a low  $p_T$ , and neither sample extends much beyond 0.15 GeV. The incoherent sample is peaked near 0.5 GeV and extends beyond 1 GeV. The two particle gun samples resemble the incoherent and coherent samples  $p_T$  distributions. The first sample has a Gaussian  $p_T$  distribution extending to approximately 0.15 GeV, whereas the second is flat in  $p_T$  up to 2 GeV.

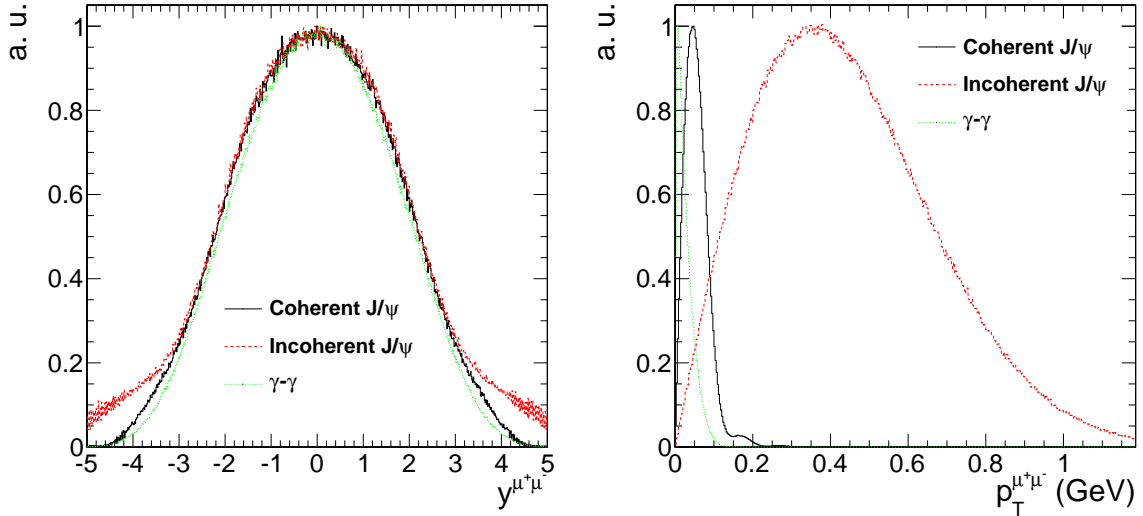


Figure 6.4: Generator level rapidity (left) and  $p_T$  (right) distributions for the coherent (black), incoherent (red), and photon-photon process (green).

The particle gun samples are unpolarized, whereas the STARlight samples have transverse polarization. In Fig. 6.5, the cosine of the helicity angle of the particle gun samples and the STARlight samples are shown. For the STARlight sample the helicity angle, the angle between the direction of the  $\mu^+$  daughter and the  $J/\psi$  direction in the rest frame of the  $J/\psi$ , prefer to be either parallel or anti-parallel. However, the particle gun samples have no preferred direction of emission.

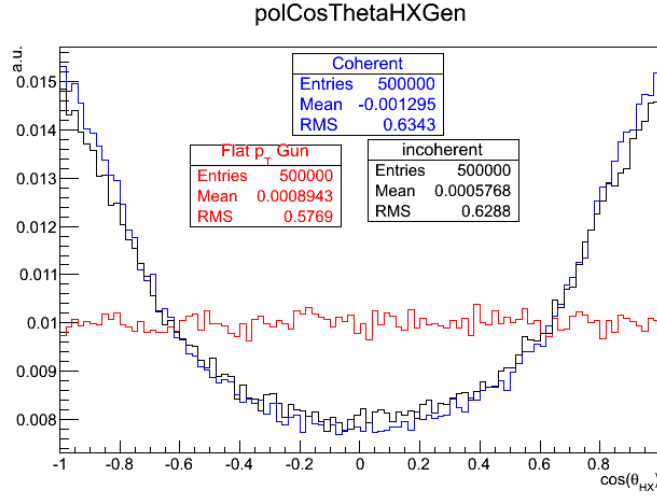


Figure 6.5: The  $J/\psi$  polarization of the particle gun (red), coherent (blue), and incoherent samples are plotted as the cosine of the helicity angle.

## 6.2 Event selection

The unprecedented amounts of data produced by the LHC has made it possible to investigate novel physics processes like UPC  $J/\psi$  production. The data for this analysis were recorded during the 2011 LHC PbPb run. During this period,  $150 \mu b^{-1}$  were recorded by the CMS detector, corresponding to over a billion PbPb collisions. Of this,  $143 \mu b^{-1}$  of data were used in this analysis due to the ZDCs being temporally disconnected to test the Forward Shower Counters.

### 6.2.1 Data sets

The data were divided into three specially selected samples, Physics, Monitoring, and Zero bias, based on the triggers which recorded the events (see Table 6.1). By recording this hierarchy of samples, interesting events are selected with a much higher purity in the physics sample, while the zero bias and ZDC triggered samples allow for the investigation of the selection criteria. The purity, which is a measure of how many signal events relative to background events are in a sample, is obtained by using more selective triggers. Less selective triggers, those assigned to the monitoring and zero bias samples, were used to investigate to what extent signal events are lost due to the higher selectivity of physics triggers. These samples were recorded using subsets of the HLT triggers found in Table 5.2 of Chapter 5. The  $J/\psi$  events discussed in this thesis were obtained analyzing the sample labeled in Table 6.1 as physics. A ZDC triggered monitoring sample was recorded for the sake of estimating efficiencies. Lastly, a zero bias sample was recorded for investigating the ZDC and the noise distributions of HF.

The physics sample containing the  $J/\psi$  signal was recorded by the muon trigger labeled "L1UPCMuon and Pixel Track" in Table 5.2. Because of the characteristically low momentum of UPC  $J/\psi$  as compared to  $J/\psi$  created by other physics processes, the loosest muon trigger was used. The noise trigger rate for the muon trigger alone was 50 Hz, but in coincidence with the BCS veto and the ZDC trigger the noise rate was below 2 Hz. By pairing the muon trigger with the ZDC on the L1, the noise contribution was reduced from the noise contribution from either of the two sub-detectors to the noise coincidence between the two sub-detectors. Contributions from hadronic interactions are reduced by the veto on the BSCs. This trigger was designed to balance reducing the rate with maximizing the efficiency, allowing for the data to be recorded without producing high rates that would have resulted in dead time for the detector.

In order to investigate the muon trigger and the other parts of the event selection, a monitoring sample was recorded by requiring energy consistent with at least one neutron in either of the ZDCs. Neutron production is a much more common process than the UPC  $J/\psi$  production. This process has cross sections on the order of 100 b compared to 10 mb predicted for  $J/\psi$  production. For this

Sample	Events	$\mathcal{L}_{int}$
Physics	346K	$143.3 \mu b^{-1}$
Monitor	1.1M	$31.6 mb^{-1}$
Zero Bias	8.8M	$580 b^{-1}$

Table 6.1: Integrated luminosities and number of events for the three samples used in this analysis.

reason, the rates of this trigger are much higher than the physics trigger, and only a small sub set of these events are recorded. From this trigger the pixel track portion of the HLT trigger efficiency was estimated as well as the ZDC trigger efficiency, as will be described in Section 6.4.

In addition to the monitoring and physics sample, a zero bias sample was recorded to examine the ZDC neutron reconstruction and the HF noise distributions. The zero bias trigger fired every time both beams passed through CMS. Only 4 events out of every million triggered were recorded for this sample. This sample allowed for an unbiased measurement of the ZDC neutron threshold energies as discussed in Section 4.1. Because the zero bias trigger only requires the presents of both LHC beams, the sample contains very few hadronic collisions. This allowed for a measurement of the electronic noise distribution in the HF, which are important to reducing contamination from hadronic interactions.

The integrated luminosity for each of the three samples is calculated by recording activity in HF [34]. The cross section for HF activity is measured from a van der Meer scan. In this way, the amount of integrated luminosity for any running period is related to the activity in HF.

### 6.2.2 Event selection cuts

The analysis described in this thesis focuses on UPC  $J/\psi$ s decaying to muons. The trigger used for this analysis recored 346841 events. A set of off-line cuts were applied to increase the relative contribution of UPC events to background processes. Two sets of event selection cuts were applied to reject background events. The first set rejects background from the beam. The second rejects events where hadronic collisions have occurred. Table 6.2 summarizes all the event selection cuts.

Cut type	Cut	Events
–	all triggered	346841
beam background rejection	good vertex requirement	340997
	beam halo muon rejection	302777
	cluster shape compatibility requirement	233590
hadronic interaction rejection	single-sided neutron requirement	149992
	two track requirement	32732
	HF signal rejection	5392
fake muon rejection	muon quality requirement	2047
kinematic cut	$J/\psi$ mass requirement	696
	muon detectability cuts	567

Table 6.2: Effects of event selection cuts.

To reject beam induced background the following cuts were applied:

- The reconstructed vertex must be within 2 cm in the transverse direction and 25 cm in the longitudinal direction. This cut ensures that reconstructed particles come from interactions between the two beams rather than event where one of the two beams interact with gas particles near the interaction point.
- Beam halo muons were rejected using the timing of the muon hits. The beam halo cut rejects events where muons surrounding the beam stream through the detector.
- Pixel cluster shape should be compatible with the vertex. This cut requires that energy deposits in the silicon tracker point back to the reconstructed primary vertex.

These beam background cuts do not reject any UPC  $J/\psi$  candidates.

The second set of background rejection cuts were designed to reduce contamination from hadronic interactions.

- No more than 2 reconstructed tracks in the event. The track requirement rejects events that produce many charged particles.
- Maximum reconstructed hit energy in HF was required to be below the threshold for electronic noise. Nearly all hadronic interactions (about 98%) produce particles in the range

$3 < |\eta| < 5$  covered by the HF detector. By requiring that the energy deposits in HF resemble noise, nearly all elastic hadronic collisions are expected to be rejected.

- Energy in the ZDCs consistent with neutrons on only one side of the interaction point. In hadronic interactions both nuclei break-up. By requiring that ZDC only reconstruct neutrons on one side of the interaction point, hadronic interactions that produce neutrons on both sides were rejected.

Each of these cuts were designed to reject topologies produced by hadronic interactions. The effect of these cuts can be seen in Table 6.2 and are denoted hadronic interaction rejection.

To establish the HF noise thresholds, the noise distributions were measured in zero bias events. An offline selection of events with no reconstructed tracks was used to ensure that no collision had taken place. The HF noise threshold was defined as the cut that keeps 99% of the zero bias events. The noise distribution from this zero bias sample is compared to the physics sample and MC in Fig. 6.6.

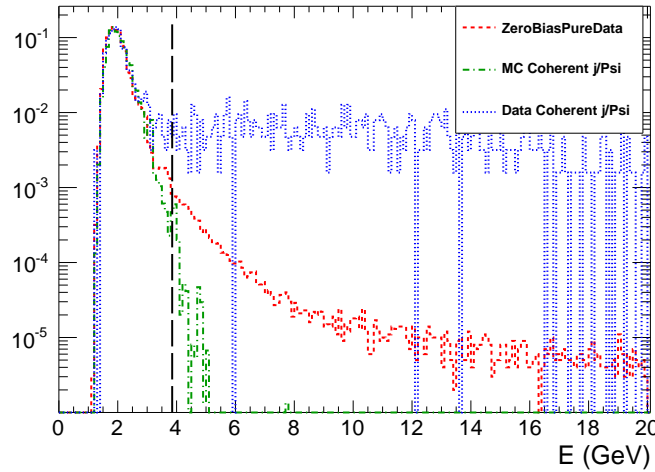


Figure 6.6: Comparison of HF noise distributions in zero bias data, physics triggered data, and MC.

The following standard muon quality cuts are applied:

- Tracker track matched with at least one muon segment (in any station) in both X and Y coordinates ( $< 3 \sigma$ ).



- Cut on number of tracker layers with hits  $> 5$ .
- Number of pixel layers  $> 0$ .
- The  $\chi^2$  per degrees of freedom of the track fit  $< 3$ .
- Loose transverse and longitudinal impact parameter cuts, within 3 cm in the transverse direction and within 30 cm in the longitudinal direction with respect to the primary vertex.

These cuts are applied to reduce the number of fake muons and have been validated for other muon analyses [35].

## 6.3 Signal extraction

After all event selection cuts, the remaining events contain a combination of coherent  $J/\psi$ , incoherent  $J/\psi$ , and dimuons from the photon-photon process. Each process must be separated from the final mix. To achieve this, the invariant mass and  $p_T$  distributions are used to distinguish between the three processes. The photon-photon process is extended in invariant mass whereas the  $J/\psi$  is peak strongly near 3.1 GeV. In dimuon transverse momentum distribution of the photon-photon and coherent process have similar distributions, both peaked sharply below 0.1 GeV, whereas the incoherent process is more broadly distributed across an interval extending to nearly 1 GeV. The mass distribution was fit to separate the photon-photon process from the  $J/\psi$  process. The  $p_T$  distribution was used to separate the incoherent process from the photon-photon process, and the coherent process. In this way, a separate yield was extracted for all three processes.

The invariant mass distribution for opposite sign dimuons is shown in Fig. 6.7. A  $J/\psi$  signal is clearly visible together with tails at higher and lower mass due to the photon-photon process. A fit to the invariant mass distribution was performed using a Gaussian to account for the  $J/\psi$  signal and a first-order polynomial function for the photon-photon process. The extracted number of  $J/\psi$  candidates from this fit includes all  $J/\psi$ s in the mass window that passed the analysis cuts, i.e.

both coherent and incoherent process contribute to yield from the mass fit. The  $p_T$  distribution is needed to separate the two different contributions to the  $J/\psi$  peak.

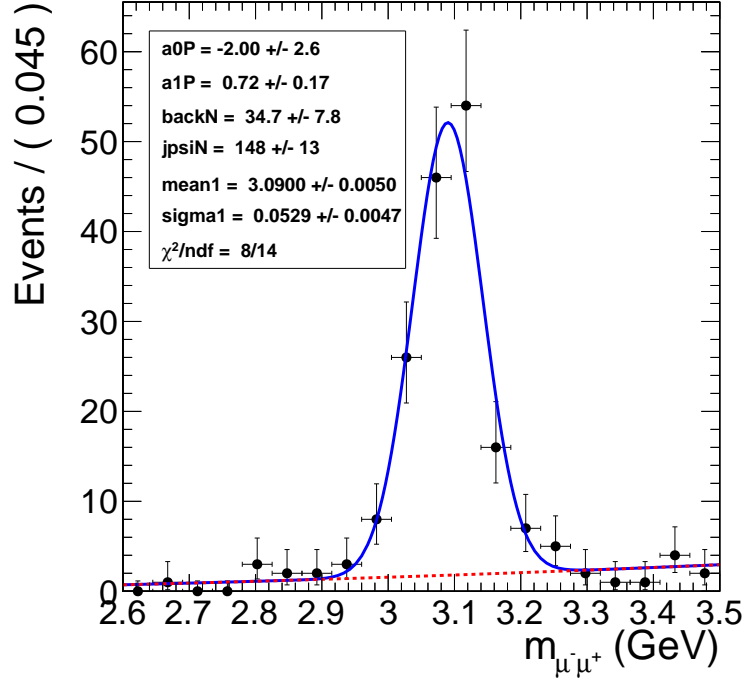


Figure 6.7: Mass fit to  $J/\psi$  using Gaussian for the signal and a first-order polynomial for the photon-photon continuum.

Figure 6.8 shows the  $p_T$  spectrum of the events plotted in Fig. 6.7. There is a clear coherent peak at  $p_T = 60$  MeV followed by broad distribution that peaks near  $p_T = 450$  MeV. To extract the contribution of coherent, incoherent and gamma-gamma processes in the data the spectrum in Fig. 6.8 was fit to the sum of three MC templates corresponding to the final output of the MC simulations for these three processes. The clear overlap of the coherent and photon-photon process, and the clear separation of these two lower  $p_T$  processes from the incoherent process is apparent. The shape of the  $p_T$  distribution for the coherent, incoherent, and photon-photon process are taken from the final output of MC after applying all analysis cuts. In Fig.6.8, the yield parameters that were fit were left unconstrained for all three process.

The shape of the photon-photon and coherent  $J/\psi$  process are very similar in transverse momentum. Accordingly, the contribution from the photon-photon process and the coherent process are

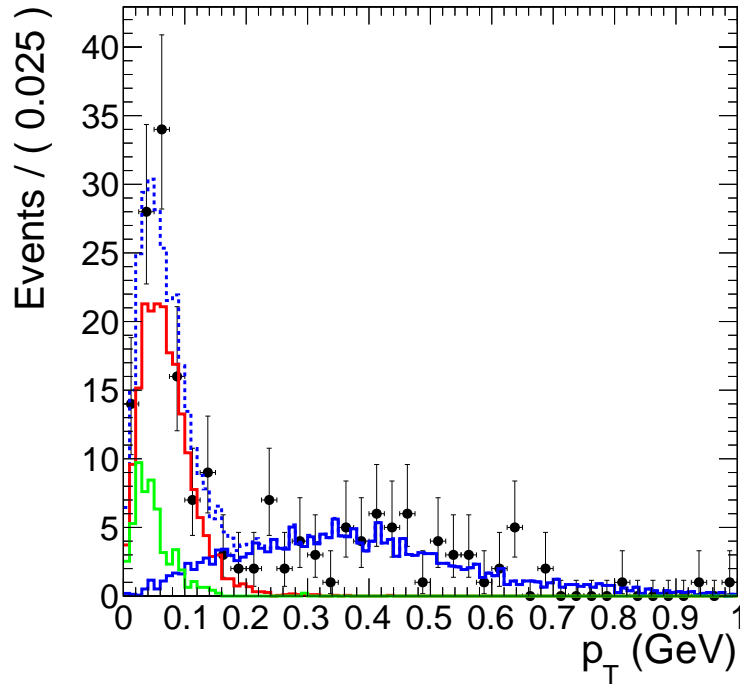


Figure 6.8: Fit to MC  $p_T$  templates.

difficult to separate from the  $p_T$  distribution. The confidence contours in Fig. 6.9 from the template fit in Fig. 6.8 demonstrate the strong anti-correlation between the coherent yield parameter,  $nCo$ , and the yield parameter for the photon-photon process,  $nGamma$ . Because of the anti-correlation, the statistical uncertainty on  $nCo$  and  $nGamma$  from the fit are larger than  $\sqrt{nCo}$  and  $\sqrt{nGamma}$  expected from Poisson statistics. The information from the invariant mass and  $p_T$  distributions were combined to break this correlation. Through this combination, the contribution to the final yield from the three process was measured.

A simultaneous fit to the mass spectrum and  $p_T$  spectrum was performed to utilize the mass fits ability to distinguish the photon-photon process from the coherent and incoherent process all while utilizing the  $p_T$  fits ability to separate the coherent and photon-photon processes from the incoherent. Fig. 6.10 shows the result of the simultaneous fit. The simultaneous fit forces the parameter  $nGamma$  to both describe the photon-photon continuum present in the side bands of the  $J/\psi$  mass peak as well the photon-photon contribution to the low- $p_T$  part of the  $p_T$  spectrum. In addition, the  $J/\psi$  yield from the mass fit is forced to equal the contribution from the incoherent

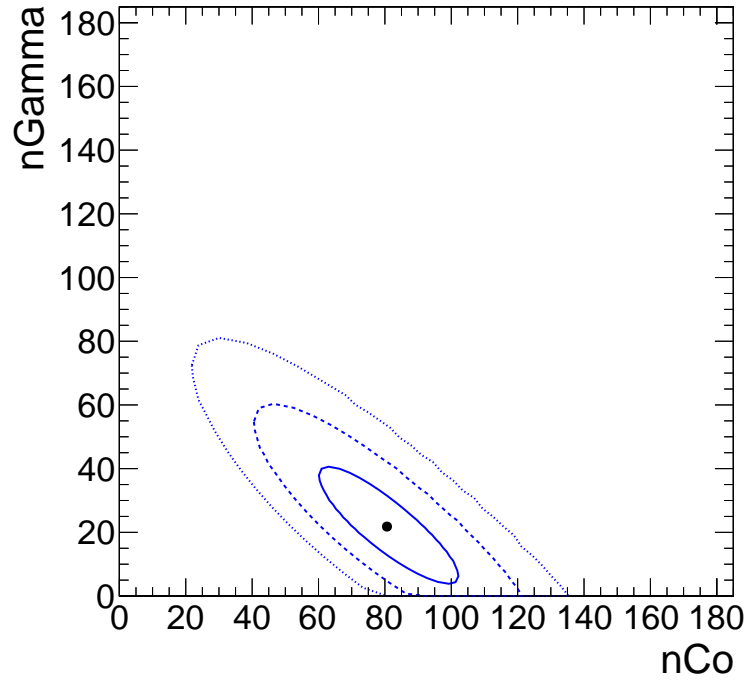


Figure 6.9: 68%, 95%, and 99% confidence contours from the  $p_T$  template fit.

and coherent process in the fit to the  $p_T$  distribution. In this way, the correlation between the yield parameters was broken, and the contribution from the three process were made independent of each other.

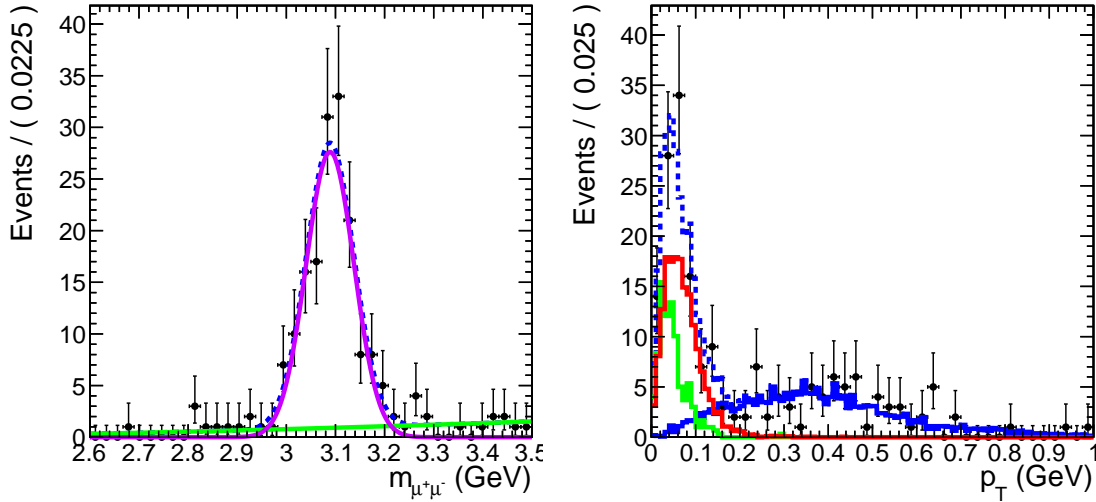


Figure 6.10: Simultaneous fit to the mass and  $p_T$  spectra.

Fig. 6.11 shows the confidence contours for  $nCo$  and  $nGamma$  from the simultaneous fit in

Fig. 6.10. The slope of the confidence contours in Fig. 6.11 is noticeably than in Fig. 6.9. The contours for the simultaneous fit are also reduced compared to Fig. 6.9 with widths in  $nCo$  and  $nGamma$  similar to those expected from Poisson statistics. From the simultaneous fit, reasonable statistical errors were obtained along with the yields for the three processes.

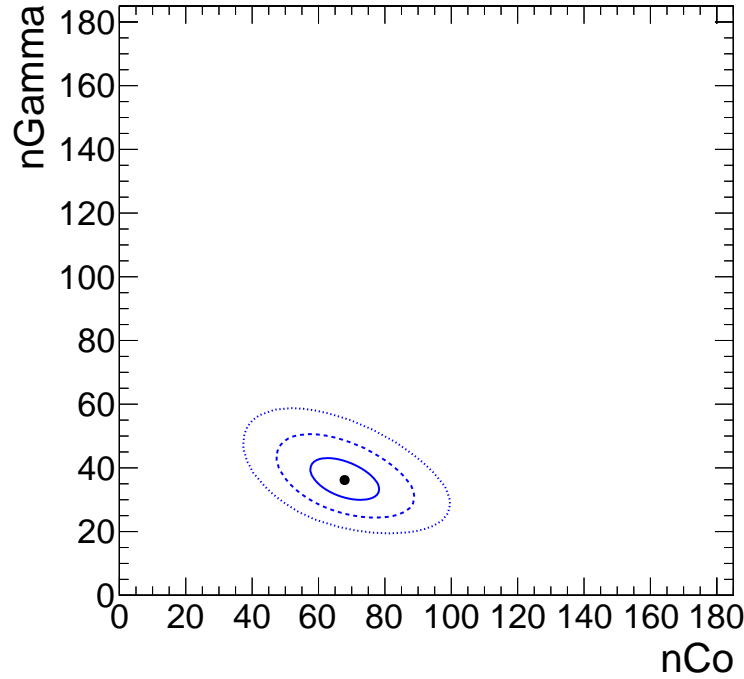


Figure 6.11: 68%, 95%, and 99% confidence contours from the simultaneous fit.

## 6.4 Efficiency determination

Each step of the triggering, event selection, and analysis has an associated efficiency that must be accounted for in the measurement of the  $J/\psi$  cross section. The ZDC trigger efficiency, the muon trigger efficiency, and the muon reconstruction efficiency are the two most significant contributors to the total efficiency measurement. The efficiency of the pixel track requirement, and the veto on activity in the BSCs from the trigger are also estimated but found to be consistent with fully efficient. The following section explains how each of these efficiencies were measured with a special emphasis on the ZDC trigger efficiency and the muon trigger and reconstruction efficiencies.

### 6.4.1 Muon efficiencies

The muon efficiencies were measured using a combination of MC and data based methods. The MC based measurement accounts for the detector acceptance and the efficiency of the muon quality cuts discussed in Section 6.2. The trigger efficiencies were measured in data using the tag and probe method [36], which is discussed below.

CMS has a limited acceptance for  $J/\psi$ s, particularly in the case of  $J/\psi$ s with low momentum like those produced in UPC events. To measure the acceptance of CMS for  $J/\psi$ s, reconstructed dimuon candidates were considered detectable if both reconstructed muon daughters fell into a detectability region in  $p_T$  and  $\eta$ . The muon detectability region was defined using the coherent  $J/\psi$  events obtained from STARlight. The efficiency for reconstructing single muons  $\epsilon_{reco}^\mu$  is defined by  $\epsilon_{reco}^\mu = \frac{N_{reco}^\mu}{N_{gen}^\mu}$ , where  $N_{reco}^\mu$  is the number reconstructed muons obtained after the full CMS detector simulation and that passed the standard muon quality cuts, and  $N_{gen}^\mu$  is the number of generated muons from STARlight. Fig. 6.12 shows the efficiency for reconstructing single muons from co-

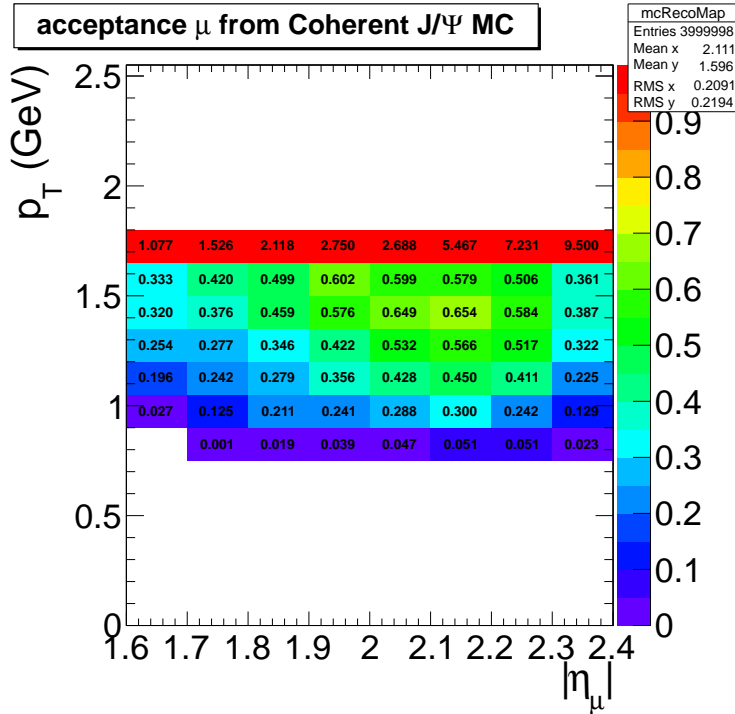


Figure 6.12: Muon daughter detectability from coherent  $J/\psi$

herent  $J/\psi$  events. To avoid the edges of the detectors acceptance, all reconstructed muons that fall

into a  $(p_T, |\eta|)$  bin that has an efficiency less than 20% were rejected. This condition defines the detectability region. The acceptance for reconstructing dimuons was calculated from MC using the following formula:

$$A = \frac{N_{det}(|y|, p_T)}{N_{gen}(|y|, p_T)}, \quad (6.1)$$

where  $N_{det}$  is the number of reconstructed dimuons where both daughters fall into the detectability region, and  $N_{gen}$  is the number of generated dimuons. From Eq. 6.1, the acceptance for  $J/\psi$  was calculated as a function of  $|y|$ , and  $p_T$  (see Fig. 6.13).

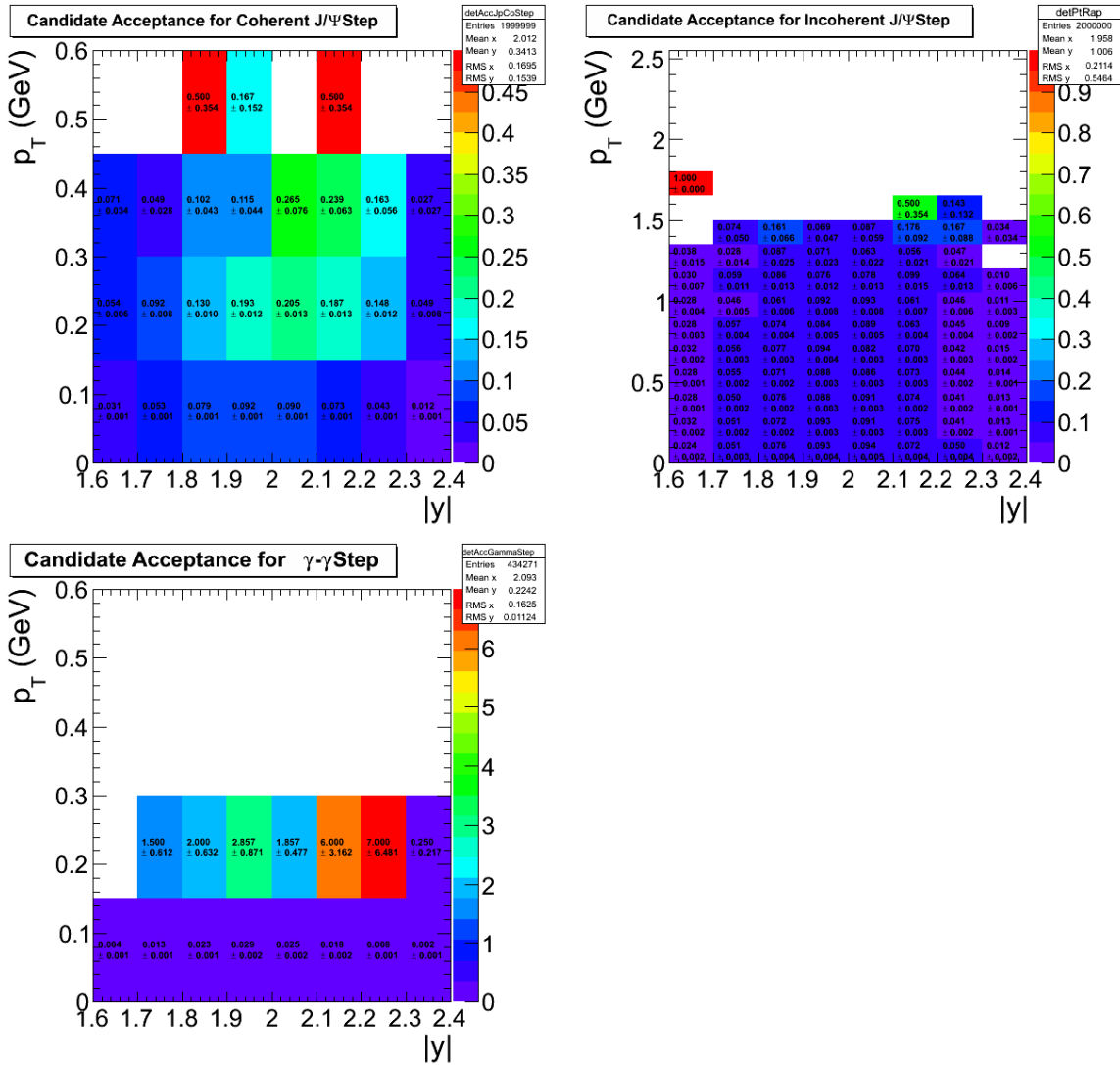


Figure 6.13: Dimuon acceptance from coherent  $J/\psi$  (top left), incoherent  $J/\psi$  (top right), and photon-photon interactions (lower).

The "tag and probe method" is a data driven approach used to measure the trigger efficiency of the muon daughters from  $J/\psi$  decays. In this method there are three categories of daughter muons. *Tag muons* are high quality muons. *Passing probes* are reconstructed muons that match the muon trigger, while *failing probes* do not. Each dimuon will have one daughter classified as a tag and the other as a probe. From here three invariant mass histograms are studied. One histogram is created from all pairs. The second comes from pairs where the probe is a passing probe. The last histogram comes from pairs where the probe fails to fulfill the trigger, it is a failing probe. By matching the tag to the trigger, the probe is unbiased by the trigger and the efficiency can be measured by fitting the three mass histograms.

Because the trigger efficiency depends on the  $p_T$  and  $|\eta|$  of the muon, one set of three histograms for each  $(p_T, |\eta|)$  bin of the probe is created. To extract the single muon trigger efficiency  $\epsilon_{trig}^\mu$ , each set of invariant mass histograms were simultaneously fit. The signal was fit using a Crystal Ball function, and the background was fit to an exponential. The Crystal Ball parameters were simultaneously fit to all three histograms. The exponential function was fit to the failing and passing probe histograms separately. Because the background shapes are in principle different for the two samples, the efficiency is driven by this difference.

Fig. 6.14 shows the fit of the three sets of pairs. This fit was done for each bin of the probes  $p_T$

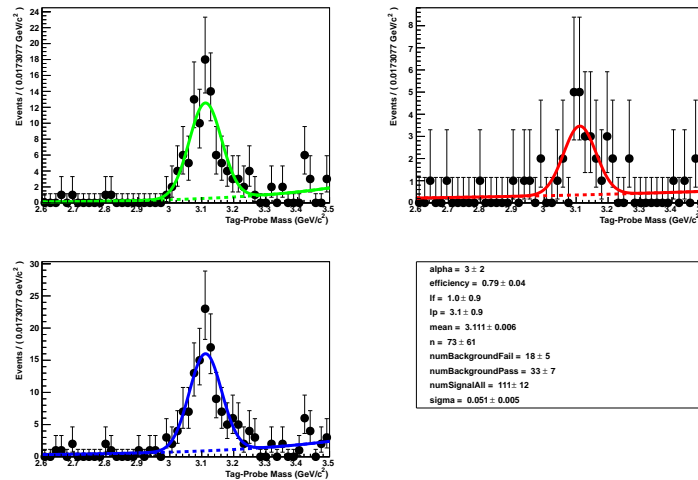


Figure 6.14: Fits to tag and probe pairs in the  $J/\psi$  mass region for pairs with a probe  $2 < |\eta| < 2.2$  and  $1.55 < p_T < 1.8$  GeV.



and  $\eta$ . The efficiency from the fits in each bin are shown in Fig. 6.15.

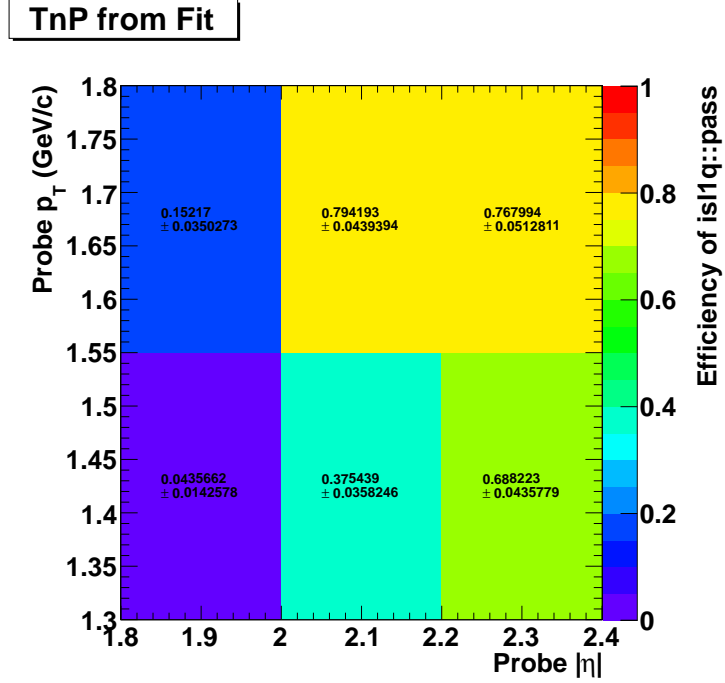


Figure 6.15: Muon trigger efficiencies in  $p_T$  and  $\eta$  bins from the tag and probe method.

The dimuon trigger efficiency  $\epsilon_{trigger}^{dimuon}$  was calculated from the single muon efficiencies using the following equation:

$$\epsilon_{trigger}^{dimuon} = 1 - (1 - \epsilon_{trigger}^{\mu_1})(1 - \epsilon_{trigger}^{\mu_2}), \quad (6.2)$$

where  $\epsilon_{trigger}^{\mu_1}$  is the tag and probe efficiency of the first dimuon daughter, and  $\epsilon_{trigger}^{\mu_2}$  is the efficiency of the second muon daughter. In Eq. 6.2 the probability of at least one daughter firing the trigger is calculated by subtracting one from the probability that neither daughter fires the trigger, thus giving the dimuon trigger efficiency.

The average dimuon trigger efficiency for each dimuon ( $p_T, |y|$ ) bin was calculated by averaging the efficiency of dimuon candidates in each bin. The dimuon trigger efficiency ranges from about 50% to 90%. As expected the  $J/\psi$  trigger efficiency increase with rapidity since the longitudinal momentum of the  $J/\psi$  is given  $p_Z = M_{J/\psi} \cdot \sinh(y)$ . Thus  $J/\psi$  mesons at forward rapidity distribute more momentum to their daughter muons which therefore have a greater chance of punching through into the muon chamber. The average trigger efficiency was multiplied by the

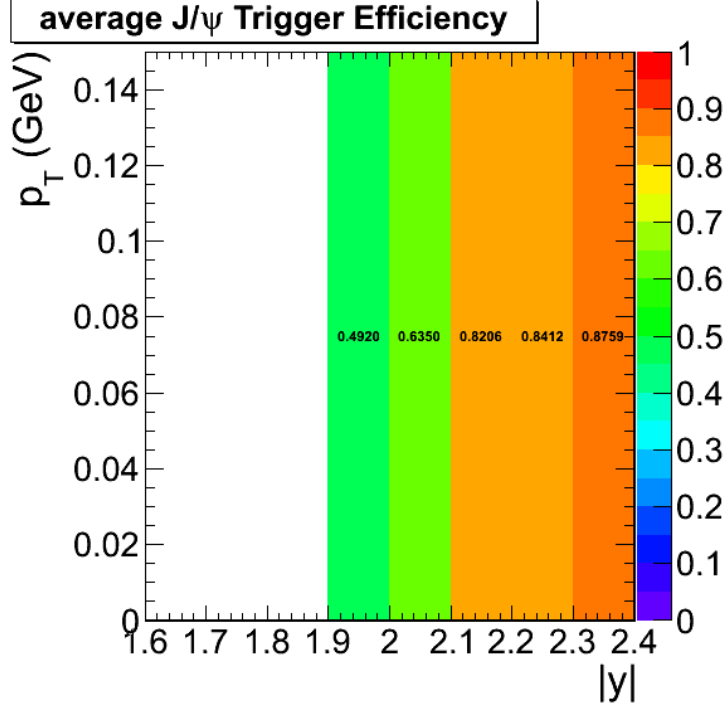


Figure 6.16: The trigger efficiency from tag and probe averaged over candidates in each  $(p_T, |y|)$  bin.

acceptance and reconstruction efficiency from the MC to produce a total factor for both efficiency and acceptance.

The total combined efficiency and acceptance factor coherent  $J/\psi$  between  $2.0 \leq |y| \leq 2.2$  was found to be  $\approx 5\%$ . The acceptance factor of roughly 7% from the MC was found to be the main contributor to the total efficiency. The interplay of the polarization of the  $J/\psi$  and the material in detector drive down the efficiency by creating an effective momentum threshold for detection (see Section 6.1). The reconstruction efficiency of the daughters range between 20%-60% for muons in the defined detectability range. The trigger efficiency for the detectable muons ranges from 30%-80% depending on  $p_T$ .

#### 6.4.2 ZDC trigger efficiency

As discussed in Section 4.1, the trigger labeled "L1ZDCOr and Pixel Track" in Table 5.2 was used to measure the ZDC trigger efficiency. This trigger required either a  $ZDC^+$  or  $ZDC^-$  trigger,

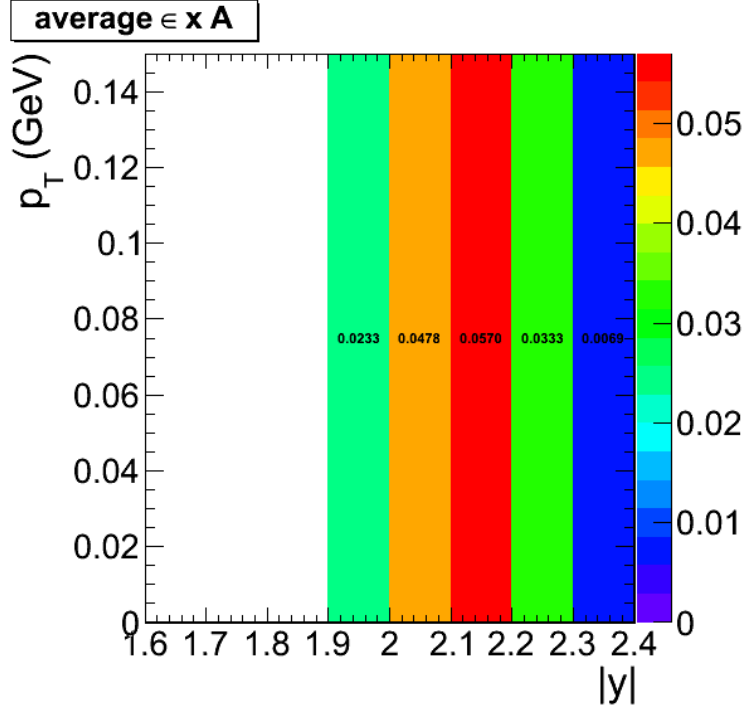


Figure 6.17: The acceptance times averaged trigger efficiency from tag and probe.

together with at least one pixel track. The veto on the BSC minimum bias trigger, as in the physics triggers, was applied offline. The BSC veto excludes events where BSCs from both sides of the interaction point are above threshold. This trigger was used in order to collect the most inclusive possible sample without using the minimum bias triggers designed to collect hadronic interactions.

This ZDC triggered sample suffers from a trigger bias. For example, a sample triggered by  $ZDC^+$  would always produce a  $ZDC^+$  trigger efficiency of one. To avoid this, a similar technique to tag and probe was used. Each event is either tagged as triggered by  $ZDC^+$  or triggered by the  $ZDC^-$ . The  $ZDC^+$  trigger efficiency is measured from the  $ZDC^-$  tagged sample, and vice versa.

To estimate the efficiency, the number of events with energy in  $ZDC^+$  greater than the single neutron threshold,  $N_{events}$ , was measured. From this set of events, the number of events that also fire the  $ZDC^+$ ,  $N_{trig}$ , was measured. The ratio between the number of single neutron events that fired the trigger and all single neutron events was taken as the estimate of trigger efficiency. The same procedure was applied for each side of the ZDC. The trigger efficiency was found to be 98% for  $ZDC^-$  and 94% for  $ZDC^+$ .

ZDC Side	$N_{events}$	$N_{trig}$	$\epsilon_{ZDC}$
ZDC <sup>+</sup>	73028	71706	$0.9819 \pm 0.005$
ZDC <sup>-</sup>	76132	71859	$0.9439 \pm 0.005$

Table 6.3: ZDC trigger efficiencies for ZDC reconstruction method 1 and 2

# Chapter 7

## Systematic uncertainties

Table 7.1 shows the systematic errors that were estimated. The method used to separate the coherent from the photon-photon process is the most dominant error. The ZDC reconstruction method used to estimate the neutron thresholds is the next most dominant, followed by the method used to estimate the HF noise threshold.

systematic	uncertainty in %
Template fit normalization	+9.5% -12.0%
ZDC trigger efficiency	3.5%
ZDC reconstruction	2.9%
HF noise threshold	+1.3% -3.4%
MC acceptance	1.1%
Total systematic	+10% -13%

Table 7.1: Summary of systematic uncertainties

### 7.1 Template fit normalization

The  $p_T$  template fit depends on the functions chosen for fitting the mass distribution. As described in Section 6.3, the similarity of the  $p_T$  distribution for the coherent and photon-photon process makes the contributions from the two process difficult to separate from the  $p_T$  distribution alone. The mass distribution was used to distinguish between these two processes.

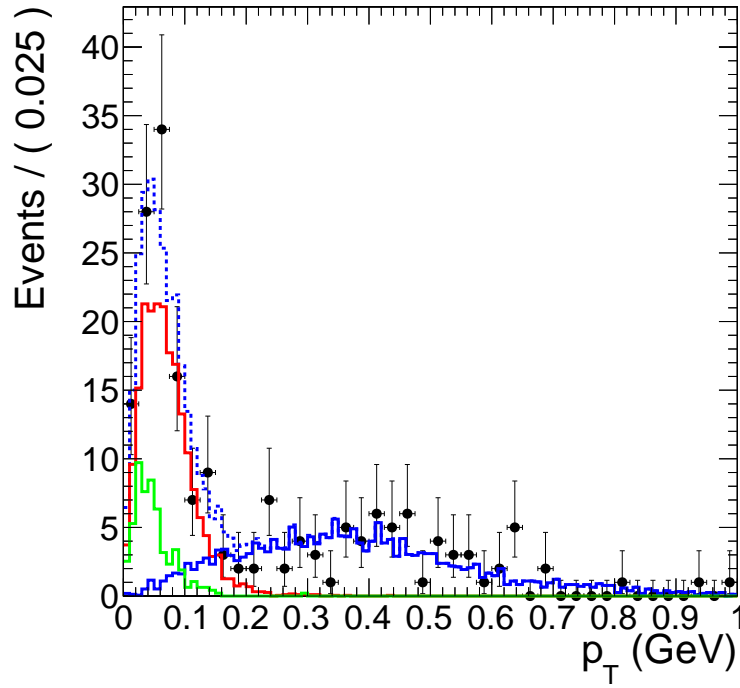


Figure 7.1: Coherent, incoherent, and photon-photon process  $p_T$  template fit to data.

The systematic uncertainty due to the choose of functions used to fit the mass distribution was estimated by varying the signal and background functions. The contribution to the background from the mass fit was used to fix the contribution from the photon-photon process in the  $p_T$  template fit. Two functions were used to describe the signal, a Gaussian, and a Crystal ball function. The background was fit to a linear function, a 2nd order polynomial, and a 2nd order Cheby-Chev polynomial. The resulting variation on the coherent contribution was used to as an estimate of this systematic effect.

Moving from left to right in Fig 7.2, the contribution from the photon-photon process increases. The  $\chi^2$  / degree of freedom is similar between the three fits indicating a similar goodness of fit. On this basis, neither fit is preferred. The left most fit uses a Crystal Ball function to account for the radiative decay of the final state daughters of the  $J/\psi$ . The low mass exponential portion however picks up background events and overestimates the  $J/\psi$  contribution. The right most plot fits the background to a 2nd order Cheby-Chev polynomial. Because the Cheby-Chev peaks just below the  $J/\psi$  peak, this fit overestimates the background and in turn underestimates the signal

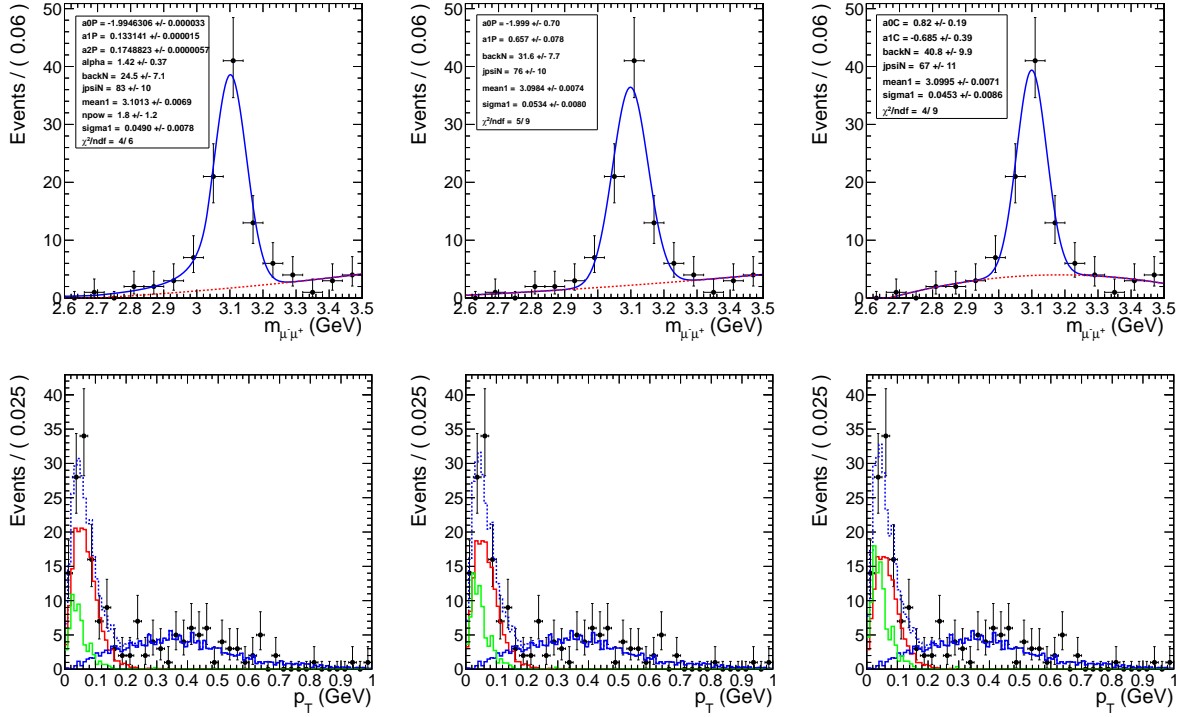


Figure 7.2: Various mass distribution fits and the corresponding  $p_T$  template fit.

contribution. The Gaussian fit with a linear background however does a reasonable job of fitting both the background and the signal.

From these three fits an upper and lower bound of the systematics due the choice of fit functions was estimated. The difference between the Gaussian-Linear fit and the Crystal Ball-polynomial fit was taken as an upper bound. The difference between the Gaussian-Linear fit and the Gaussian-Cheby-Chev fit was taken as a lower bound. The overall systematic uncertainty due to the choose of normalization for the photon-photon template is found to be  $+9.5\%$   $-12\%$ .

## 7.2 ZDC trigger efficiency

The ZDC trigger efficiency measurement is sensitive to the underlying neutron distribution. The more neutrons that hit the ZDC, the higher the trigger efficiency will be. To estimate the effect the input sample has on the efficiency, the ZDC trigger efficiency was measured from five different samples. Table 7.2 shows the results from the three samples, which require a reconstructed pixel

ZDC Side	Reco Method	$N_{events}$	$N_{trig}$	$\epsilon_{ZDC}$
(ZDC <sup>+</sup> or ZDC <sup>-</sup> ) and 1 pixel track				
ZDC <sup>-</sup>	comparison	72946	71688	$0.982 \pm 0.005$
ZDC <sup>-</sup>	nominal	73028	71706	$0.982 \pm 0.005$
ZDC <sup>+</sup>	comparison	76137	71786	$0.943 \pm 0.005$
ZDC <sup>+</sup>	nominal	76132	71859	$0.944 \pm 0.005$
(ZDC <sup>-</sup> or ZDC <sup>+</sup> ), 1 pixel track, and L1 EG trigger				
ZDC <sup>-</sup>	comparison	613758	602123	$0.9810 \pm 0.0018$
ZDC <sup>-</sup>	nominal	614014	601863	$0.9802 \pm 0.0018$
ZDC <sup>+</sup>	comparison	643905	602671	$0.9360 \pm 0.0017$
ZDC <sup>+</sup>	nominal	647888	603089	$0.9309 \pm 0.0017$
(ZDC <sup>-</sup> or ZDC <sup>+</sup> ), 1 pixel track, and L1 Muon trigger				
ZDC <sup>-</sup>	comparison	65466	63376	$0.968 \pm 0.005$
ZDC <sup>-</sup>	nominal	65543	63358	$0.967 \pm 0.005$
ZDC <sup>+</sup>	comparison	71929	63512	$0.883 \pm 0.005$
ZDC <sup>+</sup>	nominal	72932	63582	$0.872 \pm 0.005$

Table 7.2: ZDC trigger efficiencies using the nominal and comparison ZDC reconstructions for trigger sample that require a pixel track.

track in the event to reduce noise. Both the nominal and comparison ZDC reconstruction methods are shown.

The systematic uncertainty in the ZDC trigger efficiency due to the uncertainty in the underlying distribution was estimated by calculating the standard deviation of efficiency measurements in Table 7.2. The uncertainty in the ZDC trigger for ZDC<sup>-</sup> was found to be less than 1% and taken to be negligible. For ZDC<sup>+</sup>, the systematic uncertainty was taken to be 3.5%.

### 7.3 ZDC reconstruction

In order to estimated the systematic uncertainty in the ZDC reconstruction method, the comparison ZDC reconstruction method described in Section 4.1.3 is used to measure the number of candidates in the Xn0n mode. The systematic uncertainty due to the ZDC reconstruction method is estimated from the difference between the UPC J/ $\psi$  candidate yields when using the comparison versus the nominal method. The yields for the nominal and comparison ZDC reconstruction method in the Xn0n break up were found to be 298 and 315 respectively. Half the difference between the two



methods was used as an estimate of the systematic uncertainty, giving 2.9%.

## 7.4 HF noise threshold

The way in which the HF noise distribution is measured effects the event selection and therefore the final candidate yield. This cut plays a significant role in rejecting hadronic events. In Table 6.2 the importance of cutting on HF noise is evident. The HF noise cut rejects nearly 1/5 of the remaining events. The systematic uncertainties on the HF noise requirement is important for this reason.

The most basic information from the HF detectors are contained in RecHits. There is one RecHit per phototube on HF. The RecHit signal is calibrated in GeV, and no noise subtraction is done. The CaloTowers are formed from geometrical groups of RecHits. They are the first stage of the CMS jet trigger and perform some noise suppression.

The default HF noise cut required that the maximum RecHit energy from both HF+ and HF- be less than 3.85 GeV. This cut was designed to accept 99% of the noise events, see Fig. 6.6. The stability of this cut was tested by

1. Summing CaloTowers instead of RecHits
2. Making separate cuts on HF- and HF+
3. Tightening the threshold so that only 98% or 97% noise events passed the cut.

Object type	HF (GeV)	HF <sup>-</sup> (GeV)	HF <sup>+</sup> (GeV)
RecHits	3.85	3.25	3.45
CaloTowers	4.25	3.25	3.75

Table 7.3: Thresholds from combined HF noise distributions and two-side noise distributions.

Table 7.3 shows the noise thresholds for RecHits and CaloTowers for both the combined HF+ and HF- calorimeters and the two-sided individual calorimeters when 99% of noise events are accepted. Table 7.4 compares the threshold for the cases when 99%, 98% and 97% of noise events are accepted. The number of  $J/\psi$  events remaining after these cuts is shown in Table 7.5. The

%	$E_{RecHit}$ (GeV)	$E_{CaloTower}$ (GeV)
99	3.85	4.25
98	3.25	3.75
97	2.95	3.25

Table 7.4: HF noise thresholds for keeping various fractions of the noise sample for RecHit and CaloTower.

efficiency corrected numbers are also shown in order to compare between different noise thresholds. The fractional systematic error is then estimated by finding the maximum and minimum deviation from the default method. The nominal number of candidates come from the 99% combined RecHit threshold. From Table 7.5, the maximum number of corrected candidates comes from the 99% threshold for combined CaloTower objects, and the minimum from 97% threshold for the same objects. The fractional increase from the maximum of 305 corrected candidates and the nominal value of 301 is taken as the systematic upper bound; the bound is estimated from the minimum of 289, giving a systematic uncertainty of  $^{+0.3\%}_{-3.4\%}$ .

%	RecHit cut	RecHit corrected	CaloTower cut	CaloTower corrected	Threshold type
99	298	301	302	305	Combined
98	287	293	294	300	
97	284	292	280	289	
99	290	293	288	291	Two-sided

Table 7.5: Number of upc dimuon candidates with  $p_T < 1$  GeV when changing HF calorimeter cuts for RecHit and CaloTower.

## 7.5 MC acceptance

The MC derived acceptance correction factors depend on the input physics generator. The underlying  $p_T$  distribution was assumed to be correctly described by STARlight for the coherent cross section measurement. To estimate the effect of changing the underlying  $p_T$  distribution on the acceptance measured from the MC, the incoherent sample was used to correct the coherent yield. Half the difference was used as the estimate and was found to be 1.1%.

## 7.6 Additional systematic checks

### 7.6.1 Mass fit

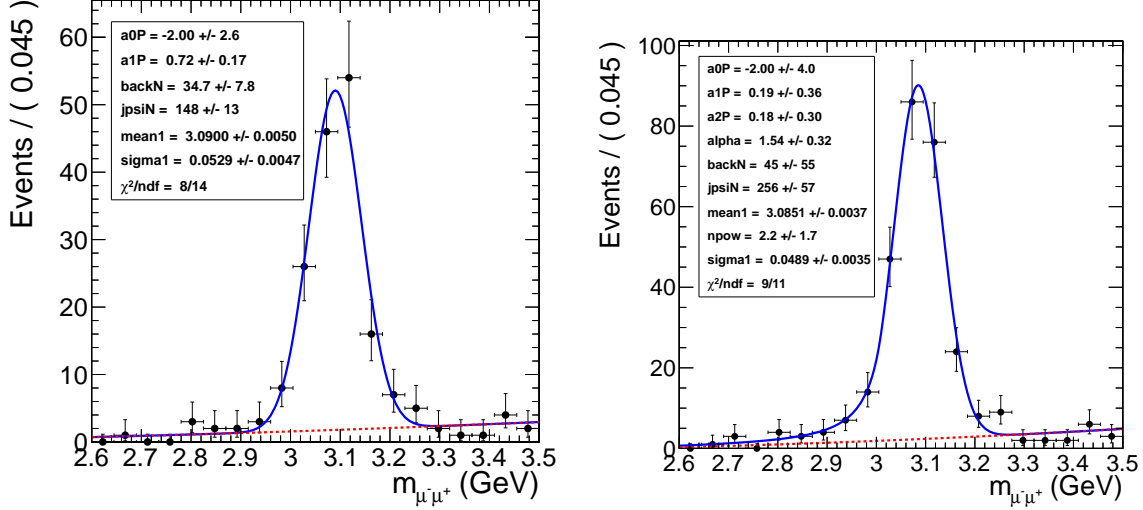


Figure 7.3: Mass fit to  $J/\psi$  using Gaussian (Left) and Crystal Ball (Right) for the signal and a polynomial for the background

Fig. 7.3 demonstrates the small dependence the raw  $J/\psi$  yield has on the fitting function. Both fit functions agree well, with reduced  $\chi^2$  values below one. The Crystal ball fit gives an upper estimate for the  $J/\psi$  yield. The Gaussian fit gives a lower estimate. The main difference comes from the lower mass tails. In the Crystal ball fit the lower tail is considered to be signal due to shifting of the mass spectrum to lower mass due to radiation from the final state muons. In the Gaussian fit the lower mass tail is considered to be background and the signal is sharper.

As check on the simultaneous  $p_T$  and mass fit, the mass fit is done using mass templates from STARlight. The coherent fraction,  $f_{co}$ , using the mass template for the simultaneous fit gave  $0.60 \pm 0.09$ , which is consistent with the nominal method described in Section 6.3.

### 7.6.2 Tag and probe from counting compared to fitting

The main purpose for fitting the mass spectra to estimate the efficiency is to separate the background from true signal. The background may not have the same efficiency as the signal, so

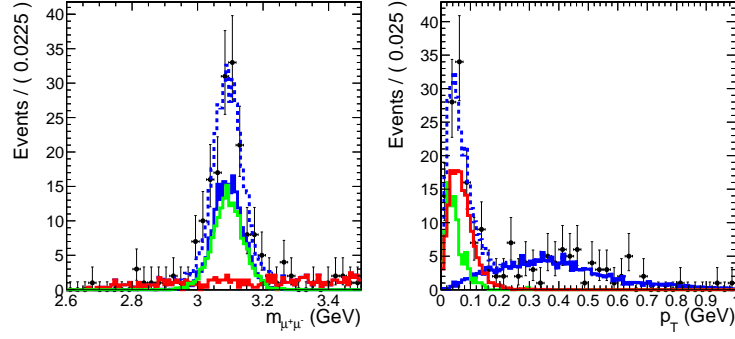


Figure 7.4: Simultaneous fit to the mass and  $p_T$  using mass templates for the mass fit.

separating the two is important if this is the case. In the tag and probe fit the signal peak from the  $J/\psi$  resonance is fit to the probes, passing probes, and failing probes alike (see Fig. 6.14). The signal shape, if from the same physical signal, will be identical in each of the three distributions. The background for the passing and failing probes is fit using different parameters for the background because the background may come from different physical processes than the signal, or from non-physical sources like combinatorial backgrounds or misidentified fake particles. When the background comes from sources other than the physical signal, the background may give an efficiency estimate that is lower than the signal.

The trigger efficiency measured by the tag and probe method depends on the fitting functions use to estimate the background and signal contributions. Depending on what functions is used to fit the spectra, the amount of background can be over or underestimated and effect the efficiency measurement. To estimate this effect, the tag and probe efficiencies were additionally measured by counting probes in the  $J/\psi$  mass window. The whole mass window is used to estimate the efficiency including all the events from the mass side bands. In this way, a worst case scenario estimate is given where all background events are included as signal.

From Fig. 7.5 it is apparent that the choice of fit function, and, therefore, the amount of background from the mass side bands is included in the signal measurement has very little effect on the tag and probe efficiency measurement. The small effect of including the side bands are due to the side bands being comprised mostly of photon-photon events. Because this background is neither decays from other particles like pions, nor is it from non-physical background like combinatorics,

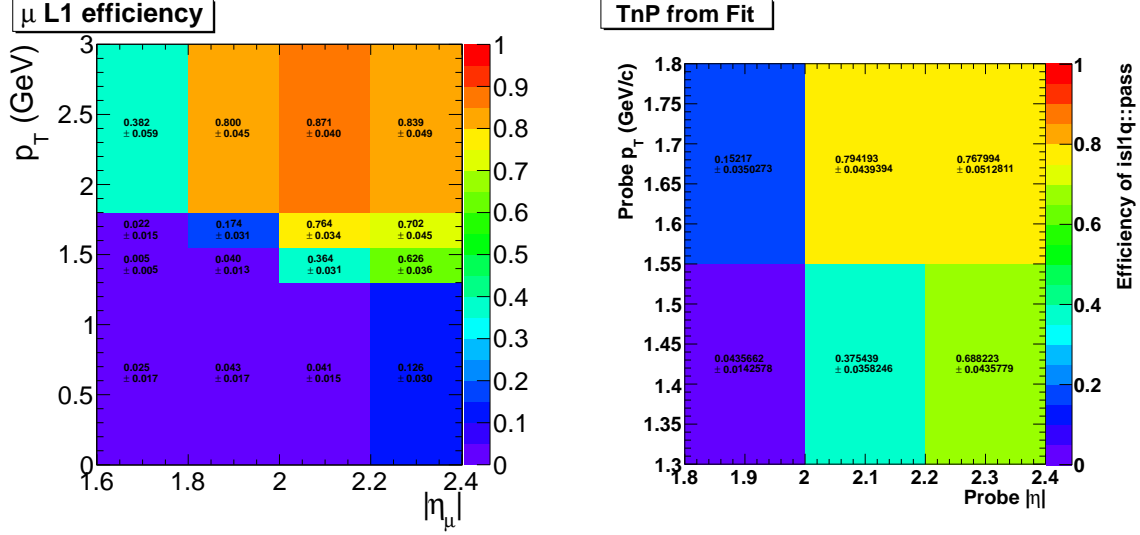


Figure 7.5: Tag and probe trigger efficiencies from counting (left) compared to fitting (right).

the efficiency for muons from the side bands are nearly identical to  $J/\psi$  signal. The photon-photon process directly produces two muons just like the  $J/\psi$ , therefore efficiency estimated from the side bands has little effect on the measurement because of this similarity. The counting and fitting trigger efficiency measurements agree within statistical uncertainties, so this uncertainty was taken to be negligibly.

### 7.6.3 The effect of noise on ZDC trigger efficiency estimates

The amount of electronic noise in the sample effects the ZDC energy distribution and, therefore, the trigger efficiency measurement. The more noise that sits below the one neutron peak, the lower the efficiency estimate will be. In Table 7.6, the zero bias sample with the timing cuts described in Section 4.1.3 gives a significantly higher estimated efficiency compared the zero bias sample with out timing cuts in Table 7.6. The same increase is seen when comparing the ZDC triggered sample with the ZDC triggered sample that also requires a pixel track shown in Table 7.2. The effect of the electronic noise is also present in the difference seen in using the two methods. As seen in Fig. 4.6, the new reconstruction method shows better separation of the one neutron peak from the electronic noise, in particular in  $ZDC^+$  where the signal gain is lower. For this reason, the zero

ZDC Side	Reco Method	$N_{events}$	$N_{trig}$	$\epsilon_{ZDC}$
Zero bias with ZDC timing cuts				
$ZDC^-$	comparison	88676	84429	$0.9521 \pm 0.0046$
$ZDC^-$	nominal	88480	84202	$0.9517 \pm 0.0046$
$ZDC^+$	comparison	59878	54728	$0.9140 \pm 0.0054$
$ZDC^+$	nominal	60467	54733	$0.9052 \pm 0.0053$
(ZDC <sup>-</sup> or ZDC <sup>+</sup> )				
$ZDC^-$	comparison	30986	30333	$0.9789 \pm 0.0079$
$ZDC^-$	nominal	31029	30339	$0.9778 \pm 0.0079$
$ZDC^+$	comparison	39178	30164	$0.7699 \pm 0.0059$
$ZDC^+$	nominal	35703	30443	$0.8527 \pm 0.0067$
Zero bias				
$ZDC^-$	comparison	109967	101598	$0.9239 \pm 0.0040$
$ZDC^-$	nominal	110230	101561	$0.9214 \pm 0.0040$
$ZDC^+$	comparison	253241	86660	$0.3422 \pm 0.0013$
$ZDC^+$	nominal	156336	87401	$0.5591 \pm 0.0024$

Table 7.6: ZDC trigger efficiencies using the nominal and comparison ZDC reconstructions for trigger sample that do not require a pixel track.

bias data, which contains the largest contribution from electronic noise, shows the most separation between the two methods and gives the lowest estimate for the ZDC trigger efficiency.

# Chapter 8

## Results and summary

In the previous two chapters the analysis steps to measure the coherent  $J/\psi$  photoproduction were given. In this chapter, the measured cross section for this process is given in Section ?? . Comparisons to the theoretical models are discussed. In addition, the rapidity corrections between UPC  $J/\psi$  and forward neutrons are presented and compared to model calculations in Section ?? . Finally, a summary of the complete thesis is given.

### 8.1 Coherent $J/\psi$ cross section

The coherent  $J/\psi$  cross section is calculated using the following formula:

$$\frac{d\sigma_{co}^{J/\psi}}{dy} = \frac{N_{cor} f_{co}}{\Delta y \mathcal{L}_{int} \epsilon_{ZDC} \epsilon_{pT} BR_{\mu^+\mu^-}}, \quad (8.1)$$

where  $N_{cor}$  is the corrected dimuon yield,  $f_{co}$  is the fraction of events that come from the coherent process,  $BR_{\mu^+\mu^-}$  is the branching ratio for  $J/\psi$  to  $\mu^+\mu^-$ ,  $\epsilon_{ZDC}$  is the efficiency for triggering the ZDC,  $\epsilon_{pT}$  is the efficiency for the 0.15 GeV cut in  $p_T$ ,  $\mathcal{L}_{int}$  is the integrated luminosity, and  $\Delta y$  is the width of the rapidity interval.

The raw yield of dimuon candidates was measured after applying the cuts described in Section 6.2.  $N_{cor}$  was calculated by dividing the raw yields by acceptance and efficiency factor from

which combines the acceptance from MC,  $A$ , and  $\epsilon_{trigger}^{dimuon}$  as described in Section. 6.4. The corrected yields,  $N_{cor}$ , are shown in Fig. ?? . For the coherent cross section measurement,  $N_{cor}$  is taken from the region  $2.0 < |y| < 2.2$  and  $p_T < 0.15$  GeV to avoid the edges of the detectors acceptance, bin migration in the calculation of  $A$ , and overlap between the coherent and incoherent process. From this procedure, the  $N_{cor}$  was measured to be 1903.

To measure  $f_{co}$ , the simultaneous fit shown in Fig. 6.10 was used. The normalizations for each of the three components to the signal are fixed by the fit as described in Section 6.3. The normalized coherent template is integrated up to 0.15 GeV in  $p_T$  and divided by the integral of the data  $p_T$  spectrum up to 0.15 GeV. The statistical error was taken from the template fit and is included in the coherent fraction,  $f_{co} = 0.60 \pm 0.11$ .

The two efficiency terms,  $\epsilon_{ZDC}$  and  $\epsilon_{p_T}$ , were measured from data and MC respectively. As described in Section 4.1,  $\epsilon_{ZDC}$  was measured in the from the ZDC triggered data set by dividing the number of events both fire the ZDC trigger and pass the one neutron threshold.  $\epsilon_{ZDC}$  was measured to be 0.96 with a negligible statistical error. The efficiency of the 0.15 GeV  $p_T$  cut was estimated from MC by dividing the number of events that are lost by applying the  $p_T$  cut after all other cuts are applied. From this method  $\epsilon_{p_T} = 0.95$ .

The remaining two terms,  $\mathcal{L}_{int}$  and  $BR_{\mu^+\mu^-}$ , depend on [34] and [37]. [34] describes the method of using activity in HF to measure the luminosity. From this method,  $\mathcal{L}_{int}$  was measured to be  $143.3 \mu b^{-1} \pm 7.2$ .  $BR_{\mu^+\mu^-}$  from [37] is  $0.0593 \pm 0.0006$ . From Equation 8.1,  $\frac{d\sigma_{co}^{J/\psi}}{dy} = 368 \mu b$ .

## 8.2 diMuon-neutron correlations

In this section the correlation between the rapidity of the  $\mu^+\mu^-$  and of the neutron is studied. The following samples are studied:

- $\gamma + A$  collisions in which two cases are considered
  - elastic coherent interaction: here photon interacts with entier nucleus coherently and



produce  $J/\psi$ . Another photon is needed to cause the breakup and neutron emission. Those two photons are uncorrelated and thus we don't expect to observe the correlation between the rapidity of the neutron and the rapidity of the  $J/\psi$ . In the data sample this corresponds to the low- $p_T J/\psi$  ( $p_T < 0.15$  GeV).

- inelastic incoherent interaction: here a single high  $p_T$  photon interacting with nucleus produce the  $J/\psi$  and neutron. The correlation between the rapidity of the neutron and the rapidity of the  $J/\psi$  is expected. In the data sample this corresponds to the high- $p_T J/\psi$  ( $0.15 < p_T < 1.05$ ).
- $\gamma\gamma$  collisions: two photons collide and produce the  $\mu^+\mu^-$  and the third photon is needed to excite one of the nucleons and produce neutron. Thus we don't expect to see the correlation between the rapidity of the neutron and the rapidity of the  $\mu^+\mu^-$ . In the data sample this corresponds to the  $\mu^+\mu^-$  with the invariant mass between 4 and 8 GeV.

In order to study the correlation in rapidity between the neutron and dimuon direction we below four quantities and give they values in Table 8.1.

- $y_{\mu\mu}^- \wedge y_n^-$ : number of  $\mu^+\mu^-$  having  $y < 0$  and the neutron in  $ZDC^-$  ( $y < 0$ )
- $y_{\mu\mu}^- \wedge y_n^+$ : number of  $\mu^+\mu^-$  having  $y < 0$  and the neutron in  $ZDC^+$  ( $y > 0$ )
- $y_{\mu\mu}^+ \wedge y_n^+$ : number of  $\mu^+\mu^-$  having  $y > 0$  and the neutron in  $ZDC^+$  ( $y > 0$ )
- $y_{\mu\mu}^+ \wedge y_n^-$ : number of  $\mu^+\mu^-$  having  $y > 0$  and the neutron in  $ZDC^-$  ( $y < 0$ )

The ratio  $R_{opp/same}$  is defined as:

$$R_{opp/same} = \frac{y_{\mu\mu}^- \wedge y_n^+ + y_{\mu\mu}^+ \wedge y_n^-}{y_{\mu\mu}^- \wedge y_n^- + y_{\mu\mu}^+ \wedge y_n^+} \quad (8.2)$$

Ratios studied in this section are only sensitive to the difference between the  $ZDC^-$  and  $ZDC^+$ . It is seen that the efficiency of both ZDCs is not exactly the same i.e. the efficiencies of  $ZDC^-$  and  $ZDC^+$  are respectively  $\epsilon_{ZDC^-}=0.98$  and  $\epsilon_{ZDC^+}=0.94$  and this is taken in the account in the

estimations. The  $R_{opp/same}$  ratio corrected by the ZDCs efficiencies is also included in Table 8.1 and called  $R_{opp/same}^{ZDC}$ . It is seen that the difference between corrected and uncorrected results is very small. Other uncertainties cancel. In this case cuts related to the acceptance and efficiencies corrections are not necessary and thus they are released.

Figure 8.1 gives  $p_T$  distributions of the  $J/\psi$  when  $J/\psi$  and neutron have the opposite rapidity direction or when they have the same rapidity direction for low- $p_T$  and high- $p_T$   $J/\psi$ . Also the Fig 8.1 gives the  $R_{opp/same}$  for low- $p_T$  and high- $p_T$   $J/\psi$ . It is seen from this plot that in the case of the low- $p_T$   $J/\psi$  this  $R_{opp/same}$  ratio is close to 1 and is decreasing when the  $p_T$  of  $J/\psi$  increases.

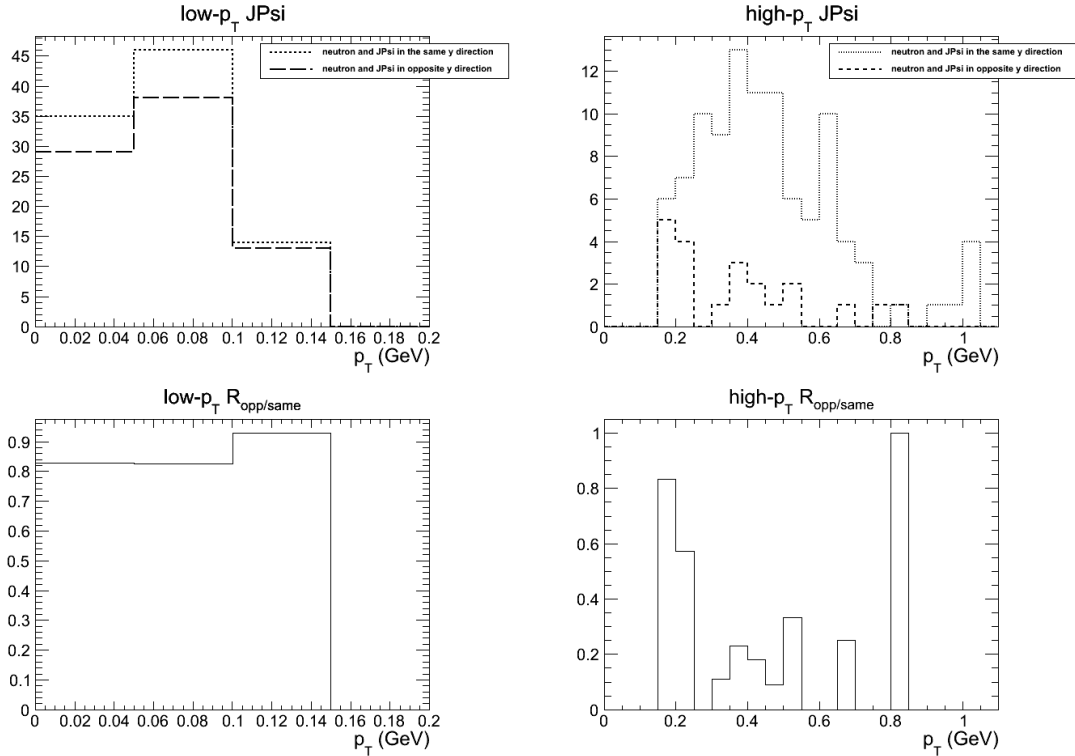


Figure 8.1: Transverse momentum distribution of the  $J/\psi$  when  $J/\psi$  and neutron have the opposite rapidity direction and the transverse momentum distribution of the  $J/\psi$  when  $J/\psi$  and neutron have the same rapidity direction for low- $p_T$  (top left) and high- $p_T$  (top right)  $J/\psi$ . Bottom: Ratios  $R_{opp/same}$  for low- $p_T$  (left) and high- $p_T$  (right)  $J/\psi$ .

Compiled for  $p_T < 1.05$  GeV  $R_{opp/same}$  ratio between the  $p_T$  distribution of the  $J/\psi$  having neutron emitted in the opposite direction and the  $J/\psi$  having the neutron emitted in the same direction is shown on Fig. 8.2. The same distributions as 8.1 but now as a function of rapidity of the  $J/\psi$  are

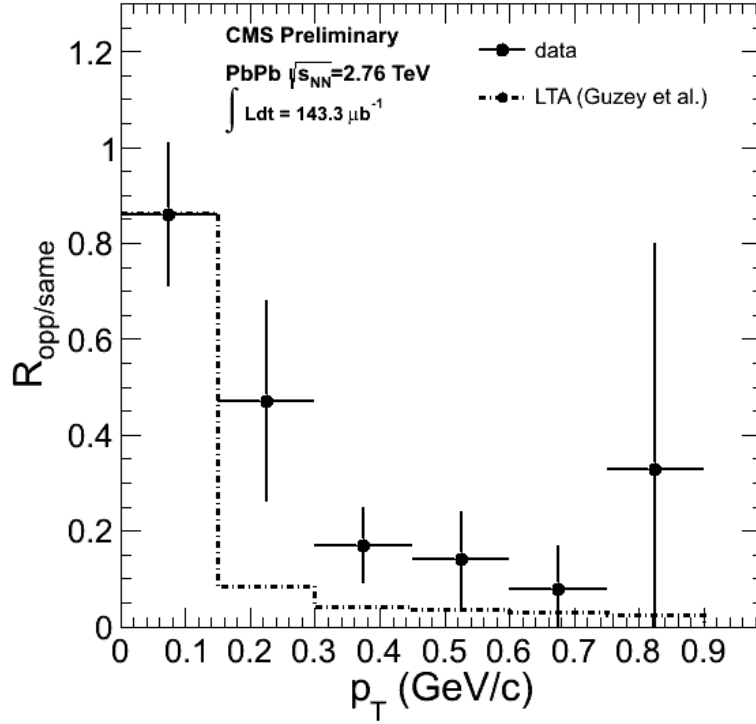


Figure 8.2: Ratio between the transverse momentum distribution of the  $J/\psi$  when  $J/\psi$  and neutron have the opposite direction and the transverse momentum distribution of the  $J/\psi$  when  $J/\psi$  and neutron have the same direction.

presented in the Fig 8.3 and compiled in Fig. 8.4.

Figure 8.5 shows the rapidity of the dimuon for the events that are tagged by the  $ZDC^+$  and  $ZDC^-$  means having the neutron emitted in the  $y > 0$  and  $y < 0$ .

Another, interesting correlation between the  $J/\psi$  rapidity direction and the neutron rapidity can be also studied with quantities defined in Eq. 8.3 that are calculated in the Table 8.1. Table 8.2 gives the same quantities as Table. 8.1 but here it is corrected for the difference between the efficiency of the  $ZDC^+$  and  $ZDC^-$ .

$$R_{(\mu\mu)^-}^{n^-/n^+} = \frac{y_{\mu\mu}^- \wedge y_n^-}{y_{\mu\mu}^- \wedge y_n^+} \quad \text{and} \quad R_{(\mu\mu)^+}^{n^-/n^+} = \frac{y_{\mu\mu}^+ \wedge y_n^-}{y_{\mu\mu}^+ \wedge y_n^+} \quad (8.3)$$

Integrated over rapidity, separately for  $y < 0$  and  $y > 0$  ratios from Table 8.2 are shown in the Figure 8.6.

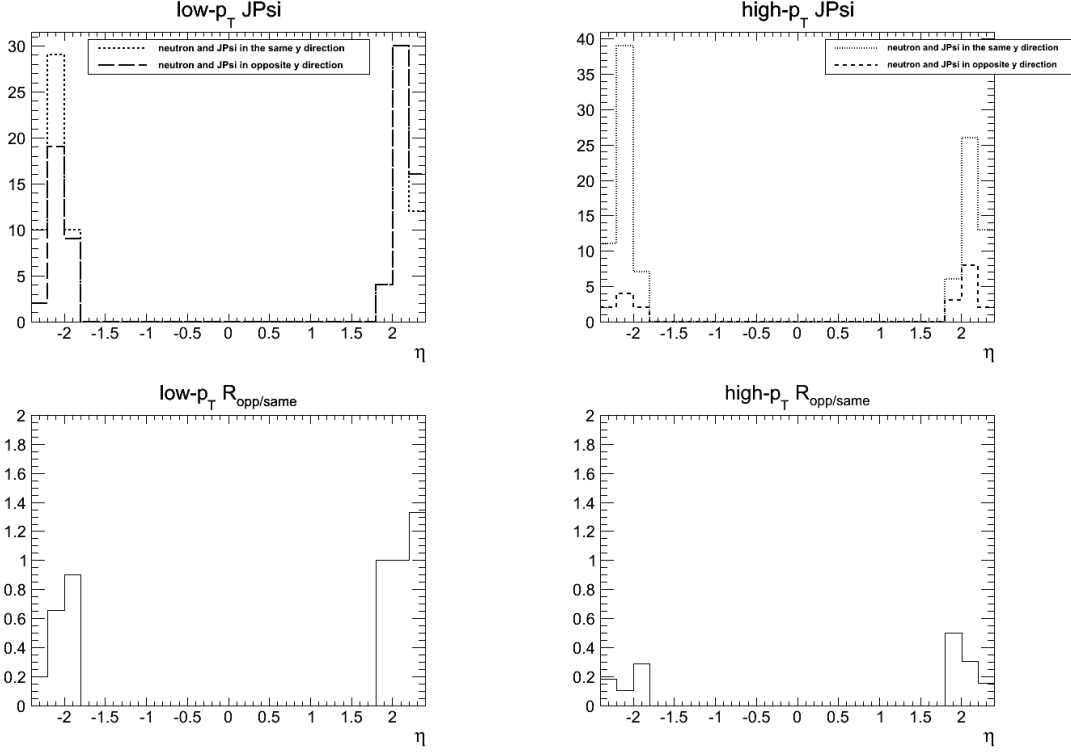


Figure 8.3: Rapidity distribution of the  $J/\psi$  when  $J/\psi$  and neutron have the opposite rapidity direction and the rapidity distribution of the  $J/\psi$  when  $J/\psi$  and neutron have the same rapidity direction for low- $p_T$ (top left) and high- $p_T$ (top right)  $J/\psi$ . Bottom: Ratios  $R_{opp/same}$  for low- $p_T$ ( left) and high- $p_T$ ( right)  $J/\psi$ .

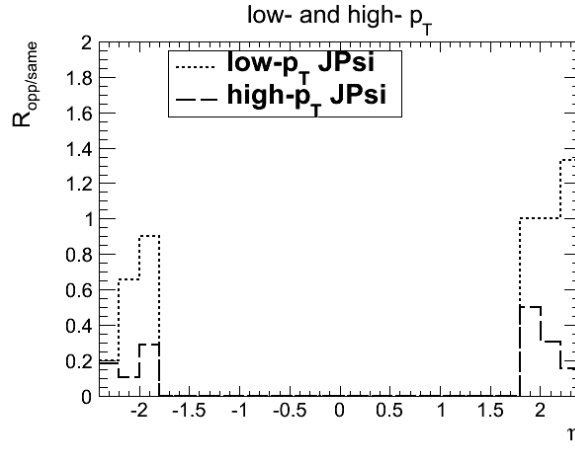


Figure 8.4: Rapidity ratios  $R_{opp/same}$  for low- $p_T$ ( left) and high- $p_T$ ( right)  $J/\psi$ .

From the Tab 8.1 and the Fig. 8.5 it is seen as expected that there is no correlation between the  $J/\psi$ rapidity and neutron rapidity in the case of the low- $p_T J/\psi$ and dimuons coming from  $\gamma\gamma$

	$y_{\mu\mu}^- \wedge y_n^-$	$y_{\mu\mu}^- \wedge y_n^+$	$y_{\mu\mu}^+ \wedge y_n^+$	$y_{\mu\mu}^+ \wedge y_n^-$	$R_{(\mu\mu)^-}^{n^-/n^+}$	$R_{(\mu\mu)^+}^{n^-/n^+}$
low- $p_T J/\psi$	$78 \pm 8.8$	$47 \pm 6.8$	$81 \pm 9$	$74 \pm 8.6$	$1.66 \pm 0.31$	$0.91 \pm 0.15$
high- $p_T J/\psi$	$132 \pm 11.5$	$17 \pm 4.1$	$117 \pm 10.8$	$29 \pm 5.4$	$7.76 \pm 2.0$	$0.25 \pm 0.05$
$\mu^+ \mu^-$ from $\gamma\gamma$	$80 \pm 8.9$	$81 \pm 9$	$75 \pm 8.7$	$83 \pm 9.1$	$0.99 \pm 0.16$	$1.11 \pm 0.18$

Table 8.1: Number of dimuon pairs for different directions of the neutron rapidity direction together with  $R_{(\mu\mu)^-}^{n^-/n^+}$  and  $R_{(\mu\mu)^+}^{n^-/n^+}$ .

	$R_{(\mu\mu)^-}^{\varepsilon_{ZDC}(n^-/n^+)}$	$R_{(\mu\mu)^+}^{\varepsilon_{ZDC}(n^-/n^+)}$
low- $p_T J/\psi$	$1.59 \pm 0.29$	$0.88 \pm 0.14$
high- $p_T J/\psi$	$7.45 \pm 1.87$	$0.24 \pm 0.05$
$\mu^+ \mu^-$ from $\gamma\gamma$	$0.95 \pm 0.15$	$1.06 \pm 0.17$

Table 8.2: Ratios  $R_{(\mu\mu)^-}^{\varepsilon_{ZDC}(n^-/n^+)}$  and  $R_{(\mu\mu)^+}^{\varepsilon_{ZDC}(n^-/n^+)}$  i.e.  $R_{(\mu\mu)^-}^{n^-/n^+}$  and  $R_{(\mu\mu)^+}^{n^-/n^+}$  corrected by the  $ZDC^+$  and  $ZDC^-$  efficiencies.

sample. In the case of the high- $p_T J/\psi$  the correlation is clearly visible.

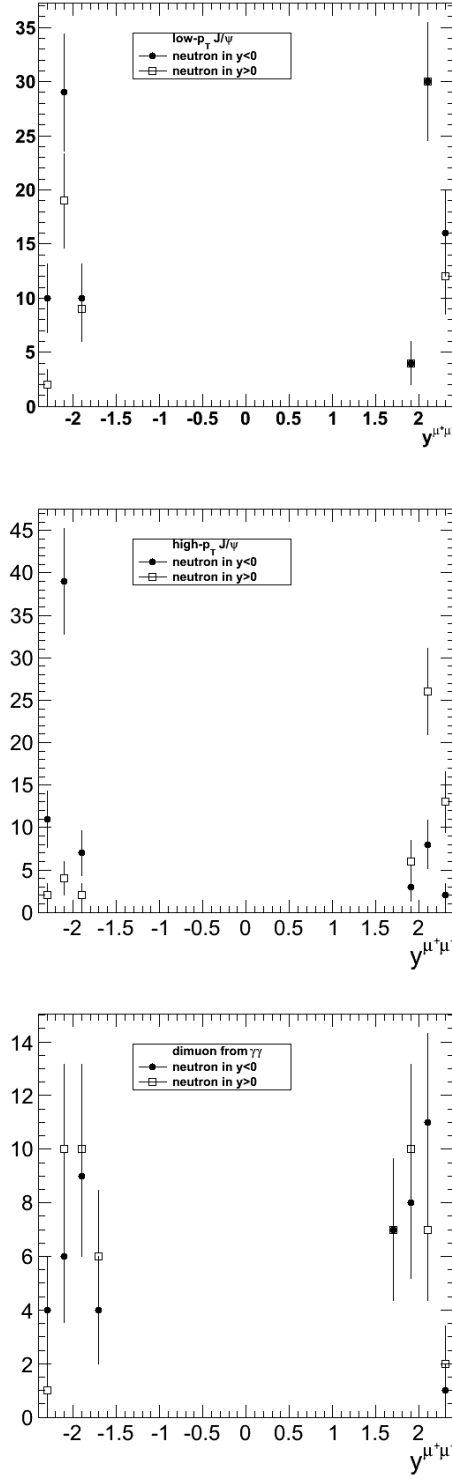


Figure 8.5: Rapidity distribution of  $J/\psi$  in the case of the events having the neutron in negative and positive rapidity for the low- $p_T$   $J/\psi$  (top), high- $p_T$   $J/\psi$  (middle) and dimuons from  $\gamma\gamma$  sample (bottom).

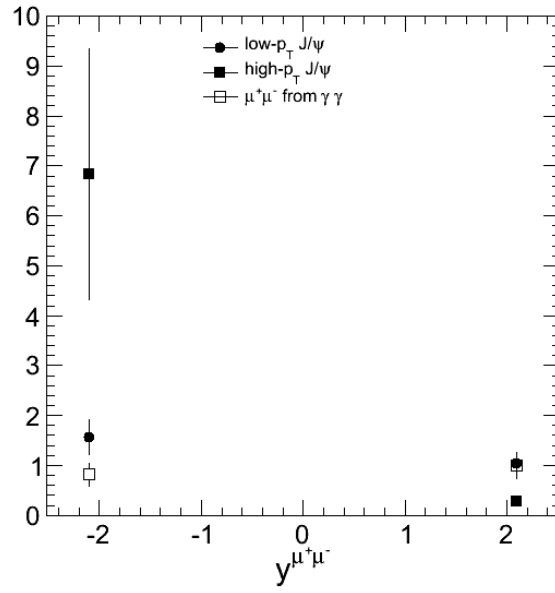


Figure 8.6:  $R^{\varepsilon_{ZDC}(n^-/n^+)}_{(\mu\mu)^-}$  and  $R^{\varepsilon_{ZDC}(n^-/n^+)}_{(\mu\mu)^+}$  integrated over one side in rapidity for low- and high- $p_T J/\psi$  and also for dimuons from  $\gamma\gamma$  sample.

# References

- [1] **PHENIX Collaboration** Collaboration, A. Adare *et al.*, “Enhanced production of direct photons in Au + Au collisions at  $\sqrt{s_{NN}} = 200\text{GeV}$  and implications for the initial temperature,” *Phys. Rev. Lett.* **104** (Mar, 2010) 132301.  
<http://link.aps.org/doi/10.1103/PhysRevLett.104.132301>.
- [2] M. Wilde, “Measurement of direct photons in pp and pb–pb collisions with {ALICE},” *Nuclear Physics A* **904–905** no. 0, (2013) 573c – 576c.  
<http://www.sciencedirect.com/science/article/pii/S0375947413001954>. The Quark Matter 2012 Proceedings of the {XXIII} International Conference on Ultrarelativistic Nucleus-Nucleus Collisions.
- [3] M. Chiu, A. Denisov, E. Garcia, J. Katzy, A. Makeev, M. Murray, and S. White, “Measurement of mutual coulomb dissociation in  $\sqrt{s_{NN}} = 130\text{GeV}$  *au + au* collisions,” *Phys. Rev. Lett.* **89** (Jun, 2002) 012302.  
<http://link.aps.org/doi/10.1103/PhysRevLett.89.012302>.
- [4] S. Chatrchyan *et al.*, “The cms experiment at the cern lhc,” *Journal of Instrumentation* **3** no. 08, (2008) S08004. <http://stacks.iop.org/1748-0221/3/i=08/a=S08004>.
- [5] **PHENIX Collaboration** Collaboration, A. Adare *et al.*, “Cold Nuclear Matter Effects on  $J/\psi$  Yields as a Function of Rapidity and Nuclear Geometry in Deuteron-Gold Collisions at  $\sqrt{s_{NN}} = 200\text{ GeV}$ ,” *Phys.Rev.Lett.* **107** (2011) 142301, arXiv:1010.1246 [nucl-ex].



- [6] **CMS Collaboration** Collaboration, S. Chatrchyan *et al.*, “Measurement of the pseudorapidity and centrality dependence of the transverse energy density in pb-pb collisions at  $\sqrt{s_{NN}}=2.76$  tev,” *Phys. Rev. Lett.* **109** (Oct, 2012) 152303.  
<http://link.aps.org/doi/10.1103/PhysRevLett.109.152303>.
- [7] **PHENIX Collaboration** Collaboration, S. S. Adler *et al.*, “Systematic studies of the centrality and  $\sqrt{s_{NN}}$  dependence of the  $de_T/d\eta$  and  $dn_{ch}/d\eta$  in heavy ion collisions at midrapidity,” *Phys. Rev. C* **71** (Mar, 2005) 034908.  
<http://link.aps.org/doi/10.1103/PhysRevC.71.034908>.
- [8] J. D. Bjorken, “Highly relativistic nucleus-nucleus collisions: The central rapidity region,” *Phys. Rev. D* **27** (Jan, 1983) 140–151.  
<http://link.aps.org/doi/10.1103/PhysRevD.27.140>.
- [9] **CMS Collaboration** Collaboration, S. Chatrchyan *et al.*, “Measurement of the elliptic anisotropy of charged particles produced in pbpb collisions at  $\sqrt{s_{NN}} = 2.76$  tev,” *Phys. Rev. C* **87** (Jan, 2013) 014902. <http://link.aps.org/doi/10.1103/PhysRevC.87.014902>.
- [10] H. Song, S. A. Bass, U. Heinz, T. Hirano, and C. Shen, “200 a gev Au + Au collisions serve a nearly perfect quark-gluon liquid,” *Phys. Rev. Lett.* **106** (May, 2011) 192301.  
<http://link.aps.org/doi/10.1103/PhysRevLett.106.192301>.
- [11] M. Klasen, “Hard photoproduction at hera,” hep-ph/0702052.
- [12] J. D. Jackson, *Classical electrodynamics*. Wiley, New York, NY, 3rd ed. ed., 1999.  
<http://cdsweb.cern.ch/record/490457>.
- [13] E. Fermi, “On the Theory of Collisions between Atoms and Electrically Charged Particles,” in *Electromagnetic Probes of Fundamental Physics*, W. Marciano and S. White, eds., pp. 243–252. Sept., 2003. hep-th/0205086.

- [14] C. A. Brau, *Modern Problems in Classical Electrodynamics*. Oxford, New York, NY, 1st ed. ed., 2004.
- [15] S. R. Klein and J. Nystrand, “Exclusive vector meson production in relativistic heavy ion collisions,” *Phys. Rev. C* **60** (Jun, 1999) 014903.  
<http://link.aps.org/doi/10.1103/PhysRevC.60.014903>.
- [16] A. Adeluyi and C. A. Bertulani, “Gluon distributions in nuclei probed at energies available at the CERN large hadron collider,” *Phys. Rev. C* **84** (Aug, 2011) 024916.  
<http://link.aps.org/doi/10.1103/PhysRevC.84.024916>.
- [17] V. Rebyakova, M. Strikman, and M. Zhalov, “Coherent rho and J/psi photoproduction in ultraperipheral processes with electromagnetic dissociation of heavy ions at RHIC and LHC,” *Phys.Lett.* **B710** (2012) 647–653, arXiv:1109.0737 [hep-ph].
- [18] I. A. Pshenichnov, J. P. Bondorf, I. N. Mishustin, A. Ventura, and S. Masetti, “Mutual heavy ion dissociation in peripheral collisions at ultrarelativistic energies,” *Phys. Rev. C* **64** (Jul, 2001) 024903. <http://link.aps.org/doi/10.1103/PhysRevC.64.024903>.
- [19] P. Chomaz, “Collective excitations in nuclei,”.
- [20] A. J. Baltz, C. Chasman, and S. N. White, “Correlated forward–backward dissociation and neutron spectra as a luminosity monitor in heavy-ion colliders,” *Nuclear Instruments and Methods in Physics Research Section A: Accelerators, Spectrometers, Detectors and Associated Equipment* **417** no. 1, (1998) 1 – 8.  
<http://www.sciencedirect.com/science/article/pii/S0168900298005750>.
- [21] I. A. Pshenichnov, I. N. Mishustin, J. P. Bondorf, A. S. Botvina, and A. S. Iljinov, “Particle emission following coulomb excitation in ultrarelativistic heavy-ion collisions,” *Phys. Rev. C* **60** (Sep, 1999) 044901. <http://link.aps.org/doi/10.1103/PhysRevC.60.044901>.

- [22] **STAR Collaboration** Collaboration, G. Agakishiev and others, “ $\rho^0$  photoproduction in auau collisions at  $\sqrt{s_{NN}} = 62.4$  gev measured with the star detector,” *Phys. Rev. C* **85** (Jan, 2012) 014910. <http://link.aps.org/doi/10.1103/PhysRevC.85.014910>.
- [23] **STAR Collaboration** Collaboration, C. Adler and others, “Coherent  $\rho^0$  production in ultraperipheral heavy-ion collisions,” *Phys. Rev. Lett.* **89** (Dec, 2002) 272302. <http://link.aps.org/doi/10.1103/PhysRevLett.89.272302>.
- [24] **STAR Collaboration** Collaboration, B. I. Abelev *et al.*, “ $\rho^0$  photoproduction in ultraperipheral relativistic heavy ion collisions at  $\sqrt{s_{NN}} = 200$  gev,” *Phys. Rev. C* **77** (Mar, 2008) 034910. <http://link.aps.org/doi/10.1103/PhysRevC.77.034910>.
- [25] S. Afanasiev *et al.*, “Photoproduction of and of high mass in ultra-peripheral au-au collisions at  $\sqrt{s_{NN}}$ ,” *Physics Letters B* **679** no. 4, (2009) 321 – 329. <http://www.sciencedirect.com/science/article/pii/S0370269309008983>.
- [26] A. Adeluyi and T. Nguyen, “Coherent photoproduction of  $\psi$  and  $\Upsilon$  mesons in ultraperipheral pPb and PbPb collisions at the CERN Large Hadron Collider at  $\sqrt{s_{NN}} = 5$  TeV and  $\sqrt{s_{NN}} = 2.76$  TeV,” *Phys. Rev. C* **87** (Feb, 2013) 027901, arXiv:1302.4288 [nucl-th]. <http://link.aps.org/doi/10.1103/PhysRevC.87.027901>.
- [27] V. Guzey, E. Kryshen, M. Strikman, and M. Zhalov, “Evidence for nuclear gluon shadowing from the ALICE measurements of pppb ultraperipheral exclusive production,” *Physics Letters B* **726** no. 1–3, (2013) 290 – 295. <http://www.sciencedirect.com/science/article/pii/S0370269313006825>.
- [28] **CMS Collaboration** Collaboration, G. Bayatian *et al.*, “CMS technical design report, volume II: Physics performance,” *J.Phys.* **G34** (2007) 995–1579.
- [29] A. Lardeux, “ $J/\psi$  production in Pb-Pb collisions at  $\sqrt{s_{NN}} = 2.76$  TeV in the ALICE experiment,” *J.Phys.Conf.Ser.* **446** (2013) 012042.

- [30] <http://starlight.hepforge.org>.
- [31] J. Alwall, A. Ballestrero, P. Bartalini, S. Belov, E. Boos, *et al.*, “A Standard format for Les Houches event files,” *Comput.Phys.Commun.* **176** (2007) 300–304, [arXiv:hep-ph/0609017](https://arxiv.org/abs/hep-ph/0609017) [hep-ph].
- [32] J. Allison *et al.*, “Geant4 developments and applications,” *Nuclear Science, IEEE Transactions on* **53** no. 1, (Feb, 2006) 270–278.
- [33] P. Faccioli, C. Lourenco, J. Seixas, and H. K. Wohri, “Towards the experimental clarification of quarkonium polarization,” *Eur.Phys.J.* **C69** (2010) 657–673, [arXiv:1006.2738](https://arxiv.org/abs/1006.2738) [hep-ph].
- [34] **CMS Collaboration** Collaboration, S. Chatrchyan *et al.*, “Measurement of CMS Luminosity,”.
- [35] S. Chatrchyan *et al.*, “ $J/\psi$  and  $\psi(2s)$  production in pp collisions at  $\sqrt{s} = 7$  tev,” *Journal of High Energy Physics* **2012** no. 2, (2012) .  
<http://dx.doi.org/10.1007/JHEP02%282012%29011>.
- [36] T. C. collaboration, “Performance of cms muon reconstruction in pp collision events at  $\sqrt{s} = 7$  tev,” *Journal of Instrumentation* **7** no. 10, (2012) P10002.  
<http://stacks.iop.org/1748-0221/7/i=10/a=P10002>.
- [37] **Particle Data Group** Collaboration, J. Beringer *et al.*, “Review of particle physics,” *Phys. Rev. D* **86** (Jul, 2012) 010001.  
<http://link.aps.org/doi/10.1103/PhysRevD.86.010001>.

# **Appendix A**

## **My Appendix, Next to my Spleen**

There could be lots of stuff here